

# Electrical and mechanical characterization of silicon and zinc oxide nanowires

A dissertation submitted to the  
Faculty of Sciences, Institute of Microtechnology  
Université de Neuchâtel  
Switzerland

for the degree of  
*Doctor of sciences*

presented by

Samuel Hoffmann

Laboratory for Mechanics of Materials and Nanostructures  
Empa, Swiss Federal Laboratories for Materials Testing and Research

accepted on the recommendation of  
Prof. Christophe Ballif, Doctoral advisor  
Dr. Johann Michler, co-examiner  
Prof. Michel Troyon, co-examiner  
Prof. Nico de Rooij, co-examiner

November 13, 2008

## IMPRIMATUR POUR LA THESE

Electrical and mechanical characterization  
of silicon and zinc oxide nanowires

**Samuel HOFFMANN**

---

UNIVERSITE DE NEUCHATEL

FACULTE DES SCIENCES

La Faculté des sciences de l'Université de Neuchâtel,  
sur le rapport des membres du jury

MM. C. Ballif (directeur de thèse),  
N. de Rooij, M. Troyon (Université de Reims, F)  
Et J. Michler (Thoune)

autorise l'impression de la présente thèse.

Neuchâtel, le 9 février 2009

Le doyen :  
F. Kessler

UNIVERSITE DE NEUCHATEL  
FACULTE DES SCIENCES  
Secrétariat - décanat de la faculté  
Rue Emile-Argand 11 - CP 158  
CH-2009 Neuchâtel  
*Felix Kessler*

# Abstract

## Keywords

silicon nanowires, zinc oxide nanowires, electrical properties, mechanical properties

## Mots clés

nanofils silicium, nanofils oxyde de zinc, propriétés électriques, propriétés mécaniques

Semiconducting nanowires can be grown epitaxially on crystalline substrates in predefined directions. This *bottom up* approach stands in contrast to the common *top down* technology in semiconductor industry. With diameters down to a few nanometers, the nanowires' small dimensions open up new possibilities for sensors and electronic devices. In order to be able to incorporate them in a new design, their physical properties have to be known.

This thesis deals with the electrical, mechanical, and electromechanical characterization of silicon and zinc oxide nanowires. Their small dimensions not only give them a high potential for new applications, but also reveal difficulties for the investigation of their properties. Common methods are used when possible, and new techniques are developed where standard methods reach their limits.

The doping concentration of nanowires doped during growth is measured by contacting them using electron beam lithography. It is shown that by adding phosphine or diborane to the growth chamber,  $n$  and  $p$  doping concentrations in the order of  $10^{19} \text{ cm}^{-3}$  can be achieved. A careful analysis reveals that the doping concentration changes along the nanowire axis; the conductivity being about a factor of two higher near the nanowire root than at its top.

$p$ - $n$  junctions along the nanowire axis are achieved by ion implantation after the nanowire growth. Because of the limited penetration depth of the dopant ions, this new doping process applies to rather short nanowires ( $< 500 \text{ nm}$ ), only, so it is difficult to contact them by electron beam lithography. Alternatively, a novel method allowing the location of junctions at the nanometer scale is introduced. This method is based on a nanomanipulator built into a scanning electron microscope that is used to contact the nanowires, and the  $p$ - $n$  doping profile is revealed by electron beam induced current imaging. The presented technique is able to qualitatively demonstrate the effective doping of very short individual nanowires.

The nanomanipulator inside the scanning electron microscope used for the electrical investigations was originally developed to manipulate the nanowires for mechanical characteriza-

tion. In contrast to traditional characterization techniques based on atomic force microscopy, a versatile tool is introduced that allows for fast characterization of nanostructures with real time visual feedback from the scanning electron microscope. In particular, tensile experiments can be performed in which the specimen is strained uniformly. This is important to reduce the influence of surface effects, for example when measuring Young's modulus of a material.

In order to precisely and automatically extract data from the experiments, an image analysis tool is programmed that can track objects with subpixel resolution. Further, finite element calculations show within which limits the analytic elastic beam formula can be used to calculate the maximum strain at the nanowire footing, taking into account its particular shape and the nanowires low aspect ratio.

Mechanical investigations reveal that the fracture strength of both silicon and zinc oxide nanowires is close to the theoretical limit. Subjected to bending experiments, silicon and zinc oxide nanowires show a fracture strain of  $(6.3 \pm 1.8)\%$  and  $(7.7 \pm 0.8)\%$  (average  $\pm 1$  standard deviation), respectively. Because of the controversial values published on Young's modulus of zinc oxide nanowires, these are subjected to tensile load as well. The tensile strength is  $\approx 4$  GPa, and Young's modulus is measured to be  $\approx 100$  GPa, close to the bulk value of 144 GPa.

Finally, an experiment for the measurement of electromechanical properties of silicon nanowires is proposed. It shows that the nanowires can be strained close to their fracture limit while measuring the electrical properties.

We expect that the new measurement techniques developed in this work can be applied to a large number of different nanowires and microstructures, speeding up characterization and thus contributing to an efficient development of new materials and devices.



# Contents

<b>Abstract</b>	<b>iii</b>
<b>1 Introduction</b>	<b>1</b>
1.1 Scope of the work . . . . .	1
1.2 Main contributions and results . . . . .	2
1.3 Thesis outline . . . . .	3
<b>2 Nanowire growth</b>	<b>5</b>
2.1 Vapor–liquid–solid growth of silicon nanowires . . . . .	5
2.2 Other growth techniques for silicon nanowires . . . . .	6
2.3 Some notes on gold as a precursor . . . . .	7
2.4 Growth of Zinc Oxide nanowires . . . . .	7
2.5 Nanowires investigated in this thesis . . . . .	7
<b>3 Electrical characterization</b>	<b>9</b>
3.1 Status in research . . . . .	10
3.1.1 Use of nanowires in novel devices . . . . .	10
3.1.2 Doping of nanowires . . . . .	12
3.2 Considerations on the characterization of nanowires . . . . .	13
3.2.1 Nanowire resistance and number of charge carriers present . . . . .	13
3.2.2 Contact characteristics . . . . .	14
3.2.3 4 point resistance measurements . . . . .	18
3.2.4 Characteristics of the electrical measurement instrument . . . . .	19
3.2.5 Heating of the nanowire . . . . .	20
3.2.6 Influence of the nanowire surface . . . . .	21
3.2.7 High–field effects . . . . .	23
3.3 Measurement techniques and their difficulties . . . . .	24
3.4 Determination of the doping concentration . . . . .	26
3.4.1 Electron beam lithography process . . . . .	27
3.4.2 Investigated characteristics . . . . .	28
3.4.3 Undoped nanowires . . . . .	31
3.4.4 Boron doped nanowires . . . . .	32
3.4.5 Phosphorous doped nanowires . . . . .	34

3.4.6	Discussion . . . . .	37
3.5	Location of junctions by EBIC imaging . . . . .	39
3.5.1	Principle of electron beam induced current imaging . . . . .	40
3.5.2	Scanning photocurrent imaging . . . . .	40
3.5.3	Doping of nanowires by ion implantation . . . . .	41
3.5.4	Experimental . . . . .	42
3.5.5	Results . . . . .	44
3.5.6	Discussion . . . . .	46
<b>4</b>	<b>Mechanical characterization</b>	<b>49</b>
4.1	Motivation . . . . .	49
4.1.1	Fracture mechanics . . . . .	49
4.1.2	Young's modulus . . . . .	51
4.2	Linear beam theory . . . . .	53
4.2.1	Bending experiment . . . . .	53
4.2.2	Tensile experiment . . . . .	54
4.3	Experimental . . . . .	54
4.3.1	Manipulation setup . . . . .	54
4.3.2	Spotfinder . . . . .	56
4.4	Results . . . . .	59
4.4.1	FEM calculations on a bent nanowire . . . . .	59
4.4.2	Results on silicon nanowires . . . . .	61
4.4.3	Results on zinc oxide nanowires . . . . .	62
4.4.4	Error analysis . . . . .	62
4.5	Discussion . . . . .	65
4.5.1	Silicon nanowires . . . . .	65
4.5.2	Zinc Oxide nanowires . . . . .	69
<b>5</b>	<b>Electromechanical characterization</b>	<b>71</b>
5.1	Motivation . . . . .	71
5.2	Experiment . . . . .	72
5.3	Results . . . . .	73
5.4	Discussion . . . . .	78
<b>6</b>	<b>Conclusions and perspectives</b>	<b>79</b>
<b>A</b>	<b>Matlab script: Heating a nanowire</b>	<b>83</b>
<b>B</b>	<b>Details of the lithography process</b>	<b>85</b>
<b>Backmatter</b>		<b>87</b>
	List of Abbreviations, Figures and Tables, Bibliography, Acknowledgements . . . . .	87

# Chapter 1

## Introduction

The ongoing downscaling of devices in semiconductor industry far below the micrometer scale has pushed the development of a large variety of novel fabrication methods. One of these is the bottom up growth of single crystal nanowires by epitaxial deposition of material. These nanowires have diameters in the range of tens to some hundreds of nanometers and a length of several micrometers. Their use as sensors or light sources and as components in solar cells is extensively discussed in literature.

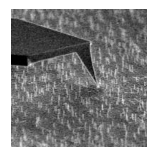
### 1.1 Scope of the work

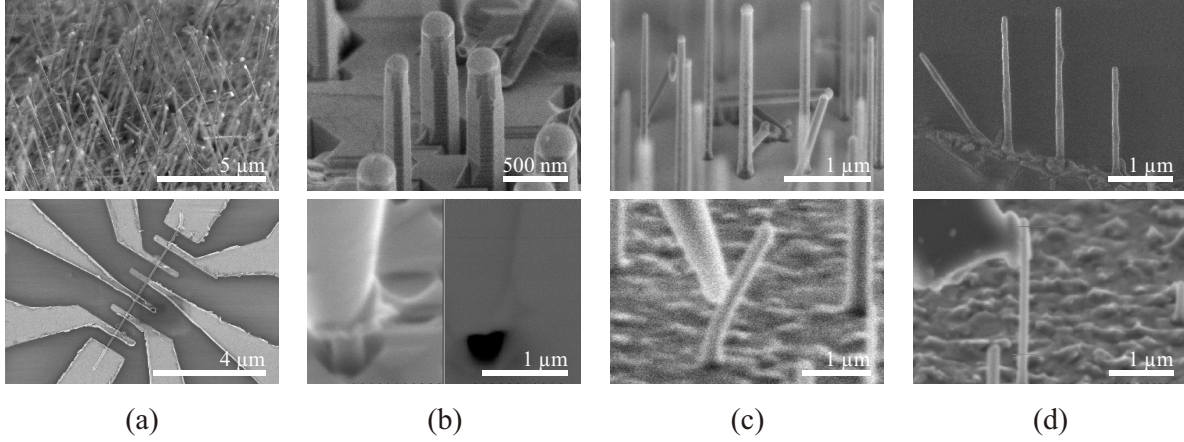
Before a new material can be used in a device, its properties must be determined. For electrical applications the doping concentration is a pivotal parameter, whereas for the use in electromechanical systems, Young's modulus and the mechanical strength are critical characteristics. But even if in a final device the nanowires are rigidly fixed, their mechanical properties may be important during processing steps because they are freestanding structures, unlike components in planar silicon technology. This thesis focuses on the electrical and mechanical characterization methods of semiconducting nanowires and presents results on silicon and zinc oxide nanowires thereof.

Figure 1.1 shows different nanowires and some experiments which they are involved in. Depending on the growth process, nanowires have diameters from 10–500 nm and lengths from 100 nm – 100  $\mu\text{m}$ . Their small size demands new characterization methods, because the specimens cannot be fixed to standard test equipment. The work thus does not only consist of the actual characterization, but a large part deals with the development of the tools for this purpose.

A versatile setup is to be developed that allows (i) the measurement of fracture strength and Young's modulus on individual nanowires; (ii) their manipulation for the fabrication of prototypes; (iii) the electrical contact of nanowires and (iv) the investigation of their electromechanical properties. The constraints of the setup are to be explored, and for the tasks that go beyond its limitations alternative techniques are to be found.

Mechanically nanowires differ from bulk material in the aspect that they can be subjected to very high strains. In present silicon technology, strained silicon is already used to enhance





**Figure 1.1:** *Different nanowires and experiments for their characterization. (a) Long and dense nanowires, grown with silane as precursor at  $\approx 1$  mbar. Electron beam lithography is used to contact and characterize them in four and eight point configurations. (b) Short and wide nanowires grown by electron beam evaporation of silicon. A nanomanipulator in a scanning electron microscope is used to contact them at the top and reveal junctions by electron beam induced current imaging. (c) Nanowires grown with silane in a ultra high vacuum environment. They are subjected to bending experiments to measure their strength. (d) Zinc oxide nanowires grown on sapphire. In tensile experiments, their strength as well as Young's modulus can be measured.*

the carrier mobility. A long term goal is thus to investigate the electrical properties of silicon at even higher strains. Also, when their diameter is reduced, quantum effects may arise that can be explored in conjunction with strain. The new methods developed should thus be flexible enough so that they can be applied to a variety of systems and materials.

## 1.2 Main contributions and results

A nanomanipulator is developed that allows individual nanowires to undergo bending and tensile experiments. The proposed methods for the mechanical characterization make use of the imaging capabilities of the scanning electron microscope (SEM), which gives visual feedback in real time. This immediate control facilitates the characterization in a way that the number of experiments can be increased substantially, compared to traditional techniques like atomic force microscopy. This in turn allows the verification of the reproducibility and reliability of the results. By *in situ* manipulating the nanowires until failure, their bending and tensile strength is measured (Fig. 1.1(c) and (d)). From the tensile experiment, Young's modulus can be estimated. To date, the measurement of Young's modulus on nanowires has been performed exclusively in bending or resonance experiments. In these flexural configurations, part of the surface is highly strained and thus influences and possibly falsifies results in small specimens. The setup introduced provides the new possibility of measuring Young's modulus in a tensile configuration, which is an important improvement in determining the stiffness of nanowires.

In particular, the bending strength of vapor-liquid-solid grown silicon nanowires is mea-

sured to be  $(6.3 \pm 1.8)\%$ . Zinc oxide nanowires are subjected to both bending and tensile experiments. The bending strength  $((7.7 \pm 0.8)\%)$  turns out to be roughly twice as high as the tensile strength ( $\approx 4$  GPa). From the tensile experiment, Young's modulus is found to be  $\approx 100$  GPa, close to the value of bulk ZnO.

Contacting perpendicular on the substrate standing nanowires, the setup is used to qualitatively characterize  $p$ - $n$  junctions in ion implanted nanowires that are too short to be contacted by electron beam lithography. Therefore, advantage of the SEM is taken by measuring the electron beam induced current induced in depleted regions (Fig. 1.1(b)).

The contact established between the manipulator tip and the nanowire is not stable enough for a reliable, quantitative extraction of the resistance of the nanowire. Four point measurements using electron beam lithography are thus carried out to investigate nanowires from different doping procedures (Fig. 1.1(a)). In this work, the measurements on successfully doped nanowires are presented and, for the first time, it is shown that the doping concentration varies along the growth axis. In particular, it is shown that nanowires can be doped up to concentrations of  $10^{19} \text{ cm}^{-3}$  by adding phosphine or diborane during growth.

The experiences acquired during mechanical and electrical characterization are combined in the development of a novel device that allows for the electromechanical characterization of silicon nanowires. The nanowires are grown in a silicon trench that can be stretched by the nanomanipulator while measuring the nanowires conductance. It is shown that the nanowires can be strained close to the theoretical limit. Because the nanowires reveal strengths far beyond the ones of millimeter sized samples, these preliminary investigations illustrate a promising way to measure the electrical properties of silicon at strains 100 times higher than what was measured up to now.

The methods developed throughout this work are not restricted to the electrical and mechanical investigation of silicon and zinc oxide nanowires, but open avenues for the characterization of other nanowires and microstructures. The nanomanipulation setup presented is also used to make prototypes for new devices. In particular, novel scanning probes for signal enhanced nanoscale Raman spectroscopy are fabricated. This, however, is not the subject of the present thesis, see the list of publications for literature thereon.<sup>5,6</sup>

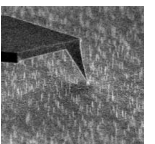
### 1.3 Thesis outline

The thesis is divided into three major chapters dealing with the electrical characterization, the mechanical characterization, and the presentation of a new approach for measuring electromechanical properties. The different topics are put into the context of the literature in the corresponding chapters.

Chapter 2 briefly presents different growth processes and the morphology of nanowires.

Chapter 3 introduces the electrical properties of silicon nanowires and some aspects that have to be considered when measuring them. The electron beam lithography process is described together with the presentation of the results that are achieved with it on nanowires doped during growth. The technique of electron beam induced current imaging is introduced to reveal  $p$ - $n$  junctions in very short nanowires.

Chapter 4 presents mechanical characterization methods for nanowires. The nanomanip-



ulation setup inside the SEM is described. An image analysis tool that tracks objects in an image sequence is presented and its limits are explored. Finite element calculations are performed and reveal within which limits the elastic beam formula for a bent beam can be used for the particular case of nanowires. Results on the silicon and zinc oxide nanowires are presented and discussed.

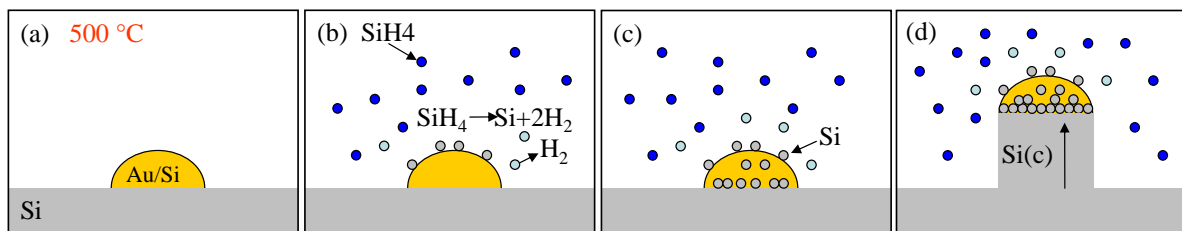
Chapter 5 presents a novel setup for measuring electrical properties of silicon nanowires in function of strain. The results of a initial experiment are presented and characterized mechanically. However, more work needs to be done. The problems encountered are discussed, and possible solutions to overcome them are proposed.

## Chapter 2

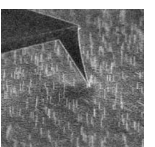
# Nanowire growth

### 2.1 Vapor–liquid–solid growth of silicon nanowires

Vertically aligned silicon nanowires are commonly grown by the vapor–liquid–solid (VLS) mechanism in which a metal catalyst forms eutectic droplets at the growing tips of the nanowires.<sup>29</sup> Figure 2.1 shows the growth diagram for the VLS process, in which a thin layer of Au is sputtered on a clean and flat silicon substrate. When heated up, the gold reacts with the silicon and at its eutectic temperature it starts to melt and forms small droplets. A supply of Si vapor supersaturates these droplets with Si and leads to its precipitation at the liquid–solid (droplet–silicon) interface. Under the gold droplet the nanowire grows as long as the Si vapor is present. SEM and transmission electron microscope (TEM) images of a nanowire are shown in Fig. 2.2.



**Figure 2.1:** Epitaxial VLS growth of nanowires: (a) A flat silicon wafer is cleaned and the oxide etched away by an HF dip. 0.5–2 nm of Au is sputtered and heated beyond the eutectic temperature such that small liquid droplets form. (b) While still heated, Si vapor such as silane ( $\text{SiH}_4$ ) is introduced. At the Au–Si eutecticum, the Si–H bonds are cracked and the hydrogen leaves the system. (c) The eutectic droplet supersaturates and silicon is precipitated at the droplet/crystal interface. (d) The nanowire grows as long as the silane is present and the temperature is high enough. From Steinmair<sup>92</sup>.



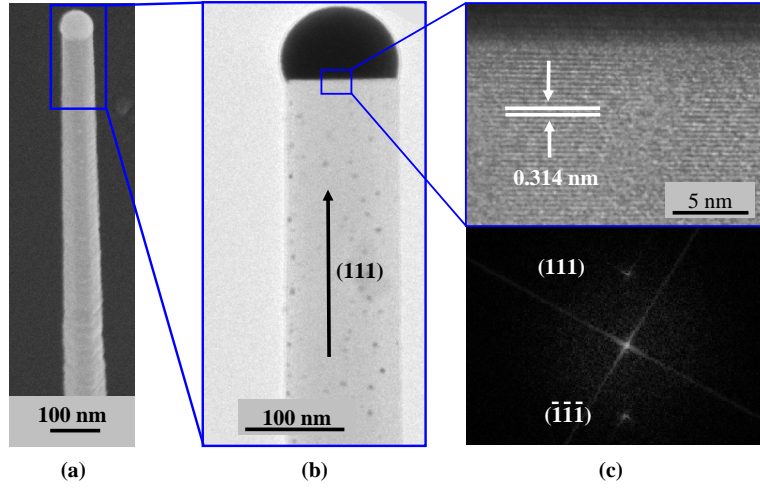


**Figure 2.2:** (a) SEM image showing a nanowire with the gold droplet on top of it. The nanowire becomes thinner towards the top because during growth the Au droplet becomes smaller (Ostwald ripening). (b) TEM image showing gold particles on the surface of the nanowire as dark spots. (c) From high resolution TEM images, the lattice constant can be measured from which the growth direction of the nanowire can be determined. The diffraction pattern demonstrates the crystallinity and also shows the growth direction. From Steinmair<sup>92</sup>.

## 2.2 Other growth techniques for silicon nanowires

By far, the most nanowires grown use gold as a catalyst, but some other metals are tested as well. For silicon nanowires, Lugstein *et al* use gallium/gold as a precursor metal.<sup>62</sup> Titanium is used as precursor as well, but hydrogen chloride (HCl) needs to be added during growth to prevent tapering.<sup>88</sup>

As an alternative to the chemical vapor deposition (CVD) with silane, Schubert *et al* investigate electron beam evaporation (EBE) VLS growth.<sup>86</sup> Silicon atoms are evaporated by an electron beam and directly offered to the gold-silicon droplet in the molecular beam. The disadvantage of this process is that silicon is deposited over all the sample surface and the ratio of the nanowire length to the thickness of the continuously deposited layer is only about 2:1.

Silicon nanowires can also be fabricated within the pores of anodic alumina templates via gold-catalysed VLS growth. The template serves as a support structure for nanowire growth and fabrication of electrical contacts to the nanowire arrays. Using silane as the source gas and trimethylboron ((CH<sub>3</sub>)<sub>3</sub>B) and phosphine (PH<sub>3</sub>) as dopants, both *p* and *n*-type doping can be achieved.<sup>23</sup>

A thermal evaporation method presented by Byon *et al* yields a dense mat of long and straight nanowires in absence of any catalyst.<sup>10</sup> The disadvantage of the process is the high temperatures necessary to evaporate silicon powder (1230 °C) and to provoke nanowire formation (substrate temperature 1000 °C).



## 2.3 Some notes on gold as a precursor

Au is favored as a catalytic material because of the low melting point at the eutectic composition ( $\text{Au}_{82}\text{Si}_{18}$  at 360 °C), which enables low temperature growth of Si nanowires (500–650 °C in most cases). In addition, the low equilibrium solubility (e.g.,  $2 \times 10^{15}$  Au atoms/cm<sup>3</sup> in Si at 650 °C)<sup>17</sup> and the absence of stable silicides in the Au–Si phase diagram suggests that growth of clean Si nanowires might be possible.

However, *in situ* TEM growth has directly shown that surface migration of Au atoms occurs from the smaller droplets to the larger ones (Ostwald ripening),<sup>35</sup> so that the sidewalls of Si nanowires are covered by a significant amount of Au (as shown in Fig. 2.2(b)). Furthermore, growth techniques such as CVD or EBE may extend the solubility limit of Au in Si nanowires or lead to high non equilibrium supersaturations.

As Au is known to adversely affect the carrier lifetime in Si,<sup>17</sup> Oh *et al.* investigate point defect configurations of supersaturated Au atoms inside Si nanowires.<sup>75</sup> They utilize the single-atom sensitivity of high-angle annular dark field scanning tunneling electron microscopy, also known as *Z*-contrast imaging. This imaging mode has a very small depth of focus, which makes it possible to localize individual Au atoms within a Si nanowire. Four different Au point defect configurations are distinguished in *Z*-contrast images, and the relative number of densities of the various configurations correspond to their calculated formation energies. A larger number of Au atoms is counted closer to the wire surface, in agreement with the typical diffusion profile that Au attains in Si, the so called "U-shape" profile.<sup>70</sup> The absolute density of Au atoms inside the nanowire was not specified.

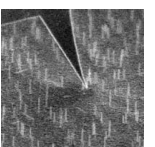
## 2.4 Growth of Zinc Oxide nanowires

The crystal structure of ZnO nanowires is of the hexagonal wurtzite type symmetry, so GaN, also of wurtzite type crystal symmetry, is a good candidate for epitaxial growth as the lattice mismatch between the two materials is only 1.9%. GaN(0001) can be grown epitaxially on Si(111) by a metal organic CVD process.<sup>50</sup>

Zn powder is heated in an Ar atmosphere for the nanowire growth. The necessary oxygen is either present from a leak in the chamber, or alternatively the Ar gas can be moisturized by flowing dry Ar over a distilled water surface. The growth of the nanowires can occur with or without a metal catalyst. When Au is used as a catalyst, the molten Au provides the necessary nucleation sites for Zn/ZnO vapors, leading to a VLS growth process.<sup>26</sup> Fan *et al.* observe a process without any metal precursor, where a rough wetting layer on a GaN/Si substrate provides the necessary nucleation sites for the nanowire growth.<sup>24</sup> *a*-plane oriented  $\alpha\text{-Al}_2\text{O}_3$  sapphire single crystal has a much higher lattice mismatch with ZnO (32%) than GaN, but can also be used as substrate for nanowire growth.<sup>27</sup>

## 2.5 Nanowires investigated in this thesis

Four different types of nanowires are investigated in this thesis. The detailed growth processes are given in the corresponding sections; here just an overview is given:



- Silicon VLS growth with silane and phosphine or diborane as dopant sources yields  $n$  and  $p$  doped nanowires. Their electrical investigation is presented in Sect. [3.4](#).
- Silicon EBE grown nanowires are chosen to be doped by ion implantation because they are relatively wide and have a low aspect ratio. These are investigated by electron beam induced current imaging in Sect. [3.5](#)
- Silicon VLS grown nanowires with silane in a ultra high vacuum (UHV) environment are chosen for the bending experiments, because they almost all stand perpendicular to the substrate and are uniform in diameter, as presented in Sect. [4.4.2](#).
- Zinc oxide nanowires grown from Zn powder are subjected to bending and tensile experiments, measuring fracture strength and Young's modulus. This is the subject of Sect. [4.4.3](#).

## Chapter 3

# Electrical characterization

### Abstract

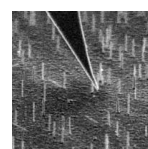
This chapter focuses on the electrical characterization of (i) nanowires doped during growth and (ii) post growth ion implanted nanowires.

The nanowires that are doped during growth are quite long (2–7  $\mu\text{m}$ ), so that they can be contacted by electron-beam lithography. Four point measurements are performed to measure their doping concentration, and, based on a new design with 8 electrodes on a same nanowire, the doping profile along the nanowire axis is investigated. Examination of the electrode-nanowire contacts reveals that the contact at the nanowire root is ohmic, whereas all other contacts are nonlinear and have a much higher contact resistance.

The post growth, ion implanted nanowires are shorter,  $\leq 500$  nm, making it difficult to contact them by lithography. The nanowires are thus contacted with a tip of a PtIr wire on a nanomanipulator in a SEM. Electron beam induced current imaging reveals the Schottky contact between the tip and a uniformly doped nanowire, and also shows that  $p$ - $n$  junctions can be implanted. These results are supported by current voltage sweeps between the PtIr tip and the substrate.

First, possible electronic applications of nanowires are presented, followed by a literature review on doping nanowires. Section 3.2 puts some theoretical aspects of semiconductor physics into the context of nanowires to give a feeling on what the work deals with in terms of resistivity and contact characteristics. The four point method is introduced and the requirements for the measurement instrument are discussed. Self-heating of the nanowire, the influence of the nanowire surface and high-field effects are theoretically investigated in order to check if these effects distort the measurement results. Section 3.3 points out the difficulties of electrical characterization.

Section 3.4 presents the electron beam lithography process and the results on the resistivities measured on nanowires doped during growth. The principle of electron beam induced current imaging together with the properties of the ion beam implanted nanowires are presented in Sec. 3.5.



## 3.1 Status in research

### 3.1.1 Use of nanowires in novel devices

Miniaturization of silicon electronics is being intensely pursued. When silicon nanowires first were grown, it was not sure how far fundamental limits of lithography may prevent current techniques from reaching the deep nanometer regime for highly integrated devices. The use of nanoscale structures as building blocks for self-assembled devices were considered to potentially eliminate conventional and costly fabrication lines, while still maintaining some concepts that have proven successful in microelectronics.

Cui *et al* have fabricated fundamental building blocks of electronic devices already in the early stage of silicon nanowire research in 2001.<sup>19</sup>  $p$ - $n$  junctions and bipolar transistors have been fabricated by laying  $p$ -doped nanowires over  $n$ -doped nanowires and contacting them by electron beam (EBeam) lithography. Surprisingly, the native oxide present on the nanowire surfaces did not disturb the junction properties at the nanowire–nanowire contact.

First field-effect transistors (FET) were fabricated by laying doped nanowires on an oxidized silicon wafer, making drain and source contacts by EBeam lithography and using the underlying silicon as a back gate.<sup>20,115</sup> This planar configuration, however, is not very space efficient, as the contacts are still fabricated by means of lithography. Therefore, efforts were undertaken to make vertical nanowire FETs with a surround gate geometry, see Fig. 3.1(a).<sup>8,73,84</sup>

In the meantime, however, Intel has demonstrated its 32 nm logic process, which should start production in 2009.<sup>i</sup> For purely electronic applications, the semiconducting industry has thus overtaken the nanowire state of the art in terms of minimal feature size.

Nevertheless, nanowires have proven potential use in other fields. Their sharp tip apex can be used as an electron source in field emitters<sup>43,105</sup>, or light sources can be built as light emitting diodes<sup>22</sup> or even lasers<sup>41,46</sup>.

A first application in the solar industry has been reported by Tian *et al*, who have fabricated a coaxial  $p$ - $i$ - $n$  nanowire structure and investigated its light to electricity conversion efficiency.<sup>101</sup> Under the illumination of one sun, a single nanowire yields a maximum power output of up to 200 pW. When incorporated into a solar cell, this can yield a conversion efficiency of 3.4 %, with stable and improved efficiencies achievable at high-flux illuminations. Electrical energy can also be gained out of mechanical movements. The group of Z.L. Wang has developed a direct current nanogenerator with ZnO nanowires, as shown in Fig. 3.1(b).<sup>106</sup>

Due to their large surface to volume ratio, silicon nanowires have also been used in the development of new sensors. For chemical sensors, the nanowire often forms the channel of a FET that is modulated by the surface potential, which in turn is influenced by the environment, as illustrated in Fig. 3.1(c). Prototypes of detectors have been built for cancer markers<sup>116</sup>, bacteria<sup>68</sup> and pH<sup>14</sup> levels, to cite just a few.

For very thin nanowires and at very low temperatures, quantum effects can be observed, because the nanowire becomes an electrically 1 dimensional system.<sup>82</sup> Such structures allow the building of single electron transistors<sup>95,99</sup>, resonant tunneling diodes<sup>9</sup> and quantum dots<sup>7</sup>.

Efforts have also been undertaken to explore the electrical properties of highly strained silicon by means of the high fracture strength of nanowires. However, He *et al* have up to date

---

<sup>i</sup>www.intel.com

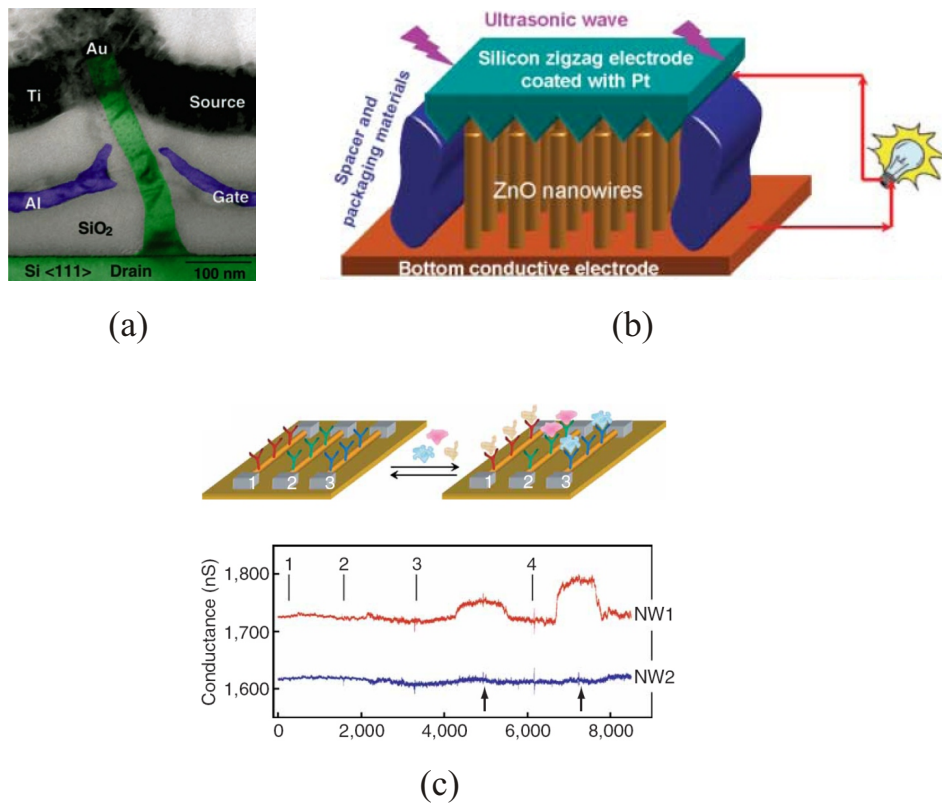
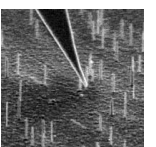


**Figure 3.1:** Novel devices based on nanowires. (a) Silicon surround gate FET (from Schmidt<sup>84</sup>); (b) Nanogenerator out of ZnO nanowires (from Wang<sup>106</sup>); (c) silicon nanowires used as cancer detectors (from Zheng<sup>116</sup>).



been the only ones to succeed experimentally.<sup>37</sup> At still relatively low strains, they find the piezoresistance of the silicon nanowire to be much higher than that of bulk silicon. All other work published is computational<sup>40,55</sup>, but Shiri *et al* reveal the interesting property that the indirect bandgap changes to a direct one under certain strains for nanowires of different sizes and orientations<sup>89</sup>.

### 3.1.2 Doping of nanowires

Typically, silicon nanowires reveal a *p* type conductance when they are grown in the VLS process without adding any dopant on purpose, although the resistivity is relatively high ( $2\ \Omega\text{cm}$ <sup>107</sup>– $400\ \Omega\text{cm}$ <sup>18</sup>). For their use in electronic applications, doping is, however, an important issue. By adding carrier gases containing a dopant in the VLS process, nanowires can be doped during their growth. But also nominally undoped nanowires can be post growth doped by vapor phase doping, spin-on-dopant technology or by ion beam implantation.

Cui *et al* were the first to dope silicon nanowires by adding diborane ( $\text{B}_2\text{H}_6$ ) to the gas flow or placing a Au–P target and additional red phosphorus at the reactant gas inlet for *p* and *n* type doping, respectively.<sup>18</sup> Lew *et al* have investigated trimethylboron ( $\text{B}(\text{CH}_3)_3$ ) as an alternative to diborane.<sup>56</sup> For both sources, doping concentrations of  $1 \times 10^{18}$  to  $4 \times 10^{19}\ \text{cm}^{-3}$  were obtained by varying the inlet dopant/ $\text{SiH}_4$  gas ratio. TEM studies revealed a 30 nm wide crystalline core with a 30 nm thick  $\text{SiO}_2$  shell for the diborane doped nanowires, while the trimethylboron doped ones had a core diameter of 50 nm covered by a thin oxide layer of only 2 nm. The different nanowire structures obtained were explained by comparing the thermal stability and reactivity of the two sources with  $\text{SiH}_4$ . Wang *et al* have investigated phosphine ( $\text{PH}_3$ ) as an *n* type dopant source for Au-catalyzed VLS growth of phosphorus-doped silicon nanowires.<sup>107</sup> Transmission electron microscopy characterization revealed that the as-grown Si nanowires were predominately single crystal even at high phosphorus concentrations. Four-point resistance and gate-dependent conductance measurements confirmed that electrically active phosphorus was incorporated. A transition was observed from *p* type conduction for nominally undoped to *n* type conduction upon the introduction of  $\text{PH}_3$  to the inlet gas. The resistivity of the *n* type nanowires decreased by approximately 3 orders of magnitude (from  $2\ \Omega\text{cm}$  to  $6\ \text{m}\Omega\text{cm}$ ) as the inlet  $\text{PH}_3/\text{SiH}_4$  gas ratio was increased from  $2 \times 10^{-5}$  to  $2 \times 10^{-3}$ .

Yang *et al* have further developed the doping process with phosphine to axially modulate the doping concentration.<sup>111</sup> By changing the flowrate of phosphine during the growth process, they can alternate between *n* and *n*<sup>+</sup> regions, which was demonstrated by scanning gate microscopy. Gudixsen *et al* have changed the doping profile from *n* to *p* type during VLS growth of silicon nanowires with silane by changing from phosphine to diborane during growth.<sup>33</sup> The *p-n* junction within the nanowire was characterized electrically and by scanning gate microscopy as well as electrostatic force microscopy. Tang *et al* grew nanowires with  $\text{Si}_2\text{H}_6$  in the VLS process, and also changed the doping profile by introducing alternatively arsenic and diborane.<sup>98</sup>

Thermal diffusion of the metal catalyst into the nanowires at 750–850 °C in a flowing 95/5 Ar/ $\text{H}_2$  environment was used by Yu *et al* for post growth doping of silicon nanowires.<sup>113</sup> Both Au and Zn was investigated, and Au nucleated nanowires exhibited resistivity values much

lower than those of similarly treated Zn nucleated nanowires. While Au, a  $p$  type dopant in silicon, can increase the carrier density, it may also decrease the carrier mobility because it acts as a scattering center. Byon *et al* have doped nanowires after they have been grown via vapor phase doping using bismuth vapor in evacuated quartz tubes.<sup>10</sup> As grown nanowires were placed a few inches away from bismuth powder in a quartz tube which was pumped down to a vacuum of  $10^{-6} - 10^{-7}$  Torr, and then sealed under a dynamic vacuum. The sealed quartz tube was annealed in a furnace at 1000 °C for 1 h to vaporize the bismuth source and achieve dopant diffusion into the nanowires. The doping concentration was not measured, but electrical characterization in a FET configuration showed  $n$  type behavior, while as grown nanowires were  $p$  type.

Ion beam implantation is used by Ronning *et al* to dope nanowires standing perpendicular to the substrate with boron and phosphorus. By varying the doses and acceleration voltages, uniform  $n$  and  $p$  type doping as well as  $p$ - $n$  profiles are achieved along the nanowire axis. Section 3.5.3 describes this process in more detail.

Doping nanowires consists not only of incorporating dopants into the crystal lattice, but also of verifying if the dopants are electrically active. Whereas the former often consists of "only" introducing an additional gas into the growth chamber, the latter requires sophisticated technology to contact the nanowires. This is more challenging than it appears in the literature, as contact properties and reproducibility are often not discussed. The next section introduces the reader to this field.

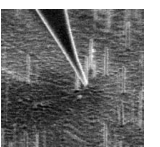
## 3.2 Considerations on the characterization of nanowires

This section shall provide an overview of what this work deals with in terms of electrical characterization. Some basic parameters of the nanowire itself and its contact properties are calculated first, followed by a presentation of the contact characteristics that can be expected. Next, the 4 point measurement concept is introduced and the measurement instrument is examined for its suitability in the measurement of nanowires. The last three subsections treat some effects that may distort the results, namely the effect of electric power dissipation via the nanowires' temperature, the influence of fixed charges at the nanowire surface and the presence of high electric fields.

### 3.2.1 Nanowire resistance and number of charge carriers present

The lowest possible carrier concentration that can be expected arises from thermally excited charge carriers in absence of any dopants. At room temperature, this intrinsic charge carrier concentration is  $n_i = 10^{10} \text{ cm}^{-3}$ . An upper limit is the doping concentration at which the Fermi level aligns with the conduction or the valence band. This occurs at  $n \approx 10^{19} \text{ cm}^{-3}$ .<sup>96</sup> Beyond this concentration, the semiconductor is called degenerate and presents a metallic behavior as the carrier concentration becomes independent of temperature.

The resistivity  $\rho$  depends on both the doping concentrations ( $n$ ,  $p$ ) and the mobility  $\sigma$  of the charge carriers,  $\rho = [q(\sigma_n n + \sigma_p p)]^{-1}$ . Figure 3.2 plots the resistance  $R = \rho \times 4l/d^2\pi$  for a nanowire with diameter  $d = 100 \text{ nm}$  and length  $l = 1 \text{ }\mu\text{m}$ , assuming the mobility of bulk silicon, and neglecting surface effects. Without knowing anything about the nanowires' doping





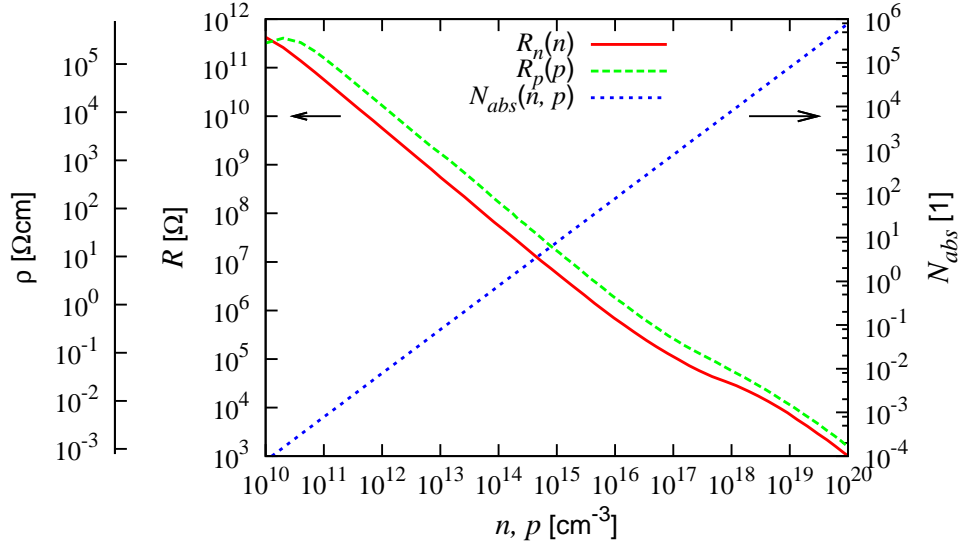


**Figure 3.2:** Resistance and the absolute number of charge carriers in a  $1\ \mu\text{m}$  long and  $100\ \text{nm}$  wide silicon nanowire in function of its doping concentration. The outer left y-axis shows the resistivity of bulk silicon, with which the resistance was calculated (values from Sze<sup>96</sup>).

concentration, one can expect its resistance to lie somewhere between  $1\ \text{k}\Omega$  and  $500\ \text{G}\Omega$ . The plot also shows the absolute number of charge carriers,  $N_{abs} = n \times ld^4\pi/4$ , present in the nanowire, averaged over time. Note that for doping concentrations below  $10^{14}\ \text{cm}^{-3}$ , less than 1 charge carrier is present.

### 3.2.2 Contact characteristics

The nature of a metal–semiconductor contact depends on both doping level and temperature. Referring to Fig. 3.3 the components of the current can be categorized into three types: (1) thermionic emission (TE) over the barrier, (2) field emission (FE) near the Fermi level, and (3) thermionic–field emission (TFE) at an energy between TE and FE. A rough criterion for the relative contributions of these components can be set by comparing the thermal energy  $kT$  to  $E_{00}$ , which is defined as<sup>96</sup>

$$E_{00} \equiv \frac{q\hbar}{2} \sqrt{\frac{N}{m^*\epsilon_s}} \quad , \quad (3.1)$$

where  $q$  is the elementary charge,  $\hbar$  Planck’s constant,  $N$  the doping concentration,  $m^*$  the effective mass of electrons and  $\epsilon_s$  the dielectric constant of silicon.

When  $kT \gg E_{00}$ , TE dominates. This means that thermally excited charge carriers that surpass the so called Schottky barrier are the main current contribution. This situation is sketched in Fig. 3.4(a). When  $kT \ll E_{00}$ , the Schottky barrier becomes thin enough so that the charge carriers can tunnel through it. In this case FE dominates, as sketched in Fig. 3.4(c). When  $kT \approx E_{00}$ , TFE is the main mechanism. In this combination of TE and FE, thermally



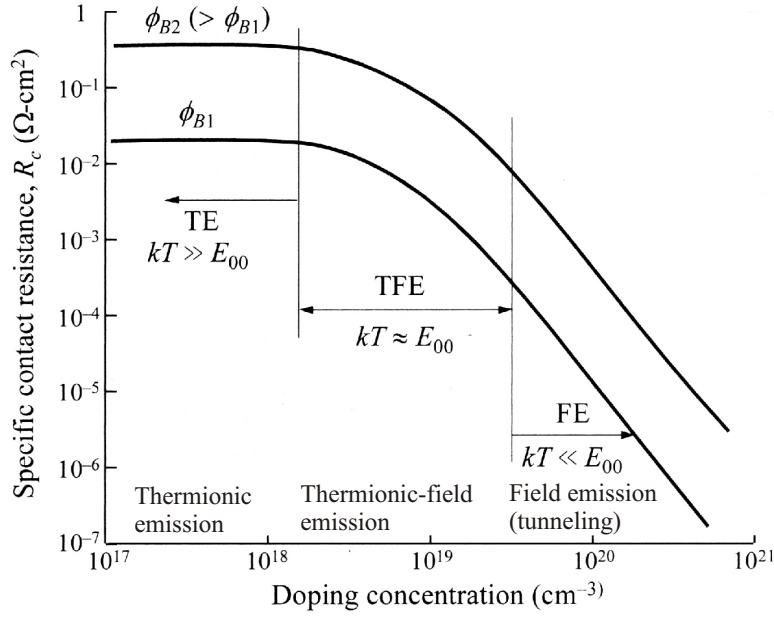


**Figure 3.3:** Dependence of specific contact resistance on doping concentration, barrier height and temperature. Regimes of TE, TFE and FE are indicated. From Sze<sup>96</sup>.

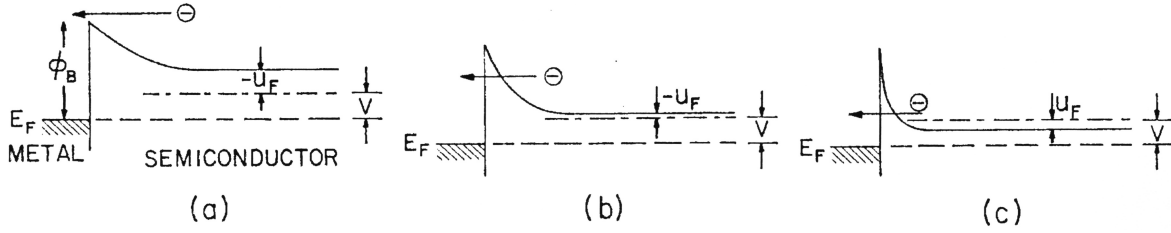
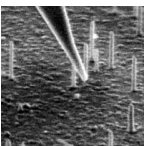


**Figure 3.4:** Band diagrams of metal n type semiconductor under forward bias: (a) semiconductor lightly doped,  $kT/E_{00} \gg 1$ , TE, (b) semiconductor heavily doped,  $kT/E_{00} \approx 1$ , TFE, (c) semiconductor very heavily doped (degenerate),  $kT/E_{00} \ll 1$ , FE. From Yu<sup>112</sup>.

excited charge carriers reach an energy level where the barrier is thin enough in order to tunnel through, as illustrated in Fig. 3.4(b). At room temperature, the doping level  $N$  for which  $kT = E_{00}$  is  $N = 6.9 \times 10^{18} \text{ cm}^{-3}$ . Thus, the FE regime is expected to occur only for degenerate semiconductors.

An ohmic contact is defined as a metal–semiconductor contact that has a negligible junction resistance relative to the total resistance of the semiconductor device. An important figure of merit for ohmic contacts is thus the contact resistance, defined as the reciprocal of the derivative of the current density with respect to the voltage across the interface, evaluated at zero bias<sup>96</sup>:

$$R_c \equiv \left( \frac{dJ}{dV} \right)_{V=0}^{-1}, \quad [\Omega \text{cm}^2]. \quad (3.2)$$



In the TE regime where  $kT \gg E_{00}$ , from the thermionic-emission-diffusion theory one gets<sup>96</sup>

$$R_c = \frac{k}{A^{**}Tq} \exp\left(\frac{q\phi_{Bn}}{kT}\right) \quad (3.3)$$

where  $A^{**}$  is the reduced effective Richardson constant and  $\phi_{Bn}$  the Schottky barrier height. In the TFE region where  $kT \approx E_{00}$ , the contact resistance is given by<sup>79</sup>

$$R_c = \frac{k\sqrt{E_{00}} \cosh(E_{00}/kT) \coth(E_{00}/kT)}{A^{**}Tq\sqrt{\pi q(\phi_{Bn} - \phi_n)}} \exp\left[\frac{q(\phi_{Bn} - \phi_n)}{E_{00} \coth(E_{00}/kT)} + \frac{q\phi_n}{kT}\right] \quad (3.4)$$

where  $q\phi_n$  is the energy difference between the Fermi level and the conduction band (negative for degenerate semiconductors). When field emission is the dominant process ( $kT \ll E_{00}$ ), the contact resistance becomes<sup>79</sup>

$$R_c = \frac{k \sin(\pi c_1 kT)}{A^{**}\pi qT} \exp\left(\frac{q\phi_{Bn}}{E_{00}}\right) \quad (3.5)$$

where  $c_1$  is defined as

$$c_1 \equiv \frac{1}{2E_{00}} \log\left[\frac{4\phi_{Bn}}{-\phi_n}\right]. \quad (3.6)$$

The specific contact resistance for different barrier heights and doping concentrations is plotted in Fig. 3.5. For the calculations the parameters of  $n$  type doping were taken with  $A^{**} = 120 \text{ cm}^{-2}\text{K}^{-2}$ ,  $m^* = 0.5m_0$ , and  $T = 300 \text{ K}$ . The second  $y$  axis on the right shows the contact resistance for a 200 nm long contact on a 100 nm wide nanowire. This contact resistance may be compared to the resistance of a 1  $\mu\text{m}$  long, 100 nm thick nanowire, plotted with the black dashed-dotted line. If the contact resistance is comparable or larger than the nanowire resistance, 4 point resistance measurements have to be performed in order to accurately extract the resistance of the nanowire. This is subject of Sect. 3.2.3.

When the electrode metal makes contact with the semiconducting nanowire, a depletion layer forms. For an infinitely wide contact on a  $n$  type semiconductor its width is<sup>96</sup>

$$W_D = \sqrt{\frac{2\epsilon_s}{qN_D} \left(\psi_{bi} - V - \frac{kT}{q}\right)} \quad (3.7)$$

where  $\psi_{bi}$  is the built-in potential, defined as  $\psi_{bi} = \phi_{Bn} - (E_C - E_F)/q = \phi_m - \chi - (E_C - E_F)/q$  with  $\phi_{Bn}$  being the barrier height (accounting for image-force lowering), and  $\phi_m$  and  $\chi$  the work functions of the metal and the semiconductor, respectively. The depletion width in function of the doping concentration for  $n$ -doped silicon is plotted in Fig. 3.6. Curves for different bias conditions are plotted for a barrier height of  $\phi_{Bn0} = 0.5 \text{ V}$  (barrier height before taking into account image-force lowering). For other barrier heights, the depletion widths can be read by keeping  $V_F - \phi_{Bn0}$  constant, e.g. the dashed green curve represents also an unbiased junction with a barrier height of 0.3 V. Although the model used for these curves assumes a planar contact area, it becomes clear that at doping concentrations below  $10^{17} \text{ cm}^{-3}$  the depletion width becomes in the order of magnitude of the dimensions of the nanowire and thus cannot be ignored.

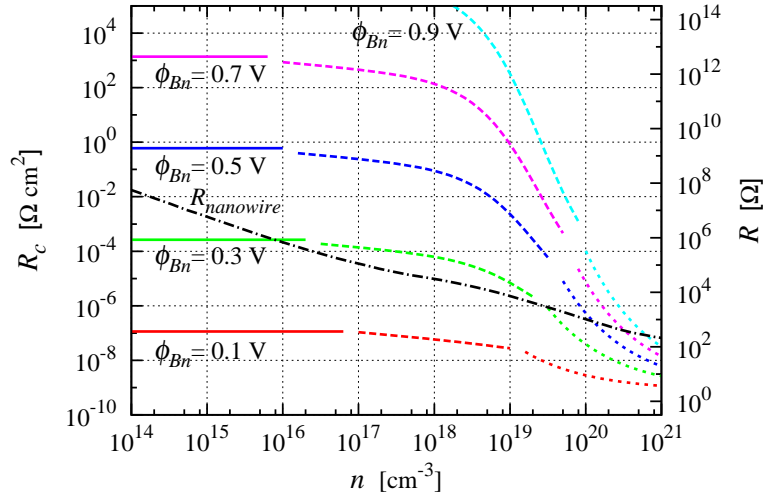


**Figure 3.5:** The specific contact resistance plotted for different barrier heights in function of the doping concentration. Solid lines represent the TE regime (Eq. 3.3), dashed lines the TFE regime (Eq. 3.4) and dotted lines the FE regime (Eq. 3.5). On the right hand y axis the resistance of contact in  $\Omega$  for a 200 nm wide contact on a 100 nm thick nanowire is indicated. For comparison, the resistance of a 100 nm wide, 1  $\mu\text{m}$  long nanowire is also represented by the black dash—dotted line (right hand y axis).

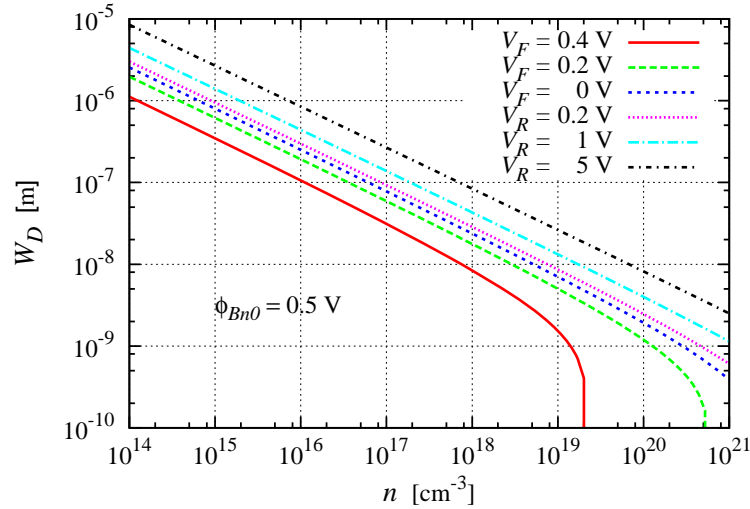


**Figure 3.6:** The depletion width of a metal–semiconductor contact in function of the doping concentration for different bias conditions, accounting for the image–force lowering, with  $\phi_{Bn0} = 0.5$  V.



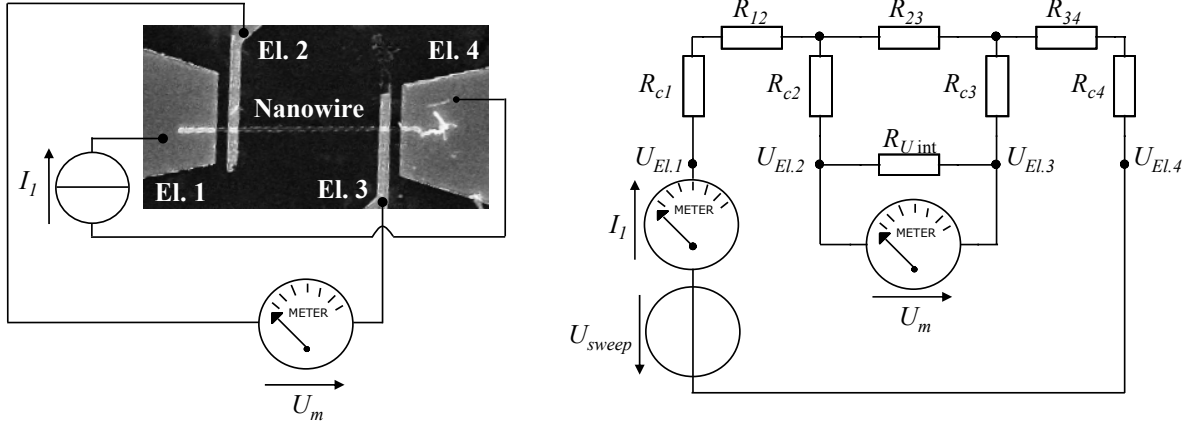


**Figure 3.7:** Left: Principle of the 4 point resistance measurement. Right: Schematic including the contact resistances  $R_{ci}$  and the internal resistance of the voltage measurement unit  $R_{U_{int}}$ .

Luscombe *et al* have calculated theoretically the depletion layer width for a radial geometry.<sup>64</sup> They have shown that the depletion width satisfies the inequality  $W_p \leq W(r) \leq R_c$ , where  $W_p$  is the depletion width at a planar interface, and  $R_c = \sqrt{2}W_p$  is a critical radius below which the structure is fully depleted. The standard result  $W_p$  therefore underestimates the depletion length in a finite structure. The discrepancy between  $W(r)$  and  $W_p$  become significant when the dimensions of the structure becomes comparable to the depletion length, as can occur in nanowires, but does not exceed a factor of  $\sqrt{2}$ .

### 3.2.3 4 point resistance measurements

When the contact resistance is in the order of, or greater than, the resistance of the nanowire, 4 point resistance measurements have to be performed. This method is also called the Kelvin resistance measurement (Fig. 3.7). A current is induced through the outer electrodes (1 and 4) and the voltage drop is measured between the inner electrodes. Because the input resistance of the voltage meter is high, the current through, and the voltage drop over contacts 2 and 3 are small. The resistance of the nanowire section between electrodes 2 and 3 can then be calculated by  $R_{23} = U_{23}/I_{14}$ .

However, for an accurate measurement two conditions must be met. From the schematic in Fig. 3.7 they are found to be the following:

- $R_{U_{int}} \gg R_{c2} + R_{c3}$  insures that the voltage drop over the contacts can be neglected.
- $R_{23} \ll R_{c2} + R_{c3} + R_{U_{int}}$  insures that the current injected into electrode 1 flows through the nanowire and not via the contacts through the voltage measurement unit.

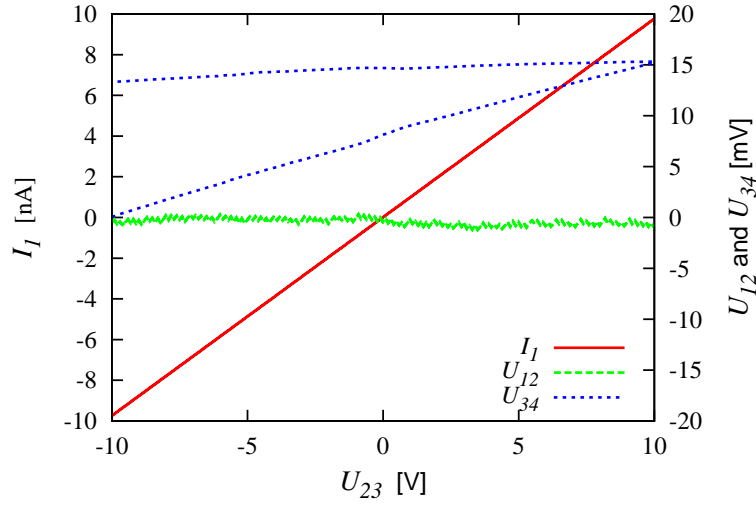


**Figure 3.8:** Test of the HP Semiconductor Analyzer HP4156B. The red solid line plots the injected current versus the voltage drop over the inner electrodes, its slope yields the resistance  $R_{23}$  (left hand scale). The green dashed and blue dotted lines plot the voltage drops between electrodes 1–2 and 3–4, respectively (right hand scale).

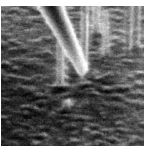
### 3.2.4 Characteristics of the electrical measurement instrument

The instrument used is a HP Semiconductor Analyzer HP4156B, which has four independent source–measure units (SMU). To measure the voltage drop over the inner electrodes, SMUs 2 and 3 are programmed to impose 0 current and to measure the voltage with respect to ground. The SMUs are specified to be able to measure currents down to 10 fA, but to check if they are also able to regulate such small currents, a setup with very high resistances is put in place.

A piece of white paper,  $1 \times 5 \text{ cm}^2$  in size, serves as a high impedance resistor. In a two point measurement (impose voltage, measure current) its resistance is determined to be  $2.2 \text{ T}\Omega$  before and after the 4 point test measurement. Referring to Fig. 3.7, the test resistor is set in place of the contact resistance  $R_{c3}$ , and a commercial  $1 \text{ G}\Omega$  resistance is put in place of the nanowire center section  $R_{23}$ . All other resistances are short–circuited.

Figure 3.8 shows the current injected into electrode 1 in the four point configuration ( $I_1$ , red solid curve) and the voltage drops between electrodes 1–2 and 3–4 (green dashed and blue dotted curves, respectively) in function of the voltage drop between the inner electrodes. From the slope of the  $U$ – $I$  curve, the resistance is calculated to be  $1.025 \text{ G}\Omega$ . This is within the tolerance of the resistor (5%) and corresponds to the value measured without the paper resistor included (not shown here).

The voltage drops between electrodes 1–2 and 3–4 would ideally be zero. The fluctuations in  $U_{12}$  originate from the noise picked up in the cables from the analyzer to the probe station. The variations in  $U_{34}$  are much greater and reach up to 15 mV. This is the voltage drop induced over the paper resistor due to the offset current  $I_3$ . The voltage is increasing as the offset current charges the cable capacitance. Because this cable capacitance is unknown, the offset



	Si bulk <sup>96</sup>	Si nanowire <sup>57</sup>	SiO <sub>2</sub> <sup>96</sup>	Air	Au
Thermal diffusivity $k$ [cm <sup>2</sup> s <sup>-1</sup> ]	0.9		0.006	0.21	1.28
Thermal conductivity $C$ [Wcm <sup>-1</sup> K <sup>-1</sup> ]	1.56	≈ 0.1	0.014	0.00026	3.17

**Table 3.1:** Thermal coefficients of Si, SiO<sub>2</sub>, Au and air at room temperature.

current  $I_3$  cannot be quantified. But an upper limit can be set by dividing the maximum voltage offset by the resistance of the piece of paper,  $I_3 < U_{23,\max}/R_{c3} = 7$  fA.

This result implies that if the voltage drop over a section of the nanowire is to be measured with an accuracy of 10 mV, the contact resistance must not be greater than 1.4 TΩ. Referring to Fig. 3.5, such high contact resistances are expected only for barrier heights  $> 0.6$  eV.

### 3.2.5 Heating of the nanowire

Because of the small dimensions of a nanowire, it is not obvious how power dissipation affects its temperature. In this section the geometry of a silicon nanowire lying on a SiO<sub>2</sub> substrate and connected at both ends to Au electrodes is considered. The thermal diffusivity and conductivity of silicon, silicon dioxide, gold and air are listed in Tab. 3.1. SiO<sub>2</sub> and air both have a much lower thermal diffusivity than silicon and gold. In order to simplify the problem, two assumptions are made: (i) all the heat is assumed to be extracted via the metal electrodes, i.e. there is no heat flow from the nanowire to the air or the substrate; (ii) because the gold electrodes are large compared to the nanowire, and their heat diffusivity is larger, too, they are considered to be perfect heat sinks, which means that they stay at room temperature.

The geometry left is a nanowire at a constant temperature on both sides, which can be treated one dimensionally. The heat equation is formulated with an additional internal heat generation function,

$$\frac{\partial u(t, x)}{\partial t} - k \frac{\partial^2 u(t, x)}{\partial x^2} - q(t, x) = 0 \quad , \quad (3.8)$$

where  $u(t, x)$  is the heat per unit volume,  $k$  is the thermal diffusivity and  $q(t, x)$  is the heat generated per unit volume at a given rate. In the present problem,  $q$  is constant throughout the nanowire,  $q(x, t) = UI/(ld^2\pi/4)$ , where  $UI$  is the electric power dissipated and  $l$  and  $d$  are the length and the width of the nanowire. In App. A the initial and boundary conditions are formally stated and a MATLAB script is given which solves the problem. Here the solutions are presented and discussed.

Figure 3.9 shows how the temperature evolves in a 1 μm long, 100 nm wide nanowire in function of time and position when a current of 1 μA passes at 1 V applied, assuming the nanowire has the same thermal properties as bulk silicon. The temperature rise in the nanowire center is only 0.1 °K, and the steady state temperature is already reached after 5 ns.

Li *et al* investigated the thermal conductivity of silicon nanowires by suspending them on a micro electromechanical system (MEMS) device.<sup>57</sup> They found the conductivity to be diameter dependent, ranging from 6 Wm<sup>-1</sup>K<sup>-1</sup> for a 22 nm to 40 Wm<sup>-1</sup>K<sup>-1</sup> for a 115 nm wide nanowire. This is more than 10 times less than the bulk value. The strong diameter dependence of thermal conductivity in nanowires is ascribed to the increased phonon–boundary scattering

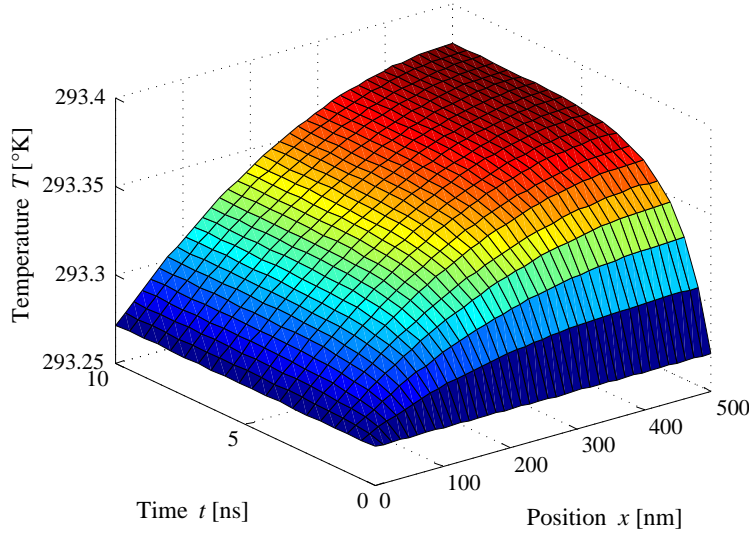


**Figure 3.9:** Heating of a 1  $\mu\text{m}$  long, 100 nm wide nanowire in function of time and position due to electrical power dissipation at a current of 1  $\mu\text{A}$  and a Voltage of 1 V.

and possible phonon spectrum modification for the thinnest nanowires. If this lower thermal diffusivity is taken into account, the temperature rises by 2 °K within 100 ns, which is still insignificant.

As the temperature rises very fast, the steady state condition can be investigated. Setting  $\partial u(t, x)/\partial t = 0$  in Eq. 3.8, and applying the boundary conditions discussed above and stated in App. A, the maximum temperature rise at the center of the nanowire is

$$\Delta T = \frac{ql^2}{8C} = \frac{UIl}{2\pi d^2 C} \quad (3.9)$$

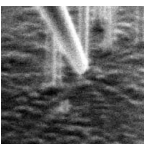
where  $C = kcp$  is the thermal conductivity ( $c$  is the specific heat and  $\rho$  the density of the material).

The 0.1 °K obtained for the parameters described above may thus increase to a more important value as  $\Delta T$  rises linearly with electric power and the length of the nanowire, and is inversely proportional to the square of the nanowire diameter. For the experiments presented in later sections, however,  $\Delta T$  remains moderate.

### 3.2.6 Influence of the nanowire surface

When the size of a device is reduced, its surface to volume ratio becomes larger. At the surface, two effects influence the electrical characteristics of a semiconductor:

- Discontinuities in the lattice periodicity are scattering centers for charge carriers. They reduce the mobility in proximity of the surface.
- Oxide charges and interface traps exist at the nanowire surface. In addition, high electric fields or the EBeam of the SEM inject hot charge carriers into the oxide, which remain





trapped therein. These surface charges may deplete a part of the semiconductor, leading to a thinning of the effective cross section of the nanowire.

Let us first consider the influence of the surface through scattering. In bulk silicon, the presence of acoustic phonons and ionized impurities result in carrier scattering that significantly affect the mobility of the charge carriers. The mean free path  $\lambda_m$  is related to the mobility by

$$\lambda_m = \frac{\sqrt{3kTm^*}}{q} \mu \quad (3.10)$$

Depending on doping concentration and doping type, the mobility in silicon varies from 100 to 1400 cm<sup>2</sup>V<sup>-1</sup>s<sup>-1</sup> and  $\lambda_m$  lies between 5–65 nm. Because for thin nanowires this mean free path is comparable to the nanowire diameter, scattering at its surface must be taken into account. Matthiessen's rule states the combined mobility to be

$$\mu = \left( \frac{1}{\mu_l} + \frac{1}{\mu_i} + \frac{1}{\mu_s} \right)^{-1} \quad (3.11)$$

where  $\mu_l$ ,  $\mu_i$  and  $\mu_s$  are the mobilities from interaction with acoustic phonons of the lattice, from ionized impurities and from the surface, respectively.

When calculating an average resistivity  $\rho$  from the nanowire dimensions and the measured resistance, the doping concentration can be calculated assuming the mobility from bulk silicon. However, because the mobility is expected to be inferior to that of bulk, the actual doping concentration might be higher than the calculated one.

Next the effect of surface charges is discussed. The nanowire surface is successively covered by (i) a layer of native SiO<sub>2</sub>, which is single-crystal silicon, (ii) a monolayer of SiO<sub>x</sub>, that is, incompletely oxidized silicon, and (iii) a thin strained region of SiO<sub>2</sub>, and the remainder, being stoichiometric, strain-free, amorphous SiO<sub>2</sub>. First, in the Si-SiO<sub>2</sub> interface, interface traps with energy states in the silicon bandgap are present. These can exchange charges with silicon in a short time, so their occupancy is dependent on the Fermi level. Interface traps can possibly be produced by excess silicon, broken Si-H bonds, excess oxygen, and impurities. Second, fixed oxide charges are located at or near the interface. These are immobile under an applied electric field. Third, oxide trapped charges can be created, for example, by EBeam irradiation or hot-electron injection. These traps are distributed inside the oxide layer.

The fixed oxide charges have been investigated for nanowires by two groups. Seo *et al* have measured the surface state density on VLS grown silicon nanowires with a native oxide to be  $2.3 \times 10^{12}$  cm<sup>-2</sup>, derived from conduction measurements on nanowires with different diameters.<sup>87</sup> A similar value of  $2.6 \pm 0.75 \times 10^{12}$  cm<sup>-2</sup> was found by Kimukin *et al*.<sup>48</sup>

The model applied to calculate the charge density is based on the charge neutrality of the nanowire. The surface charge is compensated by depletion or accumulation of charges in the semiconductor. For a positive surface charge density,  $N_s$ , on a *p* type semiconductor with a doping concentration of  $N_a$ , the effective cross-section of the nanowire is reduced to<sup>87</sup>

$$A_{eff} = A_{measure} \left( 1 - \frac{4N_s}{dN_a} \right) \quad (3.12)$$



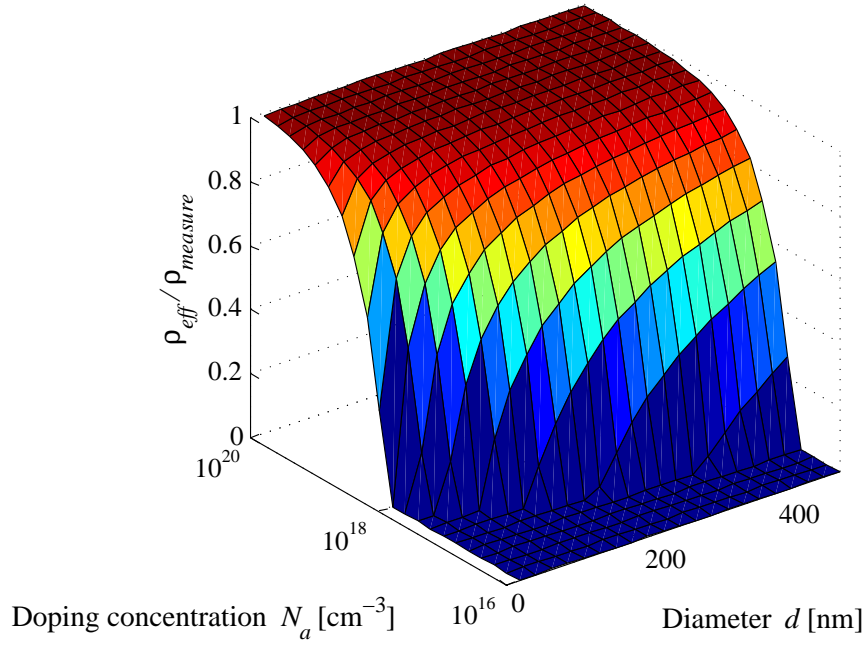
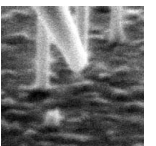


**Figure 3.10:** The ratio of the effective over to the measured resistivity, taking into account the influence of surface charge present in the native oxide. A surface charge density of  $2.3 \times 10^{12} \text{ cm}^{-2}$  is assumed.<sup>87</sup>

by the depletion region, where  $A_{eff}$  and  $A_{measure}$  are the effective and the total cross-sections, respectively, and  $d$  is the total diameter. As the resistivity (calculated from an experiment) is directly proportional to the cross-section,  $\rho = RA/l$ , the effective and measured resistivities stand in the same relation as the effective and measured cross-sections. Figure 3.10 plots the ratio  $\rho_{eff}/\rho_{measure}$  in function of doping concentration and diameter of the nanowire, assuming a surface charge density of  $N_s = 2.3 \times 10^{12} \text{ cm}^{-2}$ . It can be seen that only for high doping concentrations,  $N_a \gtrsim 10^{19} \text{ cm}^{-3}$ , the depletion region is small enough not to affect the effective cross-section. Already for a doping concentration of  $10^{18} \text{ cm}^{-3}$  and diameter of 100 nm, the depletion region affects the apparent resistivity by a factor of 0.8. However, the absolute value of  $\rho_{eff}/\rho_{measure}$  is strongly affected by the surface charge density. The two values for the surface charge density reported in literature correspond well to each other, but they might not be representative in general.

### 3.2.7 High-field effects

At low electric fields, the drift velocity in a semiconductor is proportional to the field and the proportionality factor is the mobility. When the fields are sufficiently large, however, nonlinearities in mobility are observed. This is because the carriers on average start to acquire more energy than they have at thermal equilibrium, and this energy is lost in scattering events with phonons. Fig. 3.11 shows the carrier drift velocity versus the applied electric field.



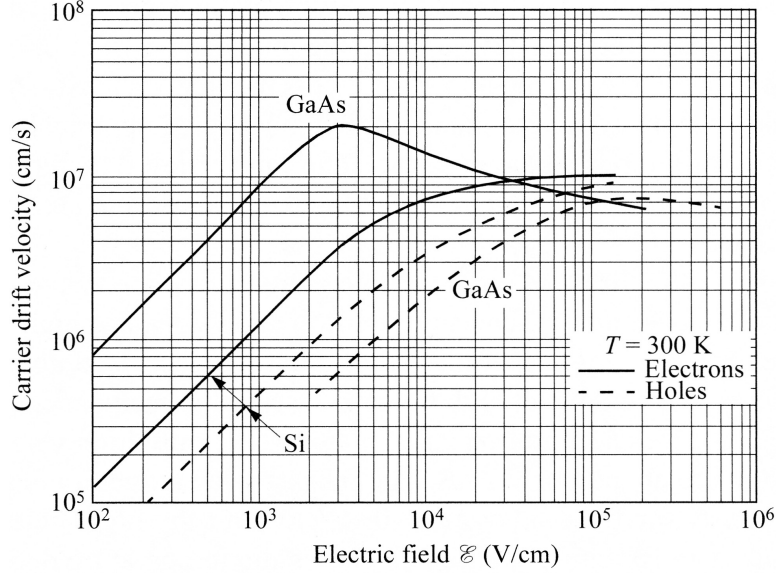


**Figure 3.11:** Measured carrier velocity versus electric field for high-purity Si and GaAs. For highly doped samples, the low-field velocities (mobilities) are lower than indicated here. In the high-field region, however, the velocity is essentially independent of doping. (From Sze<sup>96</sup>)

At  $10^4 \text{ Vcm}^{-1}$ , which corresponds to  $1 \text{ V}\mu\text{m}^{-1}$ , the drift velocity starts to deviate from its linear dependence. When calculating the doping concentration from a measured resistivity at high electric fields, one has to bear in mind that the lower effective mobility leads to an underestimation of the charge carrier density.

At still larger fields, electrons may acquire an energy higher than the band gap, and impact ionization occurs. The increased number of carriers then leads to an abrupt drop in resistivity, called avalanche breakdown.

### 3.3 Measurement techniques and their difficulties

The next sections present two successful measurement techniques for different kinds of nanowires and examined properties. But in terms of time spent, a PhD student's work consists more trying numerous possibilities to find the right experiment rather than its execution. The present section shall thus briefly elucidate the difficulties and illustrate some experiments that failed.

Langford *et al* give a comparison of different methods to contact nanowires,<sup>52</sup>: contacting nanowires with a tip on a nanomanipulator, by evaporating metal via EBeam lithography, by dropcasting nanowires on prefabricated electrodes, and by depositing electrodes with a FIB. Their advantages and disadvantages are discussed in terms of yield and effort. They also compare results from contacting gold nanowires and multi walled carbon nanotubes to those in the literature, but cannot conclude on the reliability of the different methods. Stern *et al* compare optical and electron beam lithography in terms of formation of an ohmic contact, applied to

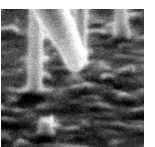
GaN,  $\text{In}_2\text{O}_3$  and carbon nanotubes.<sup>93</sup> In order to render the metal-semiconductor contacts Ohmic, e-beam-processed devices are found to require a postfabrication, high-temperature anneal, whereas the use of an oxygen plasma prior to metallization is found to be crucial for devices defined by optical lithography. Gu *et al* present a theoretical model to extract the resistance of a nanowire in a four point configuration when the contact resistance over the inner electrodes is not negligible.<sup>31</sup> In their calculations, however, they assume that the contact characteristics are symmetrical, so it does not apply to Schottky contacts, contrary to what they state. They tested the method solely on copper nanowires with a linear contact characteristic. Lin *et al* finally presented a 4 point probe mounted on a nanomanipulator with nanowires as end effectors for multiprobe measurements on fragile nanostructures.<sup>60</sup> It is, however, tested on thin Au films, and not on nanowires.

A measurement technique ideally is reliable, reproducible, time efficient, and flexible in terms of examined material, structure and properties. As a long term goal is the electromechanical characterization of nanowires, it is sensible to build a manipulation setup with which the nanowire can be contacted electrically, and deformed mechanically at the same time. Such a tool is in fact developed during this work, and presented below. However, reliability and reproducibility issues urged us to switch to other techniques.

The mentioned setup consists of an atomic force microscope (AFM) tip on a nanomanipulator that is built into an SEM. This AFM tip can be used to contact a single nanowire, which is standing, as grown, on a silicon substrate, which in turn forms the second contact. One can imagine pushing on the nanowire with the tip, performing a compression experiment while measuring the electric conduction; or somehow attaching the nanowire on the tip and pulling on it to perform a tensile experiment.

Nanowires are indeed contacted in this way. However, the current–voltage curves extracted are non-linear, indicating a non-ohmic contact, and not reproducible, neither from nanowire to nanowire nor from sweep to sweep. As it becomes clear from the discussions of the previous section, contact properties play a major role when characterizing nanowires electrically. Reasons for the unreproducible measurements could be following:

- The AFM tip–nanowire contact is mechanically not stable. A drift in the setup causes the tip to move with respect to the nanowire, resulting in different contact areas and thus to unreproducible measurements.
- The AFM tip material is not stable. The AFM tip itself is, in this case, made of heavily *n*-doped silicon. To enhance the conductance and to make a better contact, Ti, Au and Pt coatings are deposited by sputtering, and the blank Si tip is tested as well. When a metal is deposited with a nominal thickness of around 100 nm, it is not clear how much metal is deposited on the tip apex. Also, scratching the tip against nanowires in an attempt to contact them may scratch off the deposited metal, which leads to unreproducible measurements. The SEM resolution does not permit verification of the tip condition.
- The native oxide on the nanowires is etched away in some experiments prior to installing the sample into the SEM and evacuating. During the transfer to the SEM (1 min) and



evacuation (10 min), however, a new oxide may form that leads to a bad electrical contact. Doped diamond coated AFM tips are tested in order to scratch off some remaining oxide on the nanowire, but without the expected results.

- Electron beam induced contamination deposition during observation may lead to an isolating carbonaceous layer on the nanowire and the AFM tip. This layer may not be important for the first measurement, but thickness increases with observation time, leading again to unreproducible measurements.
- The non-linearity can be an inherent property of the metal–semiconductor interface because of the formation of a Schottky barrier. In order to make contact independent measurements, four contacts would have to be applied to a single nanowire. If the nanowire is not too short, this is not an impossible task, even with manipulators.<sup>61</sup> However, the above mentioned difficulties (drift and tip stability) and the complications that come up when trying to combine the electrical measurement with a mechanical manipulation with four tips discourage us to pursue this idea.

The standard technique of contacting nanowires is the deposition of electrodes by EBeam lithography. The two great advantages are that the experiments are reproducible and that four or more contacts can be made in the same run, provided the resolution of the process is high enough. This is thus applied to investigate the doping concentration of nanowires doped during growth, as presented in Sect. 3.4. Disadvantages of EBeam lithography are that (i) the nanowires need to be long enough, (ii) it is a time consuming process and requires expensive tools, and (iii) it is not flexible in the sense that the nanowires are mechanically fixed.

For very short nanowires, the nanomanipulation setup is thus used to contact them. Instead of an AFM tip, an electrochemically etched PtIr wire tip is used. This yields a better electrical contact; mechanical manipulations, however, cannot be performed with it. While the electrical contact does not permit the measurement of the exact doping concentration, electron beam induced current (EBIC) imaging is used to demonstrate the effective doping. This is presented in Sect. 3.5.

Finally, to perform electromechanical experiments, a whole new concept is introduced. The nanowires are grown epitaxially in a silicon trench, providing ohmic contacts on both sides. The manipulation setup is then used to strain the nanowire by pushing on a cantilever whose surface is one of the trench sidewalls. This device is presented in Chapter 5.

### 3.4 Determination of the doping concentration

The doping concentration of silicon nanowires is determined by measuring their resistivity in a 4 point resistance measurement. The nanowires undergoing testing are contacted by metal pads in a EBeam lithography process. The experimental results presented in this section were achieved during a research stay at the Institute for Solid State Electronics of the Technical University of Vienna, in close collaboration with Matthias Steinmair and Christoph Schöndorfer from the Alois Lugstein’s group.

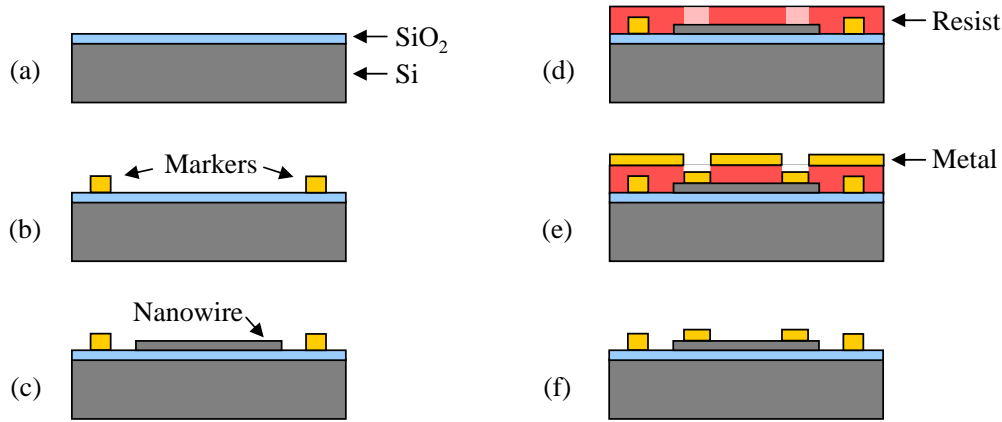
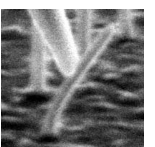


**Figure 3.12:** Process to contact nanowires by EBeam lithography and subsequent lift-off. The process steps are (a) growth of an isolating  $\text{SiO}_2$  layer on a silicon substrate; (b) fabrication of markers by optical or EBeam lithography; (c) dispersing nanowires from a suspension and localizing them using an SEM; (d) spinning resist and exposing the electrode geometry; (e) developing the resist and evaporating the electrode material; (f) lift-off to remove the remaining resist and unwanted metal.

### 3.4.1 Electron beam lithography process

The process flow for contacting nanowires is schematically described in Fig. 3.12, details of the different steps are as follows:

- (a) Growth of  $\text{SiO}_2$  on a Si wafer by dry oxidation for a high breakthrough voltage. The oxide thickness used varies between 80 – 200 nm.
- (b) Deposition of markers by EBeam or optical lithography. These markers are used as reference points when localizing the nanowires before spinning on the resist.
- (c) The nanowires are detached from their original substrate and suspended in ethanol or isopropanol by ultrasonification. They then are dispersed on the sample by applying a droplet of the suspension. Gently blowing the droplet dry with nitrogen yields a more uniform distribution of nanowires than letting the droplet air dry. The nanowires are localized using an SEM, and the pattern of the metal electrodes is designed with respect to their size and orientation.
- (d) A uniform layer of dissolved resist is applied by spinning. The solvent is subsequently evaporated on a hotplate. The sample is then exposed in the SEM by writing the electrode pattern with the EBeam.
- (e) The exposed regions are dissolved in a developer (positive resist). Before metal deposition, a short HF dip removes the native oxide on the nanowire. The metal is then deposited by sputtering or by thermal or EBeam evaporation.



- (f) The lift-off is performed by dissolving the unexposed resist in an ultrasonic bath. The metal deposited besides the electrode structure on the remaining resist is washed away in the solvent.

The details of the process steps for the nanowires contacted in the present work are given in App. B. Figure 3.13 shows a processed sample with a successfully contacted nanowire together with some failures that occur.

The main goal of the electrical investigation is to measure the resistivity of single nanowires in order to estimate their doping concentration. Throughout this work, undoped, during growth doped, as well as post growth doped nanowires are investigated. Only nanowires doped during growth, however, reveal an effective doping concentration, and the following sections concentrate on their results.

### 3.4.2 Investigated characteristics

Figure 3.14 shows a nanowire contacted by four electrodes at different magnifications. To the left the large pads are visible with some scratches; these originate from the needles in the probe station.

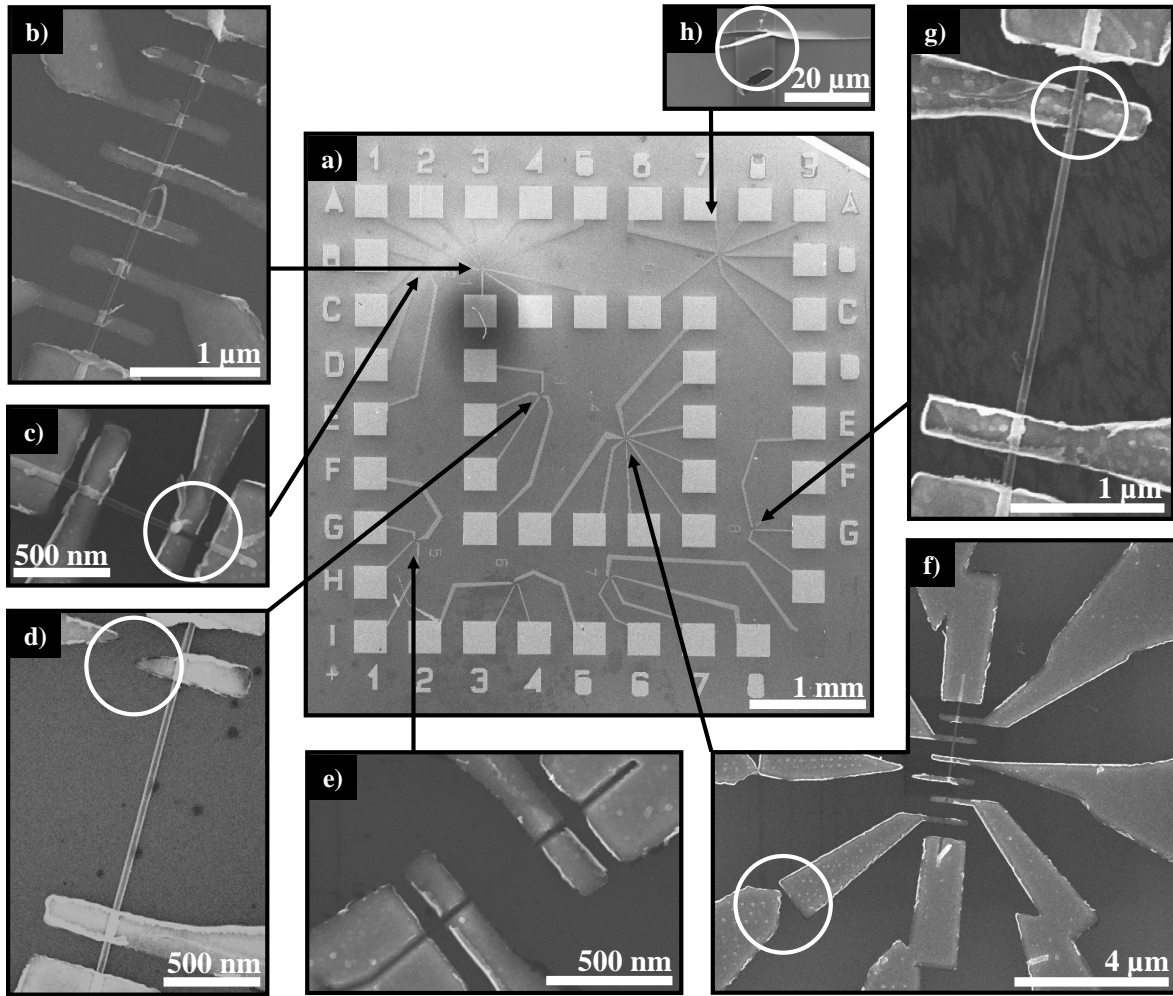
For undoped (and unsuccessfully doped) nanowires, the measured potential drop over the inner electrodes usually is not linear to the current through the nanowire, thus it is not possible to extract their resistance. This is discussed in Sect. 3.4.3.

For the nanowires doped during growth, the measurement of the resistance is possible and, in addition, contact characteristics are extracted. The contacts turn out to be very different at the top of the nanowire, where the catalyst is present during growth, and at the bottom, where it was attached to the substrate. To account for this unsymmetrical behavior, electrode 1 in Fig. 3.7 is defined to be at the bottom of the nanowire, whereas electrode 4 is at the top. The contacts are characterized by measuring the voltage drop between the neighboring electrodes at the end of the nanowire in function of the current passing through the outer contacts. Throughout Figs. 3.16 to 3.19, the current axis represents the current  $I_1$  injected at the bottom electrode, the voltage over the *inner electrodes* is  $U_{El.3} - U_{El.2}$ , the voltage over the *bottom* and the *top contact* are  $U_{El.2} - U_{El.1}$  and  $U_{El.4} - U_{El.3}$ , respectively, and the voltage over the *outer electrodes* is  $U_{El.4} - U_{El.1}$ . The contact characteristics thus also contain the nanowire section between the electrodes in addition to the contact resistance, i.e.  $R_{c1} + R_{12}$  for the bottom and  $R_{c4} + R_{34}$  for the top contact.

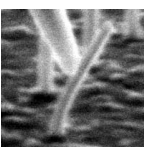
When performing the  $U-I$  measurements, the sweeps are always performed in both directions. All results presented here originate only from curves where no hysteresis is present. Also, the current flowing into electrode 1 is compared to the current flowing out from electrode 4 to be sure that there is no leakage current. Figure 3.15 shows different characteristics observed. In the tables summarizing the results, a linear characteristic is designated by its resistance, a symmetric, non-linear characteristic by  $r_{sym}$ , and a rectifying characteristic with a forward bias from the metal to the semiconductor by  $r_{ms}$  and from the semiconductor to the metal by  $r_{sm}$ .

Often the nanowires do not grow straight, but have a conical shape. If  $A(x)$  designates





**Figure 3.13:** A sample with nanowires contacted by EBeam lithography. a) Overview of the sample. The  $300 \times 300 \mu\text{m}^2$  large pads together with the numbering are written by EBeam lithography beforehand. They serve as reference markers and can be contacted with needles from a prober station or by bonding them to a printed circuit board. b) A nanowire on which 8 electrodes are fabricated successfully. c) A contacted nanowire from which a section on the right is broken off, possibly through electrostatic discharge while handling the sample. d) Electrode that has not correctly been exposed by the lithography system, leading to an open circuit. e) The whole nanowire is torn off during the lift-off step. This occurs often for nanowires that are thicker than the deposited metal. f) The electrodes are written in 2 or more steps, because small structures require small currents for higher precision, as large structures need high currents for faster exposing speed. Drift during exposure leads to open circuits as in the lower left corner. Half the nanowire is torn off, probably during the lift-off step. g) If the deposited metal is not considerably thicker than the nanowire, the metal pad does not wrap well around the nanowire and the top may come off. Electric measurements show that this leads to an open circuit. h) The time optimized process for writing the contact pads leads to overhanging edges at some places. These lead to a discontinuity in the metal electrodes written in the second step, resulting in an open circuit.



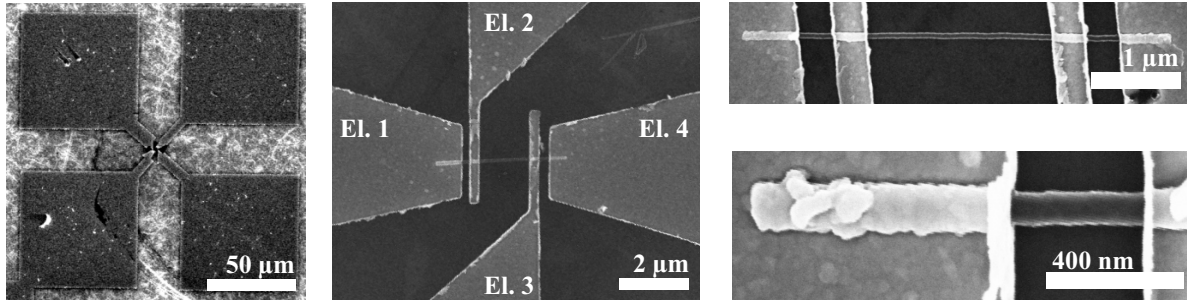


**Figure 3.14:** SEM images of a nanowire contacted by four electrodes. The numbering of the electrodes is defined such that El. 1 is at the root and El. 4 at the top where the metal catalyst was present during growth.

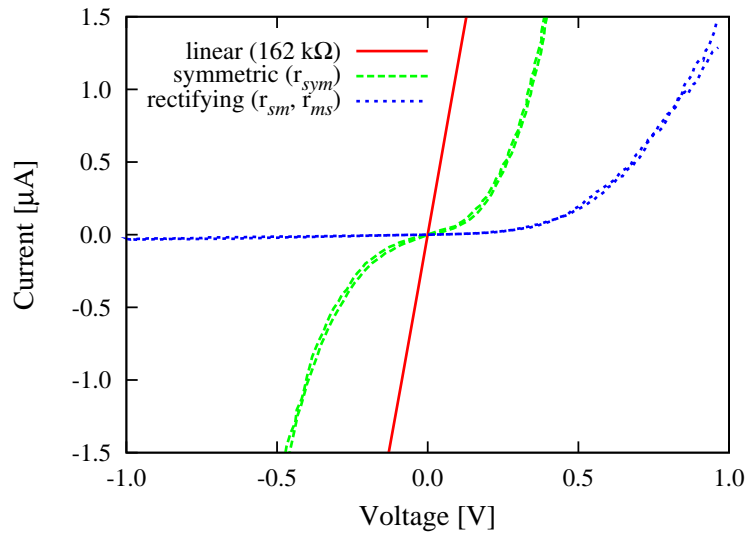


**Figure 3.15:** Classification of voltage-current characteristics. In the following tables summarizing the measurements on nanowires, a linear behavior (red, solid curve) is designed by its resistance, a symmetric behavior (green, dashed curve) by  $r_{sym}$ , and a rectifying behavior (blue, dotted curve) by  $r_{sm}$  and  $r_{ms}$ , where the forward direction is from the semiconductor to the metal and from the metal to the semiconductor, respectively.



the cross-section of the nanowire at position  $x$ , the resistance between the inner electrodes is

$$R_{23} = \rho \int_{x_2}^{x_3} \frac{dx}{A(x)} \quad (3.13)$$

$$= \rho \int_{x_2}^{x_3} \frac{4}{\pi d^2(x)} dx \quad (3.14)$$

$$= \text{some substitution work} \quad (3.15)$$

$$= \frac{4\rho l_{23}}{\pi d_2 d_3} \quad (3.16)$$

where  $d_2$  and  $d_3$  are the nanowires diameters at the electrodes 2 and 3. Thus, the resistivity is calculated from the measured resistance by

$$\rho = \frac{\pi d_2 d_3}{4 l_{23}} R_{23} \quad (3.17)$$

### 3.4.3 Undoped nanowires

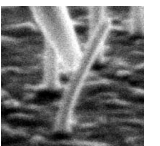
The undoped nanowires are grown by the VLS process with silane as the silicon source. Two samples, grown by Thomas Stelzner at the Institute for Photonic Technologies (IPHT) in Jena (D) and by Alois Lugstein at the Technical University of Vienna (A), are investigated. The growth process of the sample grown by Stelzner is the same as the one for the doped nanowires, described below, but without the dopant source. The nanowires from Lugstein are grown on a heavily  $p$ -doped (B) silicon (111) substrate. After etching away the  $\text{SiO}_2$  in HF, 1 nm of Au is sputtered. At a temperature of 500 °C the nanowires are grown during 60 min at a pressure of 15 mbar (2%  $\text{SiH}_4$  in He, 100 sccm flowrate plus an additional 10 sccm of  $\text{H}_2$ ). The nanowires of both samples show similar electrical characteristics and are thus not treated separately here.

Only 1 out of 15 contacted nanowires revealed a linear  $U$ – $I$  characteristic between the inner electrodes, which is plotted in Fig. 3.16. For all the other nanowires, the voltage drop over the inner electrodes was non-linear and also showed hysteresis.

The contact resistances  $R_{c2}$  and  $R_{c3}$  together with the contact pad capacitances to the substrate ( $\approx 1$  pF), form an  $RC$  circuit that charges and discharges during the voltage sweeps. However, the time constant  $\tau_{RC} = 2\pi RC$  only reaches 0.1 s for contact resistances up to 15 G $\Omega$ . In theory, the contact resistance is expected to be lower ( $<10$  G $\Omega$ ,  $\phi_{Bp} = 0.52$  V for Ti on  $p$ -Si, see Fig. 3.5), and also the contact characteristics measured from Fig. 3.16 show a resistance below 1 G $\Omega$ . The hysteresis did not vanish for long integration times either, so the capacitive influence is not responsible for it.

As discussed in Sect. 3.2.6, the effective cross-section of a nanowire can drastically be reduced by charges present on its surface. During the voltage sweeps, the high electric field present in the nanowire (up to 1 M $\Omega\text{m}^{-1}$ ) may inject hot electrons into the oxide which then get trapped there. The depletion of the nanowire by these charges is especially pronounced for low doping concentrations (see Fig. 3.10), and the nanowire might become depleted completely. The non-linear characteristics and the hysteresis are thus attributed to the surface effects.

From the resistance of 12 G $\Omega$  extracted from the one nanowire with a linear  $U$ – $I$  characteristic, a resistivity of 2.7 k $\Omega\text{cm}$  is calculated (the dimensions of the nanowire are  $l_{23} = 7.1$   $\mu\text{m}$ ,



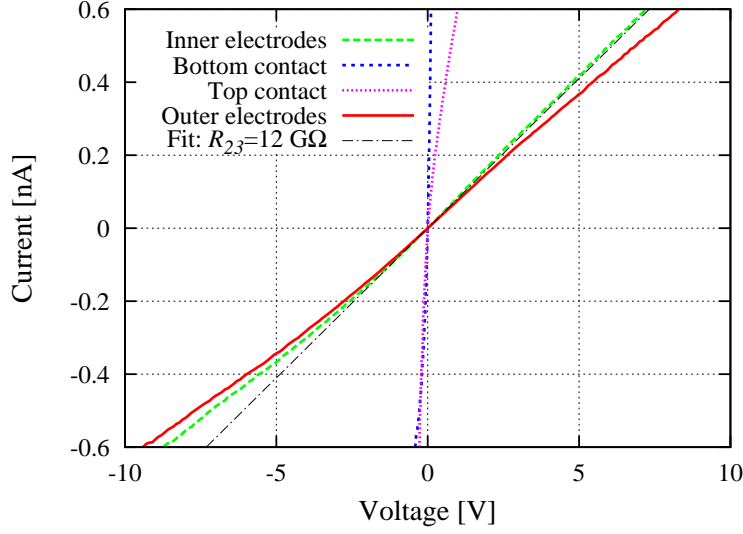


**Figure 3.16:** From 15 successfully contacted undoped nanowires, only the  $U$ - $I$  characteristics of the one shown here has a more or less linear voltage drop over the inner electrodes. This nanowire is from the sample from Lugstein.

$d_2 = 160$  nm and  $d_3 = 130$  nm). Assuming bulk conductivity and neglecting surface effects, this corresponds to a doping concentration of  $\approx 10^{13}$  cm $^{-3}$ . This value, however, can only be taken as an apparent doping concentration, as the influence of the surface is likely to falsify the measurement.

#### 3.4.4 Boron doped nanowires

Boron doped samples are grown by adding diborane ( $B_2H_6$ ) to the vacuum chamber during growth. This consists of sputtering a 2 nm thick layer of Au on an oxide free silicon sample that is etched in 5% HF for 1 min beforehand. The sample is then heated up to 580 °C in UHV and subsequently cooled down to  $\approx 510$  °C for the CVD process. The nanowires are grown for 20 min at 2 mbar, in a mixture of 10 sccm He, 5 sccm silane and 0.05 sccm diborane (2% in He). This results in tapered nanowires with a diameter of  $\approx 80$  nm at the bottom,  $\approx 30$  nm at the top, and a length of 2–4  $\mu$ m. The sample was prepared by Matthias Pietsch under the supervision of Thomas Stelzner at the IPHT.

Figure 3.17 shows the characteristics measured from a boron doped nanowire, and Table 3.2 lists the results from all the successfully contacted nanowires. The average resistivity is 6.5 m $\Omega$ cm, which corresponds to a doping concentration of  $1.3 \times 10^{19}$  cm $^{-3}$ . Interestingly, the contact characteristics are very different at the bottom and at the top: whereas the bottom contact is ohmic, the top contact is strongly rectifying and takes up most of the voltage drop.

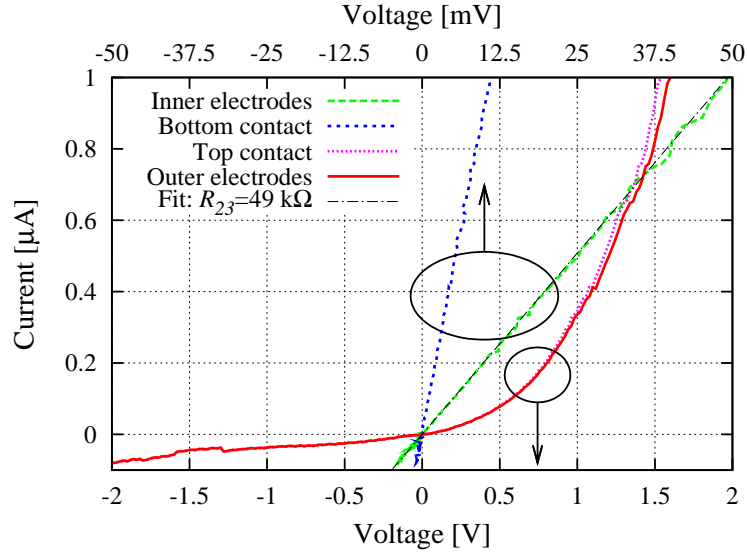
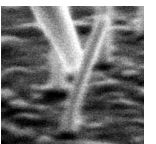


**Figure 3.17:**  $U$ - $I$  curves of the boron doped nanowire number 4. The bottom contact has a linear  $U$ - $I$  curve and a lower resistance than the center section of the nanowire, whereas the top contact is strongly rectifying and takes most of the voltage drop. Note the different voltage scales.

NW	1	2	3	4	5	6	7	8	9
$l_{23}$ [nm]	2160	1100	840	790	442	922	955	613	1930
$d_2$ [nm]	80	71	56	53	59	60	68	42	76
$d_3$ [nm]	47	47	46	40	40	45	57	32	54
$R_{23}$ [k $\Omega$ ]	30	27	16	49	10	52	16	28	49
$R_{c1} + R_{12}$ [k $\Omega$ ]	$r_{sm}$	5.1	14	12	46	6.4	5	7.8	6.9
$R_{c4} + R_{34}$ [k $\Omega$ ]	$r_{sym}$	$r_{sm}$	$r_{sm}$	$r_{sm}$	$r_{sm}$	$r_{sm}$	10	$r_{sm}$	$r_{sm}$
$\rho$ [m $\Omega$ cm]	4.1	6.4	3.8	10	4.2	11.9	5.0	4.9	8.3

**Table 3.2:** Results of the measured resistivities of the boron doped nanowires.



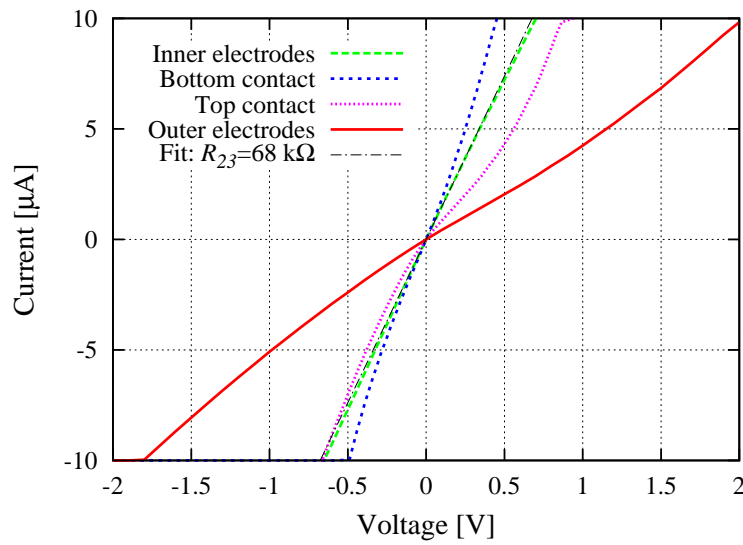
### 3.4.5 Phosphorous doped nanowires

Two samples are prepared with different amounts of phosphine ( $\text{PH}_3$ ) added during the growth process. For both samples, a 2 nm thick layer of Au is sputtered on an oxide free silicon sample that is etched in 5% HF for 1 min beforehand. The samples are then heated up to 580 °C in UHV and subsequently cooled down to  $\approx 505$  °C for the CVD process. At 2 mbar, in a mixture of 10 sccm He, 5 sccm silane and 0.05 sccm (P-sample 1) or 0.2 sccm (P-sample 2) phosphine (2% in He) the nanowires are grown for 20 min. This results in cylindrical nanowires with diameters between 30–60 nm (P-sample 1) and 60–100 nm (P-sample 2) and lengths of 3–4  $\mu\text{m}$  (P-sample 1) and 3–7  $\mu\text{m}$  (P-sample 2). Both samples were prepared by Matthias Pietsch under the supervision of Thomas Stelzner at the IPHT.

The results of P-sample 1 are summarized in Tab. 3.3, and representative  $U$ – $I$  characteristics are shown in Fig. 3.18. The resistivity is measured to be around 3 m $\Omega\text{cm}$ , corresponding to a bulk silicon doping concentration of  $2 \times 10^{19} \text{ cm}^{-3}$ , and the contacts show both linear and non-linear, symmetrical characteristics.

The resistivity measured in P-sample 2 is higher than in P-sample 1, on average 12 m $\Omega\text{cm}$ , corresponding to a bulk doping concentration of  $3 \times 10^{18} \text{ cm}^{-3}$ . The contacts, as for boron doped nanowires, show a linear behavior at the bottom and a rectifying behavior at the top. Table 3.4 shows the results of the successfully contacted nanowires, and Fig. 3.19 an example of the  $U$ – $I$  characteristics.

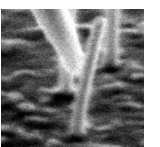
The nanowires of P-sample 2 are long enough to be contacted by more than 4 electrodes. Structures with 8 contacts were thus prepared in order to investigate the uniformity of the doping concentration along the nanowire, which is shown in Fig. 3.20. Figure 3.21 shows the resistivity measured along its axis, changing by a factor of 1.4 from section 2–3 to section 7–8. This change in resistivity is also observed for the other nanowires contacted by 8 electrodes, 5 in total; the factors varied between 1.4 and 2.8. The contact characteristics are shown in Fig. 3.22.



**Figure 3.18:**  $U$ - $I$  curves of nanowire number 2 from  $P$ -sample 1.

NW	1	2	3	4
$l_{23}$ [nm]	2520	1950	1950	2550
$d_2$ [nm]	39	39	$\approx 60$	66
$d_3$ [nm]	32	37	$\approx 60$	58
$R_{23}$ [k $\Omega$ ]	62	68	14	34
$R_{c1} + R_{12}$ [k $\Omega$ ]	$r_{sym}$	$r_{sym}$	7.1	17
$R_{c4} + R_{34}$ [k $\Omega$ ]	$r_{sym}$	51	8.4	29
$\rho$ [m $\Omega$ cm]	2.4	3.9	2.1	4.0

**Table 3.3:** Results of the measured resistivities of  $P$ -sample 1.



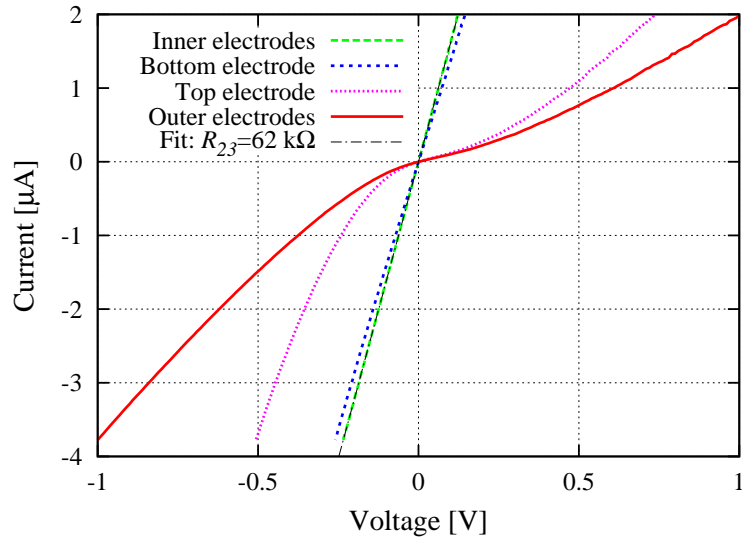


**Figure 3.19:**  $U$ - $I$  curves of nanowire number 1 from  $P$ -sample 2.

NW	1	2	3	4	5	6
$l_{23}$ [nm]	1310	1060	2340	2880	3190	2120
$d_2$ [nm]	58	60	58	90	98	64
$d_3$ [nm]	58	60	58	93	102	63
$R_{23}$ [k $\Omega$ ]	62	88	162	24	19	47
$R_{c1} + R_{12}$ [k $\Omega$ ]	70	60	64	7.1	5.0	$r_{sym}$
$R_{c4} + R_{34}$ [k $\Omega$ ]	$r_{ms}$	$r_{ms}$	$r_{ms}$	$r_{ms}$	$r_{ms}$	$r_{ms}$
$\rho$ [m $\Omega$ cm]	13	23	18	5.5	4.3	11

**Table 3.4:** Results of the measured resistivities of  $P$ -sample 2.

### 3.4.6 Discussion

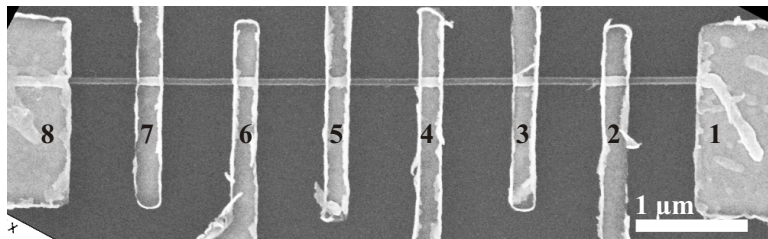
The measurement on undoped nanowires were already discussed while presenting their results in Sect. 3.4.3, here the results of the doped nanowires are discussed.

Both the boron and the phosphorous doped nanowires reveal doping concentrations in the order of  $10^{19} \text{ cm}^{-3}$ . At this level, the surface charges, as they were measured in the literature<sup>48,87</sup>, are effectively screened and do not have a major influence on the effective nanowire cross-section (Fig. 3.10). The values for the doping concentration measured are thus in a reliable order of magnitude.

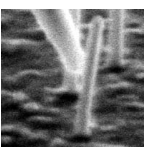
Doping of the same order of magnitude with boron and phosphorous was also achieved by Cui *et al*<sup>18,20</sup> and Wang *et al*<sup>107</sup>, while nanowires with slightly lower concentrations are grown by Kimukin *et al*<sup>48</sup> and Lew *et al*<sup>56</sup> and higher concentrations are reported by Mohny *et al*<sup>69</sup>.

The contacts, however, present very different characteristics at the bottom and at the top. Both nanowires with the Au droplets still on top and etched away with aqua regia are inspected, but the top contact characteristic does not depend on the presence of the Au, indicating that the current flows mainly through the nanowires' sidewall and not through the Au cap or the top facet. A variation in the doping concentration along the nanowire axis does change the contact characteristics, but the factor of 2 measured in the experiment with eight electrodes can only partly explain the huge difference in contact resistances, which varies over 3 orders of magnitude. Figure 3.22 shows the contact characteristics for the eight different electrodes. Only the bottom contact is linear over the entire current range. As can be seen in Fig. 3.20, the nanowire has a kink about 800 nm above its bottom end. The kink probably originates from a change in growth conditions in the initial growth phase, e.g. a change in temperature or gas concentration can change the crystallographic growth direction<sup>63</sup>. Possibly, the electric contact to the section before the kink is better due to a different morphology. Whatever the reason for the low contact resistance at the bottom is, its detection is important because it can be explored when incorporating the nanowire into a device.

The average resistivity measured for P-sample 2 is a factor of 4 higher than that for P-sample 1. This is true even though a factor of 4 more phosphine is present during growth of P-sample 2 than for P-sample 1. One expects that more dopants are present in nanowires of P-sample 2, but the less pure growth environment can also induce more defects in the crystal



**Figure 3.20:** A nanowire from P-sample 2 contacted by 8 electrodes. The nanowire bottom is located at electrode 1.



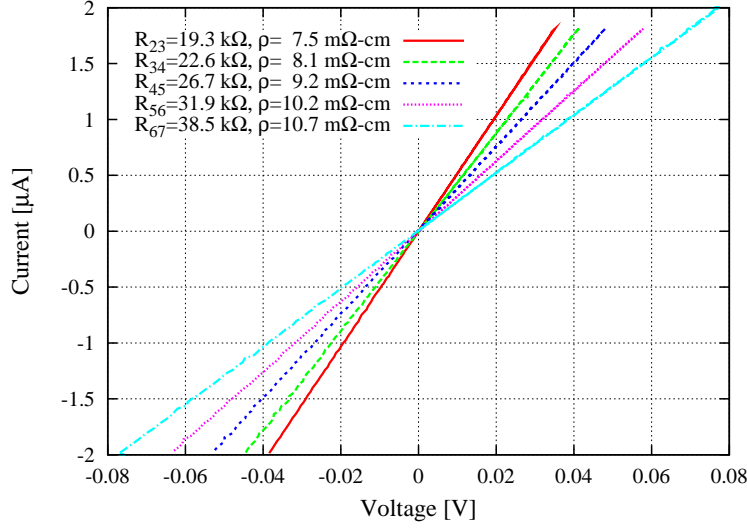


**Figure 3.21:** The resistivity measured at different sections along the growth axis of a phosphorous doped nanowire.

structure. The higher resistivity is thus attributed to a lower mobility of the charge carriers, due to a higher scattering center density. Alternatively, reproducibility of the growth process might also be an issue.

The change in resistivity along the growth axis is measured to be about a factor of 2 for P-sample 2, where the higher resistivity is measured at the top of the nanowire. Such a change in the doping concentration is not reported in literature. With the exception of a very recent publication by Imamura *et al*<sup>44</sup>, discussed below, the concentration is always assumed to be uniform. A possible reason for the concentration gradient could be that the dopants are not absorbed by the catalyst directly, but at the substrate and the nanowire sidewall. They then subsequently have to diffuse to the catalyst before they can get incorporated into the nanowire. As the nanowire grows, the silicon surface area within a given diffusion distance from the catalyst decreases because the substrate is further away. This means that fewer dopants reach the catalyst, leading to a higher resistivity. During growth, the sample is maintained at the desired temperature by heating the sample holder. Another reason for the variation of the doping concentration along the nanowire axis could thus be a temperature difference at the nanowire root and the nanowire top, as the top might be cooler due to thermal radiation. A difference in temperature changes the composition of the Au-Si droplet, leading to a different dopant incorporation efficiency. Both reasons, however, are highly speculative, as little is known about the incorporation of the dopants in the VLS process.

A very recent publication by Imamura *et al* reports the conformal growth of a highly *p*-doped layer during a VLS process with B as the dopant.<sup>44</sup> Their growth process, however, differs from the one presented here in that the silicon precursor is Si<sub>2</sub>H<sub>6</sub> instead of SiH<sub>4</sub> and the doping is B instead of P. The electrically active B concentration is studied by analyzing Fano resonance in Raman spectra. They do not say how uniform the nanowires are in diameter;



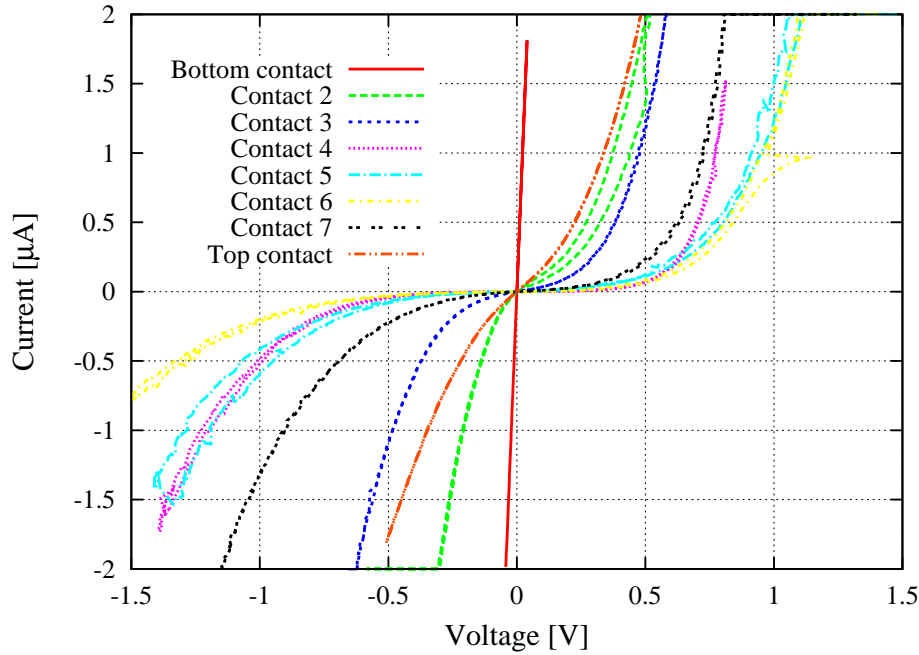


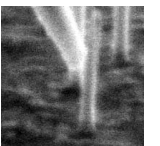
**Figure 3.22:** Contact characteristics changing along the growth axis of a phosphorous doped nanowire. The bottom and top contact characteristics include the resistance of the nanowire section between the electrodes, whereas the other  $U-I$  curves originate solely from the contacts, as the potential of the silicon underneath the contact can be probed by an neighboring electrode that is not in the current path.

however, the growth of an extra layer is likely to be observable by SEM imaging by measuring a thicker end at the bottom than at the top. This is not the case for our examined P-sample 2, whose nanowires are uniform in diameter.

For undoped nanowires, Park *et al* report for a VLS process with  $\text{Si}_2\text{H}_6$  as precursor, an electrically uniform behavior of very long (millimeter scale) nanowires, tested by fabricating several FETs along the nanowire axis.<sup>81</sup>

### 3.5 Location of junctions by electron beam induced current imaging

By adding carrier gases containing a dopant in the VLS process, nanowires can be doped during growth. Dopant incorporation is reported for diborane<sup>18</sup>, trimethylboron<sup>56</sup>, phosphine<sup>107</sup> and arsenic<sup>98</sup>. By changing the dopant source during growth,  $p-n$  junctions can be made along the axis of the nanowire.<sup>33,98</sup> However little is known about the dopant incorporation mechanism. As reported in the previous section, the doping profile of nanowires doped during growth might not be uniform along the nanowire axis. Also, recent experimental results evidence the growth of a highly doped shell around the nanowire while doping during VLS growth.<sup>44</sup>



As an alternative, reproducible and successful doping of nanowires can be achieved via ion implantation. This technique is a standard doping technique in top-down semiconductor manufacturing and offers the advantage of providing precise control over the total dose of dopants and depth profile. Most importantly, it works well also for high doping levels of the order of  $10^{20}$ – $10^{21}$  cm<sup>-3</sup>. It has been demonstrated that GaAs can be *p*-type doped using Zn ions<sup>94</sup>, and Si by the the respective use of B and P ions<sup>16</sup>. However, the demonstration of functional devices on the basis of ion implanted nanowires is still lacking.

This section presents the characterization of ion implanted silicon nanowires. By varying the fluencies, acceleration voltages, and ions in subsequent implantation steps, uniform *n* and *p* type doping, as well as *p-n* profiles are achieved along the nanowire axis.

The nanowires under investigation have diameters of 150–350 nm and a length between 250 and 500 nm. EBeam lithography works well to contact nanostructures when the requirement on the alignment precision is in the order of a few 100 nm or above. Below 200 nm the yield drops drastically, and in addition the relatively wide nanowires require thick electrodes, which puts constraints on the minimal lateral feature size. A conductive tip mounted on a nanomanipulator setup inside an SEM is thus being used to directly contact the nanowires that stand as grown on the substrate, which serves as the second contact. EBIC imaging reveals junctions at the tip-nanowire interface and within the nanowire, and current-voltage characteristics show the rectifying behavior of the *p-n* junctions.

This work has been carried out in close collaboration with Jan Bauer, Pratyush Das-Ka-nungo, Vladimir Sivakov and Silke Christiansen from the Max Plank Institute of Microstruc-ture Physics in Halle (D) and Carsten Ronning from the Friedrich-Schiller-Universität Jena (D).

### 3.5.1 Principle of electron beam induced current imaging

EBIC imaging is used in industry to reveal junctions or defects in semiconductor devices.<sup>53</sup> The technique relies on the separation of charge carriers by the electric field present in depleted regions. Figure 3.23(a) schematically shows its principle: The electron beam of an SEM induces electron-hole pairs in the semiconductor. In absence of an electric field, these eventually recombine. But if the induced charge carriers diffuse to the depleted region of a junction, the electric field separates them, which leads to a net current (positive in the direction indicated). Excited carriers can also recombine at the device surface before reaching the depletion region, these do not contribute to the signal. The magnitude of the induced current at each pixel is represented by different gray levels in the EBIC image. The junction may arise from a Schottky contact at the metal-semiconductor interface or from a *p-n* doping profile within the semiconductor.

### 3.5.2 Scanning photocurrent imaging

A similar technique is already used by some groups to reveal junctions in semiconducting nanowires. Instead of a electron beam, they use light to induce electron-hole pairs. A laser source is focused on the diffraction limited spot size and is scanned over the sample. Ahn *et al* have used this technique to reveal Schottky contacts at nickel contact pads on silicon

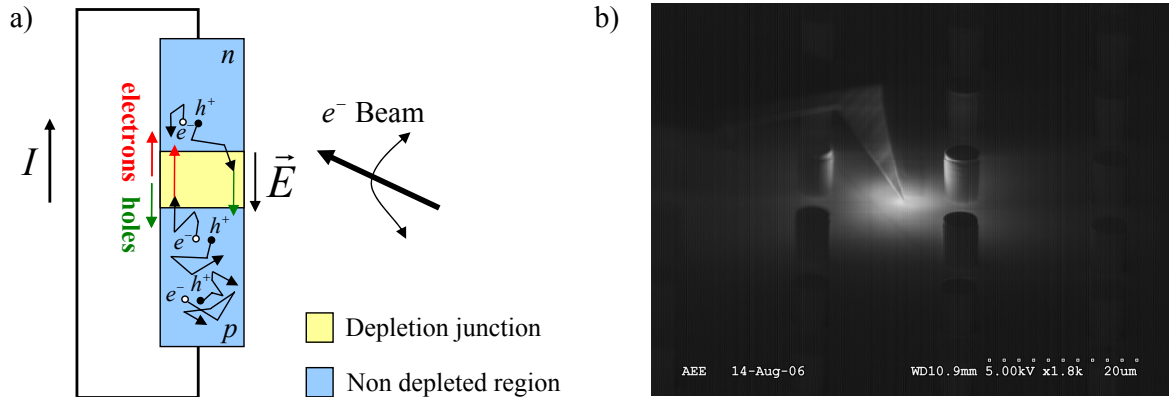


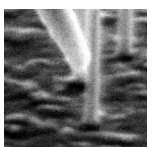
**Figure 3.23:** (a) Principle of EBIC imaging: the contrast of an image is based on the magnitude of the current induced by the electron beam scanning over the sample. (b) EBIC image of a silicon AFM tip in contact with a GaAs substrate surrounded by GaAs pillars. The junction is located beneath the AFM tip, but a ghost signal is also present at the edge of neighboring pillars. This signal originates from secondary electrons kicked out of the edges by the electron beam that diffuse through space to the junction, where they are collected.

nanowires<sup>2</sup>, and Freitag *et al* to image the Schottky contacts to semiconducting carbon nanotubes<sup>28</sup>. Gu *et al* have gone a step further by analyzing the spatial profiles of the local photoconductivity maps.<sup>32</sup> From the slope of the current versus distance in a logarithmic plot, the mobility $\times$ lifetime product ( $\mu\tau$ ) can be extracted. With units of  $\text{cm}^2\text{V}^{-1}$ , this is the average length a carrier moves per unit field, and is therefore an important figure of merit for charge collecting devices.  $\mu\tau$  directly influences the quantum yield and the conversion efficiency in photodetectors and solar cells, respectively.

### 3.5.3 Doping of nanowires by ion implantation

The results on three different samples are presented, the first purely *n*-doped (sample *n*), the second *n*-doped at the top and *p*-doped at the bottom (sample *np*) and the third *p*-doped at the top and *n*-doped at the bottom (sample *pn*). Figure 3.24 shows the different doping profile schematically.

Nanowires are grown by EBE VLS, where the gaseous silicon source is provided from atomic silicon evaporated by electron beam irradiation. For the VLS growth, 1.2 nm (sample *np*) and 2.4 nm (sample *pn* & sample *n*) Au is sputtered on a blank silicon (111) sample. The substrates are chosen to match the doping of the bottom of the nanowires, that is *n* type (P, 1–20  $\Omega\text{cm}$ ) for sample *pn* and sample *n*, and *p* type (B, 10  $\Omega\text{cm}$ ) for sample *np*. The native silicon dioxide layer is removed before sputtering the Au layer by etching in 40% HF solution for 30 s followed by a 2% HF rinse for 3 min. The growth takes place at 625  $^\circ\text{C}$  (sample *np*) and 675  $^\circ\text{C}$  (sample *pn* & sample *n*) at a pressure of  $10^{-6} - 10^{-7}$  mbar during 1 h. More details can be found in a publication by Vladimir Sivakov<sup>90</sup> who grew the samples. The resulting nanowires are 250–500 nm long and 150–400 nm wide.



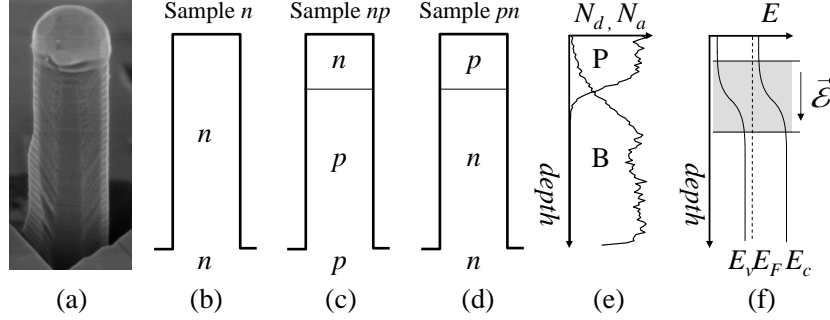


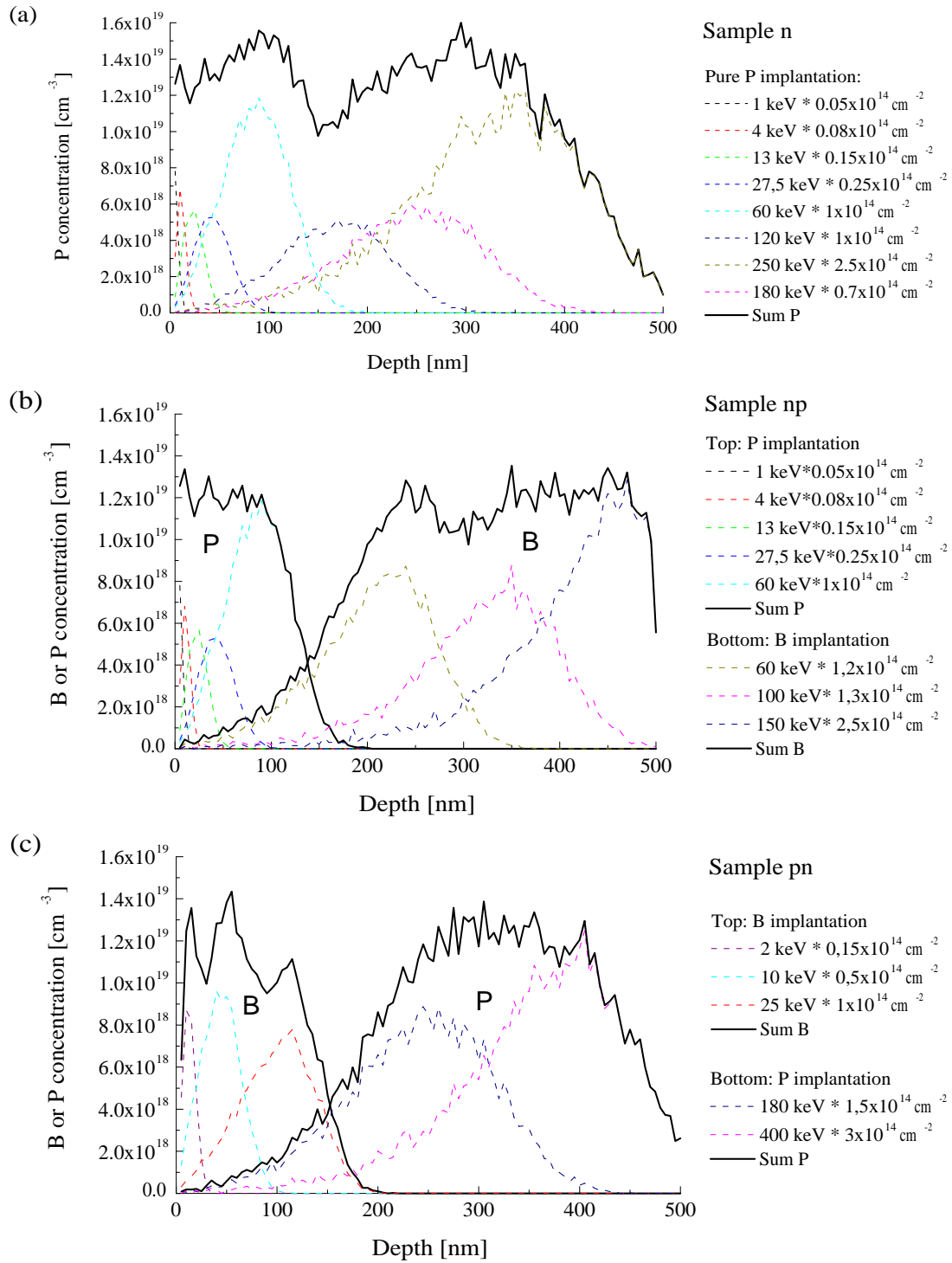
**Figure 3.24:** (a) SEM image of a silicon nanowire with the gold catalyst still on top. (b)-(d) Doping schema for the different samples. (e) Simulated doping profile of sample np. (f) Corresponding band structure, the depletion region is gray shaded and the direction of the electric field indicated.

A hopping conductivity across gold agglomerates on the nanowire sidewalls was measured on similarly grown nanowires<sup>4</sup>, therefore special care is taken to remove the gold droplets atop the nanowires and on the nanowire sidewalls. So, gold agglomeration to the bigger clusters on the surfaces is enhanced by annealing the samples at 800 °C for 15 min in air, and the silicon oxide is subsequently removed by a 2% HF dip for 2 min. Immediately after the HF dip, the sample is immersed in aqua regia in order to etch away the gold. SEM investigations show that the large Au droplets atop the nanowire and smaller droplets on the nanowire sidewalls are entirely removed after this treatment. Transmission electron microscopy studies, however, reveal in rare cases that very small Au agglomerates are still presented on the nanowires.<sup>15</sup>

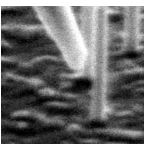
Ion implantations of  $^{11}\text{B}^+$  (as acceptor) and  $^{31}\text{P}^+$  (as donor) are performed at room temperature with ion energies varying from 1 to 400 keV and fluencies between  $0.05\text{--}3 \times 10^{14} \text{ cm}^{-2}$ . The sample surface is aligned almost perpendicular with respect to the ion beam; an angle of a few degrees is used in order to avoid channeling effects into the  $\langle 111 \rangle$  axis. The implantation profiles are calculated with the program package TRIM<sup>118</sup> and are plotted in Fig. 3.25 as a function of depth. The maximum depth matches the length of the nanowires and the peak concentration of each dopant reaches  $1\text{--}1.5 \times 10^{19} \text{ cm}^{-3}$ . All three samples are annealed directly after implantation at 850 °C for 15 min in order to remove the implantation damage.<sup>65</sup> The pressure is kept below  $1.5 \times 10^{-6} \text{ mbar}$  during annealing, avoiding oxidation of the Si substrate and nanowires. The whole ion implantation process is done by Carsten Ronning.

### 3.5.4 Experimental

Different tips are tested for their suitability to contact nanowires in the SEM. These include: highly doped, commercially available silicon AFM tips, commercially available AFM tips with a doped diamond coating, AFM tips sputtered with a layer of some 10 nm of Pt or Ti/Au, and PtIr scanning tunneling microscope (STM) tips etched from a PtIr wire. It is easiest to get an electrical contact with the PtIr tip, probably because (i) it is a soft material, adapting to the shape of the contact, resulting in a larger contact area, (ii) isolating electron beam induced contamination deposition can be scratched off the tip and (iii) the whole tip material



**Figure 3.25:** Simulated doping profiles of the ion implanted nanowires.



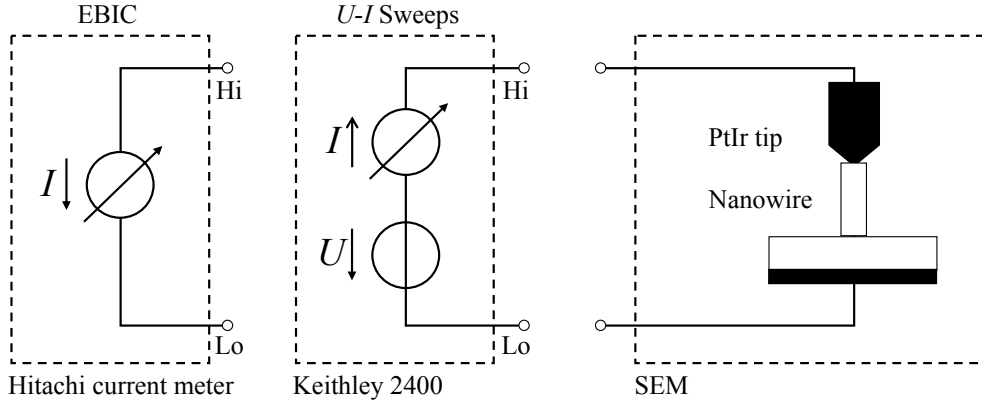


**Figure 3.26:** Electrical diagram for the EBIC imaging and  $U$ – $I$  sweeps of the ion implanted nanowires.

is PtIr, whereas coated AFM tips rely on a thin conductive layer that is scratched away after a few attempts of contacting a nanowire. A disadvantage of using PtIr tips is that due to their softness they become blunt as soon they are pushed slightly into the substrate, and because of the high stiffness of the PtIr wire (in contrast to the soft cantilever beams of the AFM tips), the nanowires have to be contacted carefully in order not to break them off.

The results presented here are all achieved with PtIr STM tips. The etching is based on an electrochemical process. A salt melt of 15 g NaOH (6 parts)/17.6 g  $\text{NaNO}_3$  (7 parts) is heated up to 320 °C, into which 2 mm of the PtIr wire (90% Pt, 10% Ir,  $\varnothing$  0.25 mm) is immersed. An AC voltage of 10–15  $V_{pp}$ , superposed to a DC voltage of 8–10 V with the negative pole at the tip, is applied between the wire and the salt melt. The wire is then periodically immersed deeper into the salt melt, by  $\approx$  3 mm at a period of 1 Hz, until an electrical arc is visible on retraction. At this point, the original 2 mm of the wire, that were immersed at the beginning, are completely etched away, and resulting in a tip with a radius of 100–500 nm at its apex. The tip is cleaned by immersing it in aqua regia and holding it in an ethanol flame for a few seconds. An alternative etch process was published by Libiouille *et al.*<sup>59</sup>

The nanomanipulation setup used to get the tip into contact with the nanowires is the same as used for the mechanical experiments, presented in Sect. 4.3.1. A Keithley 2400 SMU is used to perform the electrical measurements. The voltage is applied to the PtIr tip (positive pole) and the sample is connected to the low impedance common, the circuit being separated from ground (microscope chamber). For the EBIC imaging, the PtIr tip is connected to the input of the current meter of the SEM (ESED, environmental secondary electron detector). The electric schematic is sketched in Fig. 3.26 (note the different current polarities between the EBIC and the  $U$ – $I$  sweep setups).

### 3.5.5 Results

For all three samples, at least one EBIC image and a  $U$ – $I$  sweep could be performed. A mechanical drift in the setup often causes failure of the nanowires because of their high stiffness

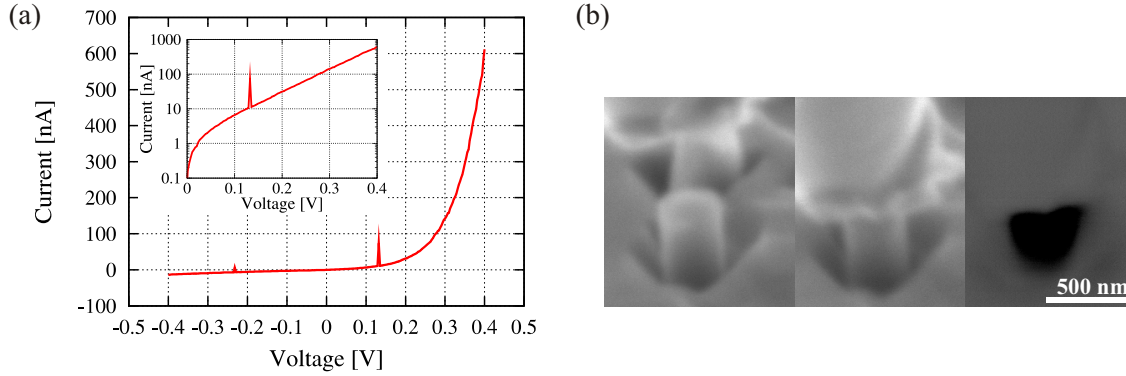


**Figure 3.27:** (a) Current–voltage characteristic of a PtIr tip in contact with a uniformly *n*-doped nanowire. The voltage is applied at the tip with respect to the substrate. (b) Left: SE image of the nanowire under investigation; Center: SE image of the tip in contact with the nanowire; Right: EBIC image of the Schottky contact at the tip–nanowire interface. In the SEM images the nanowire is at an angle of  $60^\circ$  with respect to the electron beam.

(low length/diameter ratio) and the high stiffness of the PtIr tip. Whereas the EBIC images are reproducible, the  $U$ – $I$  sweeps are not, which is discussed in the next section. Here, the most convincing results are presented, but one must keep in mind that a strong variation is present in the voltage–current characteristics.

A positive current appears black in the EBIC image, whereas negative currents show up white. Because the EBIC current is the reverse current of a junction (drift current), we expect a positive current for the Schottky contact between the PtIr tip and the nanowire for sample *n*, and a negative and positive current for the *p*–*n* junctions in samples *np* and *pn*, respectively. For the purpose of orientation the EBIC image is always shown next to a secondary electron (SE) image from the same location at the same magnification.

### Sample *n*

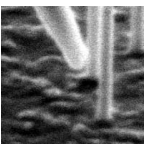
Figure 3.27 shows a  $U$ – $I$  curve and an EBIC image of the same nanowire. As expected, the EBIC signal is located at the tip–nanowire contact and appears black, indicating that electrons drift to the nanowire and holes to the tip. The  $U$ – $I$  characteristic is rectifying, with the forward direction from the tip to the nanowire. The current follows the equation

$$I = I_0 \left( e^{\frac{qV}{\eta kT}} - 1 \right), \quad (3.18)$$

and from the logarithmic plot in the inset one can extract a quality factor of  $\eta = 2.6$  and a saturation current of  $I_0 = 1.5$  nA.

### Sample *np*

The EBIC signal is shown in Fig. 3.28(a). It appears white as expected, representing a negative current. The  $U$ – $I$  characteristic, shown in Fig. 3.29(a) is rectifying, but the logarithmic plot





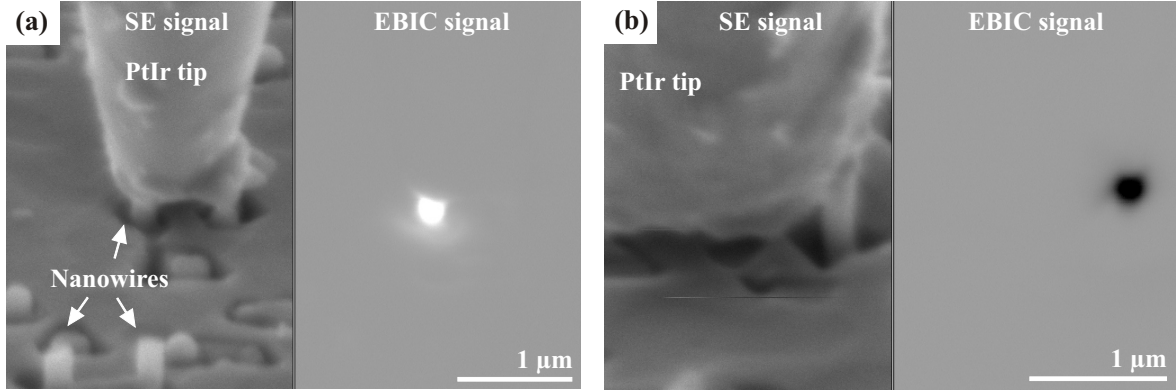


**Figure 3.28:** SE and EBIC images of (a)  $n$ - $p$  nanowires (sample  $np$ ) and (b)  $p$ - $n$  nanowires (sample  $pn$ ). The nanowires are standing at an angle of  $60^\circ$  with respect to the electron beam.

does not reveal a linear part, so it is neither possible to extract a quality factor nor a saturation current.

### Sample $pn$

In contrast to the nanowire of sample  $np$ , the EBIC image of sample  $pn$  reveals a positive current (Fig. 3.28(b)). The  $U$ - $I$  characteristics (Fig. 3.29(b)) show a rectifying behavior, but not as pronounced as the  $p$ - $n$  junction in sample  $np$  or the Schottky contact on sample  $n$ . Also, the magnitude of the current strongly depends on the tip-nanowire contact. Most current is present in the first sweep (no image available, red solid curve), it decreases drastically when the contact area is small (center image in the inset, green dashed curve), and increases again when the contact area is larger (right inset, blue dotted curve).

### Undoped nanowires

During the ion implantation process, half of the sample area is shielded from the ion beam, such that the nanowires underneath remain undoped. EBIC images of those nanowires show a faint EBIC signal between the nanowire and the substrate (not shown here), as it has been observed on undoped nanowires already.<sup>4</sup> The current through an undoped nanowire in the  $I$ - $V$  sweeps is 2–3 orders of magnitudes lower than through a doped nanowire, demonstrating that the nanowires conductance increases upon ion beam doping.

### 3.5.6 Discussion

The EBIC images all reveal the expected junctions and are thus proof that the nanowires are effectively doped. This observation is also supported by the measured  $U$ - $I$  curves.

For the  $p$ - $n$ -doped nanowires, it is not possible to tell exactly where the junction is located. However, it can be excluded that the EBIC signal originates from a Schottky contact at the tip-nanowire interface. Such a Schottky contact would reveal an inverse contrast, black for



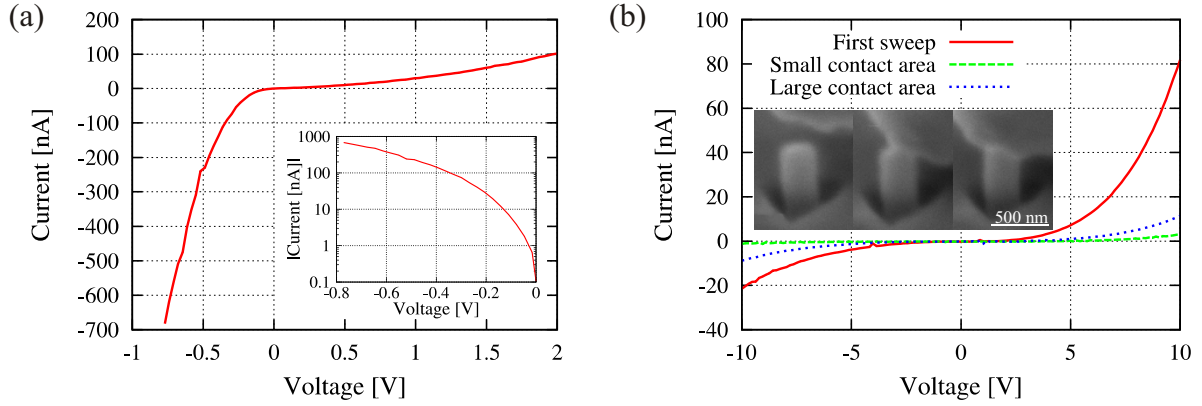


**Figure 3.29:** Current–voltage characteristics measured on  $p$ - $n$ -doped nanowires. The voltage is defined to be positive at the tip with respect to the substrate. (a) Nanowire from sample  $np$ , the same as from which the EBIC image is taken in Fig. 3.28(a). (b) A nanowire from sample  $pn$ , shown in the left inset. The red solid curve shows the first recorded sweep, the green dashed curve the second sweep with only a small contact area between tip and nanowire (center inset) and the blue dotted curve with a larger contact area (right inset).

the tip- $n$ -doped top of the nanowire from sample  $np$  and white for the tip- $p$ -doped top of the nanowire from sample  $pn$ .

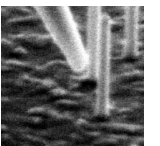
The  $U$ – $I$  characteristics of the Schottky contact on the nanowire of sample  $n$  reveals the expected rectifying behavior, and its steepest slope shows that the series resistance is smaller than 60 k $\Omega$ . This resistance, however, is not necessarily linked to the nanowire. The spreading resistance through the substrate is in that order of magnitude, too. For a top contact area with diameter  $d$  (diameter of the nanowire), a resistivity  $\rho$ , a substrate thickness  $h$  and a bottom contact area  $\gg h^2$ , the spreading resistance  $R_{sp}$  is

$$R_{sp} = \frac{\rho}{\pi d} \tan^{-1} \left( \frac{4h}{d} \right) . \quad (3.19)$$

With a substrate thickness of 0.58 cm, a substrate resistivity of 1–20  $\Omega$ cm, and a nanowire diameter of 380 nm, this yields a spreading resistance of 13–260 k $\Omega$ . The two point measurement thus does not allow the resistivity of the nanowire to be calculated.

The quality factor, however, is ideally  $\eta = 1$  for a Schottky diode. Tunneling through the barrier increases  $\eta$ <sup>96</sup>, and the measured quality factor of 2.6 thus indicates qualitatively that the doping concentration has at least reached a value of  $10^{18}$  cm<sup>-3</sup>. For the targeted doping concentration of  $1.3 \times 10^{19}$  cm<sup>-3</sup>, the thermionic field emission is the dominant process (see Fig. 3.4). For doping concentrations above  $10^{20}$  cm<sup>-3</sup>, field emission would be the dominant process and one would expect a linear  $U$ – $I$  characteristic (ohmic contact).

The current of the nanowire of sample  $np$  becomes linear with respect to the voltage below –0.5 V, the series resistance extracted therefrom is 625 k $\Omega$ . With a nanowire diameter of 190 nm and a substrate doping concentration of 10  $\Omega$ cm, the spreading resistance through the substrate is about 300 k $\Omega$ cm. It is thus not possible to extract an accurate series resistance of



the nanowire. Neither is it possible for the nanowire of sample  $pn$ , because the contact area limits the current.

Even if a quantitative extraction of the doping concentration is not possible by this technique, it should be pointed out that it is much faster to perform and less costly than EBeam lithography. A fast verification of doping is especially important for the efficient development of new processes.

## Chapter 4

# Mechanical characterization

### Abstract

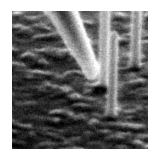
*In situ* mechanical experiments are performed to measure bending strength, tensile strength and Young's modulus of bottom-up fabricated silicon and zinc oxide nanowires. The experimental methods employed, based on bending and tensile tests, are outlined and discussed. Silicon nanowires exhibit a bending strength of  $(6.3 \pm 1.8)\%$  (average  $\pm 1$  standard deviation), which is much closer to the theoretical limit of 16% than that of micro and millimeter sized samples. It is shown that they are ripples at the nanowires' surface that might be responsible for a stress concentration leading to failure. For zinc oxide nanowires, the fracture strain of  $(7.7 \pm 0.8)\%$  measured in the bending test reveals a strength about twice as high as measured in the tensile test. From the tensile experiments Young's modulus is measured to be within 35% of that of bulk ZnO, contrary to the lower values found in literature.

### 4.1 Motivation

There is a technological as well as a scientific motivation for studying mechanical properties of nanowires. The technological interest is to know if the nanowires can withstand certain process steps like spinning resist or spin-on-doping over freestanding nanowires, or ultrasonification in a lift-off process. The scientific interest is to understand how parameters like fracture strength or Young's modulus scale with the specimens size, and to see if the laws established in the macro- and micro world are still valid down to the nanometer range. The following two subsections introduce this matter.

#### 4.1.1 Fracture mechanics

Macroscopic mechanical properties are dominated by a statistical distribution of defects with various characteristic length scales: the size and distribution of flaws in brittle fracture (100  $\mu\text{m}$ ), size and interdistance of persistent glide bands in metal fatigue (10  $\mu\text{m}$ ), sub-grain boundary spacing in creep (1  $\mu\text{m}$ ), and dislocation interdistance in metal plasticity (100 nm).



At the macroscopic scale, the Weibull statistic governs the strength of brittle materials.<sup>109</sup> It is based on the fact that in small samples, the probability of encountering a large defect that leads to failure, is smaller than in larger samples, which makes small samples statistically stronger (Fig. 4.1). As dimensions are further scaled down below the characteristic length, material properties become controlled by geometrical constraints. This includes device dimensions (physical size effect) as well as microstructure length scales like grain size (micro-/nanoscale size effect). Whereas microstructure size effects have been used for decades for hardening metals, physical size effects have been studied only recently, fueled by the ongoing miniaturization of micro- and nanomechanical systems.

Physical size effects appear particularly if the characteristic length scale is comparable to the device dimensions. In this case, the mechanical behavior of the material is governed by the interaction of a few defects, meaning that the behavior can neither be described by the statistical treatment of a large number of defects nor by their absence. The understanding of these size effects is a prerequisite for efficient material processing and high reliability of nanodevices like nanoelectromechanical systems or nanowires for sensor and electronic applications.

Namazue *et al.* have evaluated the size effect on fracture strength and Young's modulus of single crystal silicon by nanoscale bending tests using an AFM.<sup>72</sup> They have fabricated nanometer scale silicon beams on a silicon on insulator (SOI) wafer by means of field-enhanced anodisation using AFM and anisotropic wet etching. Micro- and millimeter scale beams were fabricated by conventional photolithography. All fabricated beams were along the  $\langle 110 \rangle$  direction, the smallest one being 200–370 nm wide and 255 nm thick and the largest one 1–1.8 mm wide and 520  $\mu\text{m}$  thick.

The Young's modulus did not change from the nano- to the millimeter range. The bending strength and the relative scatter in bending strength, however, were strongly influenced by the specimen size. Figure 4.1 shows Weibull plots of the bending strength for different beam widths. The plotted cumulative probability is a statistical quantity based on a large number of experiments and represents the probability of failure of the specimen at a certain stress. The plot shows that the bending strength, defined as the stress at the fracture probability of 63%, of a 200 nm wide beam (A) is 2.3–4.7 times larger than that of micrometer scale beams (D & E) and 38 times larger than that of a 1 mm wide beam (F). It can also be seen that the relative scatter in strength is reduced with the size of the beams.

Griffith's theory on fracture of brittle material predicts the fracture stress  $\sigma_f$  to be dependent on the largest crack present in the sample.<sup>30</sup> The fracture strength is roughly calculated as (see Sect. 4.5.1)

$$\sigma_f = \sqrt{\frac{2\gamma E}{\pi a}} \quad (4.1)$$

where  $\gamma$  is the surface energy of the crack,  $E$  is Young's modulus and  $a$  is the length of the largest crack. Namazue *et al.* have measured the surface roughness of the beams by AFM and found that the maximum peak-to-valley distance matched the crack length  $a$  calculated by Eq. 4.1 when the corresponding fracture strengths were inserted. They suggest that the specimen size effect on the bending strength of silicon could be due to the different surface roughness of each specimen. However, they also point out that the essence of the size effect on the bending strength of silicon cannot be concluded until further experiments using different

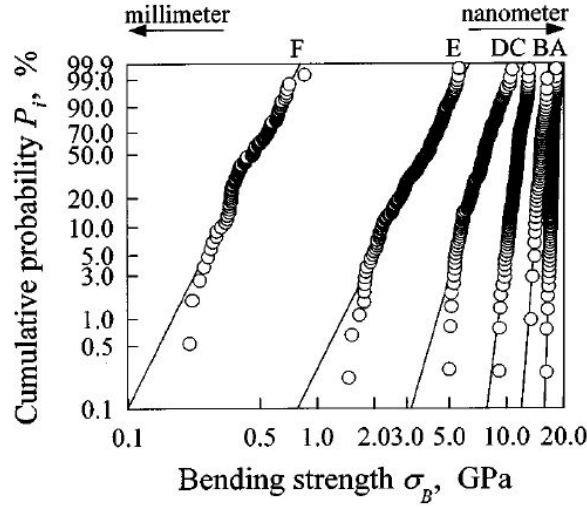


**Figure 4.1:** Weibull plots of the bending strength of Si beams along the  $\langle 110 \rangle$  direction etched out from a SOI wafer. The largest beam F has a lateral dimension of  $\approx 1$  mm, the smallest beam A of  $\approx 250$  nm. (From Namazu et al.<sup>72</sup>)

sized specimens with the same surface condition have been performed.

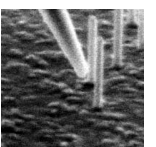
Measuring the fracture strength of bottom-up grown nanowires will allow a comparison of their structural quality to top-down processed silicon beams. Possibly, the fracture strength can give an indication if the fracture is initiated at the surface or in the bulk.

#### 4.1.2 Young's modulus

Where as Young's modulus of silicon beams<sup>72</sup> and silicon nanowires<sup>39,83</sup> has been measured to be conform with the bulk value, values for Young's modulus on ZnO nanowires found in the literature scatter from 29–220 GPa<sup>3,12,42,74,91</sup>.

There are several groups investigating the mechanical properties of crystals with reduced dimensions from a theoretical point of view. At the low level, atomistic simulations are performed, but they are restricted to geometries with some 10 atoms in diameter because the computation time becomes too important for larger structures. On a continuum mechanics level, the investigations concentrate on core-shell models, where the shell represents the surface. The next few paragraphs summarize the theoretical point of view, followed by a discussion of some experimental work published.

The reason for the apparent Young's modulus of a nanowire to be different from that of the bulk is that the surface in small structures becomes important as the surface over volume ratio increases. At the surface of a solid, the outer atoms rearrange themselves such that the potential energy is minimized. This changes their atomic coordination and electron distribution and thus the elastic properties of the material at the surface. To what extent the nanowires properties are influenced by this depends on the surface elasticity and its "thickness". Even for a given material, these properties depend on the surface orientation. For instance,



Zhou and Huang showed in molecular simulations on copper that Young's modulus along the  $\langle 110 \rangle$  direction on a  $\{100\}$  surface is larger than its bulk counterpart, whereas it is smaller along the  $\langle 100 \rangle$  direction on a  $\{100\}$  surface.<sup>117</sup>

For silicon, Park finds from calculations with a finite deformation continuum mechanics model on 10–30 nm wide beams that the resonance frequency shows little deviation from the prediction by continuum beam theory for diameters  $>30$  nm.<sup>80</sup> For smaller diameters, the surface stresses have a stronger impact on the resonant frequency of double clamped beams than for single clamped ones. Interestingly, size reduction leads to a lowering of resonance frequency for double clamped beams, but to an increase for single clamped beams. This translates into a decrease / increase in the effective Young's modulus, respectively. The surfaces of the examined beams are, however, “unreconstructed”, which might not be representative for a real silicon surface. In another continuum model, Miller *et al* find a decrease in Young's modulus as well.<sup>67</sup> For silicon  $\langle 100 \rangle$  beams, they investigate the rigidity in bending experiments (Young's modulus  $\times$  geometrical moment of inertia) and in tensile experiments (Young's modulus  $\times$  length). For flexural deformations, the surfaces carry the largest stresses and strains due to their larger distance from the neutral axis. For this reason the surface elasticity has a more pronounced contribution to the effective stiffness in a bent configuration than in an axial deformation. The effect, however, is small for nanowires with diameters  $>10$  nm, the 10% discrepancy limit from the bulk value lies at a beam diameter of 8.1 nm and 4.4 nm for the flexural and the tensile deformation, respectively.

The only experimental study on silicon's Young's modulus for different sized specimens in which a reduction in Young's modulus is observed was carried out on 12–300 nm thick cantilevers by Li *et al*.<sup>58</sup> Young's modulus is measured to be close to the bulk value in the thickest specimen, and it decreases down to a third of its value for the thinnest cantilever. The decrease in stiffness starts, compared to the theoretical work, already at relatively thick specimens, and extrapolating the data to thicker structures, Young's modulus seems to be higher than that of bulk Si. Also, the coverage of the surface by a  $\text{SiO}_2$  layer is not discussed. These facts lead to the suspicion that the surface of the cantilevers may have a larger influence than what they would have for a perfectly clean silicon surface, so that they are actually not measuring the properties of silicon. For larger structures (255 nm – 520  $\mu\text{m}$  in thickness), Namazu *et al* have not observed any change in Young's modulus,<sup>72</sup> and also for nanowires of 60–200 nm<sup>83</sup> and 100–200 nm<sup>39</sup> in diameter the stiffness is measured to be close to that of bulk Si. For silicon nanowires, Young's modulus can thus be expected to be that of bulk material.

For zinc oxide nanowires the theory remains the same. According to theoretical calculations, the rearrangement of the atoms penetrates 5–6 atomic layers into bulk<sup>66</sup>, but it is not clear if the surface is softer or stiffer. Accordingly, the surface stiffness is determined by fitting experimental data. Chen *et al* find Young's modulus to increase with decreasing diameter in ZnO nanowires<sup>12</sup>, and determine the surface to be stiffer with a thickness of 4.4 nm. Because of the similar crystallographic structure, they explicitly predict the same phenomenon for GaN nanowires, but on the other hand Nam *et al* therefore observe Young's modulus to decrease with decreasing diameter.<sup>71</sup> Lower values of Young's modulus in ZnO nanowires or nanobelts are found to be  $\approx 58$  GPa in a mechanical resonance experiment<sup>42</sup>,  $\approx 52$  GPa in dual-mode resonance<sup>3</sup>,  $(31 \pm 2)$  GPa in a 3-point bending test with an AFM<sup>74</sup> and  $(29 \pm 8)$  GPa in a

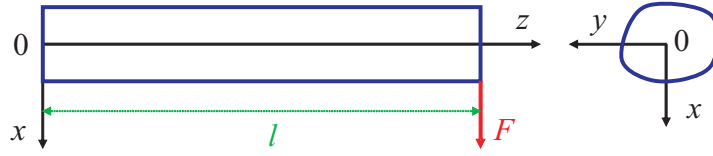


**Figure 4.2:** Configuration of a bending experiment on a bar with arbitrary but constant cross-section.

single clamped nanowire bending experiment with an AFM<sup>91</sup>. The large variety of the values published shows that experimentally it is unclear, whether the stiffness of ZnO nanowires is comparable to that of bulk ZnO.

The experimental data published on Young's modulus of ZnO nanowires are all extracted from flexural configurations, either in vibration or bending experiments. A special effort is thus undertaken in this work to measure Young's modulus of ZnO nanowires in a tensile experiment, where the whole nanowire is strained uniformly, in order to be less influenced by the nanowire surface.

## 4.2 Linear beam theory

In this work the strength of nanowires is measured in bending and in tensile experiments. In none of the experiments plastic deformation was observed deflecting the nanowires. Even strongly deflected nanowires (deflection/length > 0.3) return back to their original position when released. All strain measured can thus be assumed to be purely elastic. Consequently, in the bending and tensile experiments, the strain in the nanowire can be calculated with elastic beam theory. A large collection of formulas for all kind of geometries and situations has been established by Timoshenko.<sup>102</sup> This section points out the formulas used for the mechanical characterization.

### 4.2.1 Bending experiment

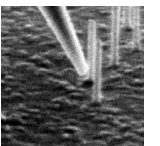
The bending configuration as we encounter it in the experiments is sketched in Fig. 4.2. The nanowire is fixed at the plane  $z = 0$  and bent by a force  $F$  acting at the nanowires end perpendicular to its axis. Both normal and shearing stresses are present in the nanowire.

The normal stress over a cross-section at a distance  $z$  from the fixed end is

$$\sigma_z = -\frac{F(l-z)x}{I} \quad (4.2)$$

where  $F$  is the applied force,  $l$  the length of the bar and  $I$  the geometrical moment of inertia. For a circular cross-section with diameter  $d$ ,  $I = d^4\pi/64$ , and so the tensile stress becomes  $\sigma_z = -64Fx(l-z)/(\pi d^4)$ . The maximum stress occurs on the nanowires' surface at its fixed end,

$$(\sigma_z)_{\max} = -\frac{32Fl}{\pi d^3} \quad (4.3)$$



The calculation of the shear stress  $\tau$  is more complicated and depends on the cross section shape of the bar. For a circular cross section, the maximum shearing stress occurs at the center ( $y = 0$ )<sup>102</sup>,

$$\tau_{\max} = \frac{(3 + 2m)Fr^2}{8(1 + m)I} = \frac{2(3 + 2m)F}{\pi(1 + m)d^2} \quad (4.4)$$

where  $m$  is Poisson's ratio.

Equating Eq. 4.3 and Eq. 4.4 the maximum shearing and normal stresses are equal when

$$l = \frac{(3 + 2m)}{16(1 + m)}d \approx 0.2d \quad (4.5)$$

where a Poisson's ratio of 0.3 has been used. As the nanowire is always longer than it is wide, the shearing stress is lower than the tensile stress, so the highest stress can be calculated by Eq. 4.3.

If the force  $F$  in Eq. 4.3 is unknown, it can be replaced by the deflection  $s$  of the nanowire via the nanowires spring constant  $k$ . For the bending experiment,  $k = 3EI/l^3$  where  $E$  is Young's modulus. To calculate the maximum strain induced in a nanowire, the definition of Young's modulus used is  $E = \sigma/\epsilon$  and the spring constant for a circular cross section is injected via the force  $F$  into Eq. 4.3 to get

$$\epsilon_{\max} = \frac{3}{2} \frac{d}{l^2} s . \quad (4.6)$$

The validity of Eq. 4.6 for the particular shape of the nanowire root and the relatively low length/width ratios were examined by the finite element method (FEM) as presented in Sect. 4.4.1.

### 4.2.2 Tensile experiment

In the tensile experiment a bar of arbitrary but constant cross-section is fixed at both its ends and stressed along its axis (all other stresses being zero). The stress is calculated by the applied force  $F$  and the bar's cross-section area  $A$ ,  $\sigma = F/A$ . For a nanowire with diameter  $d$ ,

$$\sigma = \frac{4F}{\pi d^2} . \quad (4.7)$$

With the initial length  $l_0$  and the length  $l$  of the strained nanowire, Young's modulus  $E$  is calculated by measuring the strain  $\epsilon = (l - l_0)/l_0$ ,

$$E = \frac{\sigma}{\epsilon} = \frac{l_0}{l - l_0} \sigma . \quad (4.8)$$

## 4.3 Experimental

### 4.3.1 Manipulation setup

Figure 4.3 shows an image of the manipulation setup used to manipulate the nanowires inside the SEM. A probe from an AFM (AdvanceTEC, 45 N/m, Nanosensors, Neuchâtel, Switzerland) is mounted on a piezoelectric slip-stick robot arm (MM3A, Kleindiek Nanotechnik,



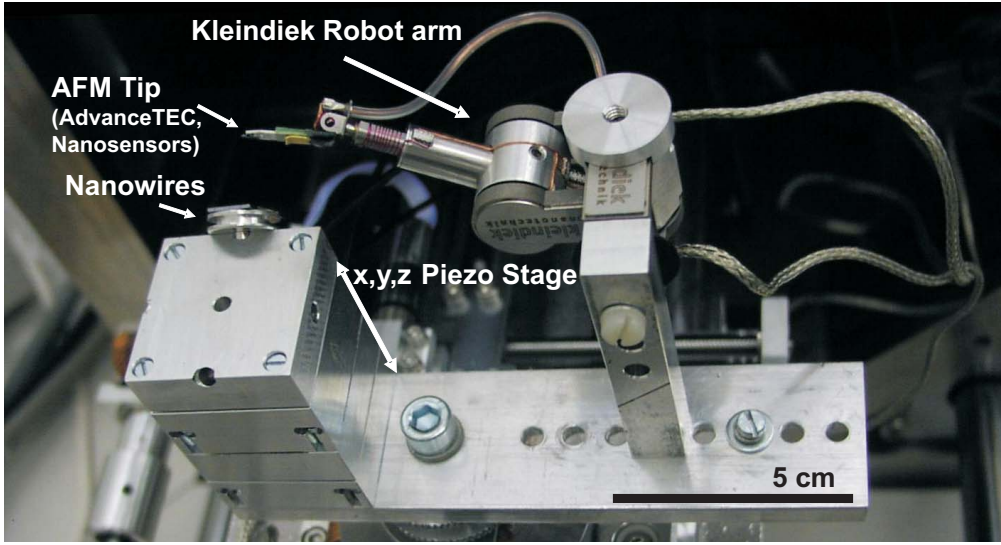
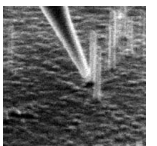


**Figure 4.3:** The experimental setup used for bending, pulling and manipulating nanowires. The whole setup is mounted in a SEM.

Reutlingen, Germany) with two rotational and one linear axis. The substrate with the nanowires is mounted on a x,y,z piezo stage (P-620.2CD and P-62.ZCL, Physik Instrumente (PI), Karlsruhe, Germany) with 50  $\mu\text{m}$  range and a sub-nanometer resolution. The whole setup is mounted inside a SEM (Hitachi Science Systems, Japan, S-3600N) such that the nanowires are at an angle of  $60^\circ$  with the scanning electron beam. With the SEM table, the nanowire of interest is moved in the field of view. With the robot arm the AFM tip is coarsely positioned toward the sample, and the fine positioning as well as the bending of the nanowire is achieved by moving the sample with the x,y,z piezo stage. The manipulation is recorded in a video file for post manipulation data analysis.

In the bending experiment the nanowires are bent perpendicularly to the electron beam, so that the deflection  $s$  can be read out directly from the SEM image. Figure 4.4(a-c) shows a series of images extracted from the recorded video file. In the majority of cases, the AFM tip is not applied at the free end of the nanowire, but somewhere in the middle along its length. The bent section is then shorter than the nanowire, which gives the possibility of artificially shortening the length of the bent nanowire in order not to get too large deflections. From the last image before failure, the maximum strain  $\epsilon_{\text{max}}$  is calculated by Eq. 4.6.

In the tensile experiment the AFM tip is first brought into mechanical contact with the top of the nanowire. By scanning the electron beam for a couple of minutes over the contact region, carbonaceous contaminants originating from the sample surface and the residual gas of the SEM chamber are deposited at the interface. This forms a joint that is stronger than the nanowire itself and allows on the nanowire to be pulled until it fractures (Fig. 4.4(d-f)). From the back leap  $t$  of the cantilever at fracture and its spring constant  $k$ , the applied force at fracture  $F = kt$  is calculated (Fig. 4.4f)). Prior to the experiment, the nanowires are imaged with a field emission SEM (S4800, Hitachi Science Systems) to measure their diameter. The



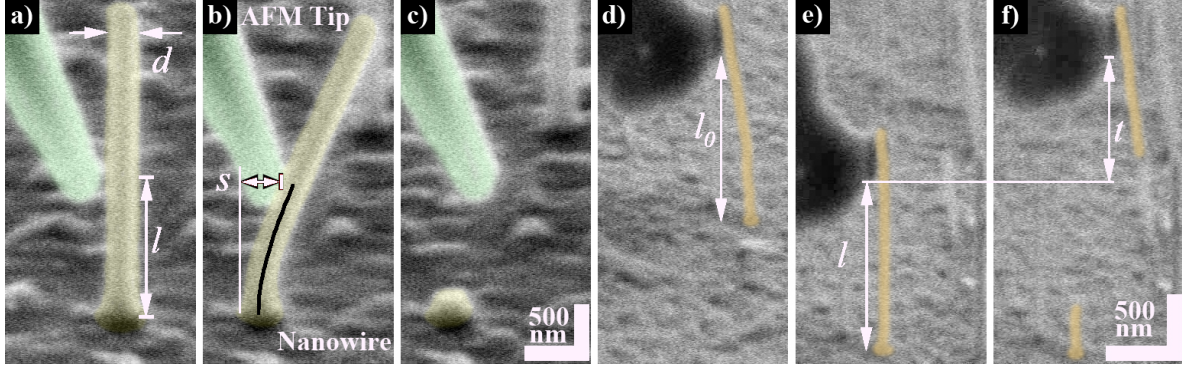


**Figure 4.4:** a)–c): Sequence of a bending experiment. b) shows the last image before fracture from which the deflection  $s$  can be read out. The black overlaid line gives a visual comparison of the curvature of a straight, clamped beam to that of the nanowire. d)–f): Sequence of a tensile experiment. Note the precurved shape of the nanowire in d), and that it is straight just before fracture in e). In f) the AFM tip snaps back to the original position it had in d), which shows that no vertical stress is exerted on the nanowire at the beginning of the experiment. This is important for the measurement of Young’s modulus.

fracture stress of the nanowire is then calculated by Eq. 4.7. During retraction of the nanowire from the AFM tip the cantilever bends and causes an undesired deflection of the nanowire. This can partly be compensated for by moving the nanowire laterally, but because of the rigidity of the AFM tip–nanowire bond the nanowires still bend a little. To minimize the curvature at failure, the nanowires are prebent in the opposite direction before they are firmly attached to the AFM tip by pulling on them horizontally (Fig. 4.4d)).

To calculate Young’s modulus from the tensile experiment the critical parameter to extract is the length difference  $l - l_0$  because of the limited resolution of the SEM. Therefore **Spotfinder** was programmed, an image analysis tool based on a cross correlation algorithm to locate the position of the tip–nanowire joint and the root of the nanowire in each image of the video file (presented in the next section). Despite the noise present in the images, the localization accuracy still is  $\pm 1$  pixel. The length difference  $l - l_0$  typically spans 10 pixels so the strain can be determined within  $\pm 10\%$ . With the stress measured at failure, Young’s modulus was calculated according to Eq. 4.8. Slipping between the tip and the nanowire would show up as a jump in the strain curve recorded by **Spotfinder**, but was never observed.

### 4.3.2 Spotfinder

To accurately calculate the strain of the nanowire in a tensile experiment, **Spotfinder** has been programmed. It is an image analysis tool able to track objects in an image sequence such as the video files recorded during an experiment. The straining of a nanowire can be extracted by tracking its root as well as the tip and following the change in distance between the two objects. Fredrik Östlund, PhD student at EMPA, has contributed equally to the development of **Spotfinder**.

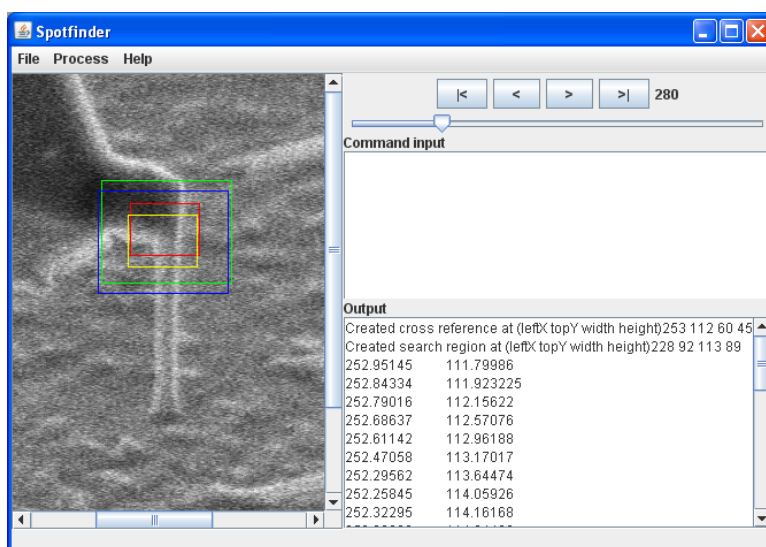


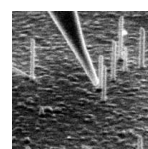
**Figure 4.5:** The program *Spotfinder*, a tool able to track objects in an image sequence. It can be operated through the menus, by writing the commands to the command line or by opening a script containing commands, which allows to run it in batch mode.

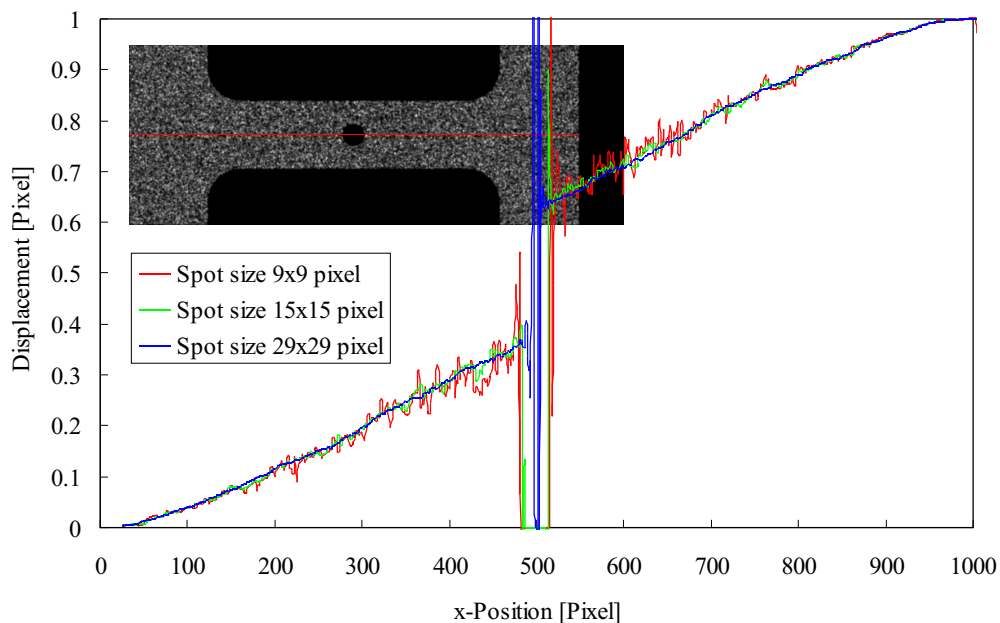
### Operation principle

Figure 4.5 shows the graphical user interface of *Spotfinder*. In red the original position of the object to be tracked that was defined in the first image is indicated. To minimize computing costs, an region of interest around the object to be tracked is selected (green), in which *Spotfinder* tries to locate the object. In the present image, *Spotfinder* calculates the cross correlation of the object at each position within the region of interest. This yields a value representing the similarity of the object and the image section for each position. The position with the highest value is the approximate position of the object (yellow). To achieve sub-pixel resolution, a second order polynomial is fitted to the similarity values in a reduced section around the maximum value (typically in a field of  $7 \times 7$  pixels). The  $(x, y)$  coordinates of the maximum of this fitted polynomial yields the position of the object with sub-pixel resolution. For the next image, the region of interest in which the object is searched is updated according to the present position (blue).

### Accuracy for a simulated experiment

To test the sub-pixel resolution a tensile test has been simulated by Ondrej Papes (PhD student at ETHZ). The simulation consists of two noise free images of a bar, first in the unstrained and second in a strained state. The bar is 1000 pixels wide, fixed at one end and stretched by exactly one pixel at the other end. Figure 4.6 shows the bar geometry in the inset. *Spotfinder* has tracked the displacement of squares of different sizes all along the horizontal center line of the bar (red line in the inset). The graph shows the displacement of these squares in function of their position, it is 0 at the fixed end and 1 pixel at the opposite side. In the





**Figure 4.6:** Examination of the *Spotfinders* resolution by means of a simulated tensile experiment. The displacement of spots located along the red line in the inset are tracked, the resulting resolution is well below 0.1 pixel for a spot size down to  $9 \times 9$  Pixels.

center of the bar, where the black hole is, there is nothing to hold on to so *Spotfinder* gets lost. The resolution is below 0.1 pixel for all spot sizes, and the smaller the spot size is the noisier the displacement curve becomes.

### Accuracy for a real experiment

The images of the SEM are quite noisy because they were taken with a low integration time in TV mode, which is necessary in order to manipulate the nanowire in real time. The image in Fig. 4.5 is an example of relatively little noise. Figure 4.7 shows the positions of different objects *Spotfinder* has extracted at each frame of the video. For instance, the blue line shows the vertical position of the nanowire footing, and the purple line shows the position of the tip. At frame 550 one can see a large jump in the tip position, this is the moment the nanowire fractured and the tip leaps back. *Spotfinder* gets lost because the region in which it searches the tip was chosen too small.

In the graph on the right a small section where two objects are tracked is magnified. Different lines show the results of objects at the same position but with different sizes. The displacement curves are much noisier than the ones from the noise free images, but the accuracy is still  $\pm 1$  pixel.

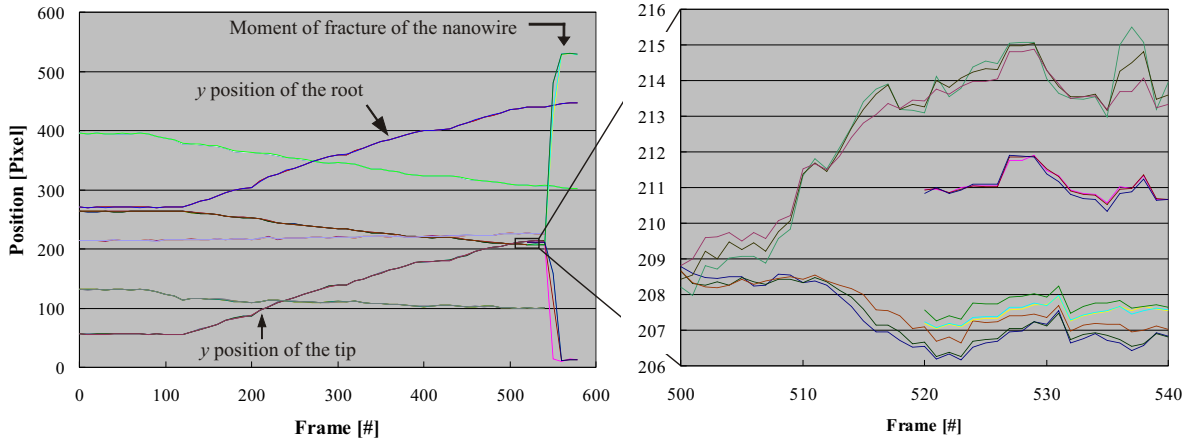


**Figure 4.7:** Positions of different spots in a tensile experiment. In the magnification on the right hand side one can distinguish the lines originating from different ranges of the fitting algorithm. Because of the noisy SEM images, the accuracy is not as good as in the simulated experiment, but still  $\pm 1$  pixel.

## 4.4 Results

### 4.4.1 FEM calculations on a bent nanowire

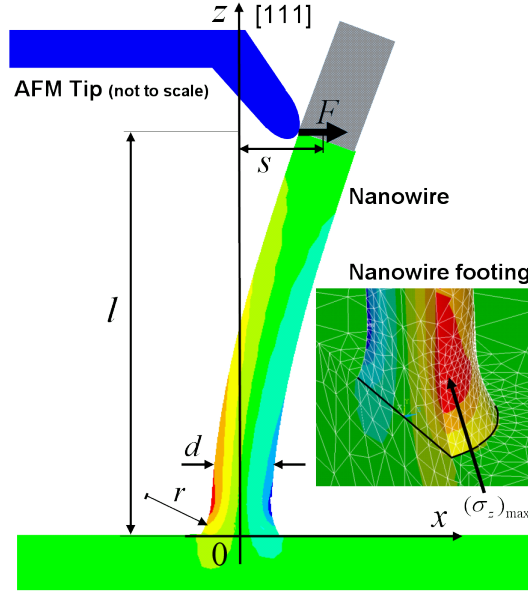
In order to verify the accuracy of Eq. 4.6 of the bending experiment, FEM analyses are carried out with the commercial program *Ansys*. The experiment differs from the ideal case through the elastic substrate (the nanowire is not firmly fixed at its root), the particular shape at the nanowire footing, the relatively low length/width ratios and the large deflections at fracture. Figure 4.8 shows the simulated geometry. Simulations were performed for different length/width ratios and various deflections. The radius of curvature at the nanowire footing is approximately the same as the width of the nanowire, as can be seen in the magnified image in Fig. 4.10 for the silicon nanowire and in Fig. 4.11 for the zinc oxide nanowires. The anisotropy in elasticity of silicon has been taken into account in the 3D simulations, but it turned out that it had little effect on the results when compared to isotropic simulations.

Fig. 4.9 shows the simulated strain maximum at the nanowire's root compared to the analytic strain calculated by Eq. 4.6. At large length/width ratios and small deflections, the influence of the substrate and the nanowire footing can be analyzed. The elastic substrate tends to release some of the strain in the nanowire, the simulated strain is thus expected to be smaller than the analytical one. In contrast, the widening at the footing leads to higher strains. As in a bent bar, the strain at the surface is proportional to the distance from the neutral line (Eq. 4.2). From the simulation at a deflection of  $s = 0.1l$  for an aspect ratio of  $l/w = 25$  we can see that the widening of the footing dominates and the calculated strain underestimates the real strain by  $\approx 6\%$ .

At large deflections, the analytic calculation underestimates the actual strain by up to 15%, but low length/width ratios are counteracting this underestimation. The field that







**Figure 4.8:** Finite element analysis of a bent nanowire. The upper part of the nanowire above the tip–nanowire contact is free of deformation and needs to be taken into account in the analysis. Inset: A detail of the FEM simulation shows that the maximum tensile stress occurs where the nanowire becomes thicker, above the sharp corner to the substrate.

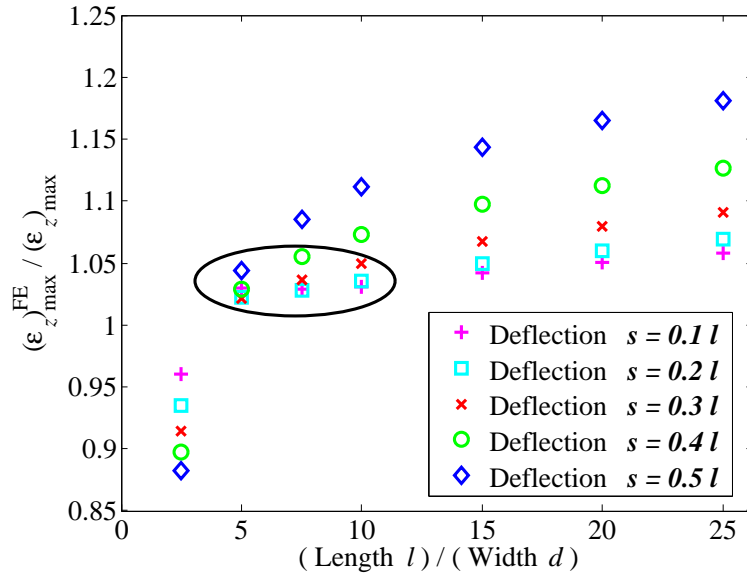


**Figure 4.9:** 3D FEM calculations of the maximum strain  $(\epsilon_z)_{\max}^{FE}$  compared to the analytic linear beam result  $(\epsilon_z)_{\max}$  (Eq. 4.6). The ellipse indicates the region of length/width ratios and deflection of the nanowires that were used in the experiments.

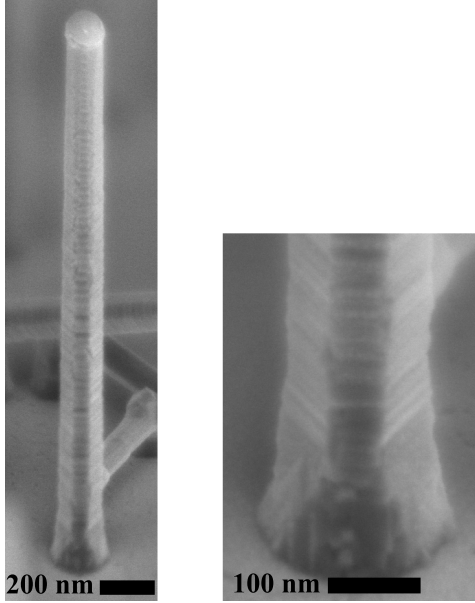


**Figure 4.10:** SEM image of a nanowire from the sample that was subjected to the bending experiment.

$d$ [nm]	$l$ [nm]	$s$ [nm]	$l/d$ [1]	$(\epsilon_z)_{\max}$ [%]	$(\epsilon_z)_{\max}^{FE}$ [%]
170	1650	370	9.7	3.5	3.8
125	1500	480	12.0	4.0	4.5
190	2000	580	10.5	4.1	4.6
90	600	130	6.7	4.9	4.9
115	1200	400	10.4	4.8	5.2
120	850	230	7.1	5.7	5.9
120	880	250	7.3	5.8	6.1
125	750	190	6.0	6.3	6.3
160	1050	300	6.6	6.5	6.7
130	750	215	5.8	7.5	7.5
150	760	210	5.1	8.2	8.0
120	500	135	4.2	9.7	8.9
100	570	210	5.7	9.7	9.6
Average $(\epsilon_z)_{\max}$ , $(\epsilon_z)_{\max}^{FE}$ :				$6.2 \pm 2.1$	$6.3 \pm 1.8$

**Table 4.1:** Measured bending strengths of the silicon nanowires calculated by means of the analytic beam formula  $((\epsilon_z)_{\max})$  and by FEM  $((\epsilon_z)_{\max}^{FE})$ .

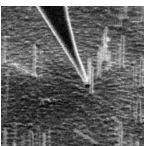
corresponds to the actual parameters from the bending experiment is indicated by the black ellipse. According to the FEM analysis, the net underestimation of strain by the analytical formula is 2–5%.

In Fig. 4.4(b) the curvature of the nanowire is visually compared to the theoretical curvature of a clamped beam whose deflection is proportional to  $z^2(3l - z)$ , where  $z$  is along the long nanowire axis (black line). One can see how the stiffening at the root alters the bending profile, as the black line is not in the middle of the nanowire throughout the whole length.

#### 4.4.2 Results on silicon nanowires

The nanowires examined in the bending experiment were grown by the VLS growth mechanism in a UHV environment using gold as a catalyst and diluted silane as a precursor (partial pressure 10 Pa). The growth temperature was set to 500 °C. The resulting nanowires had an average diameter  $d$  of approximately 100 nm and an aspect ratio  $l/d \geq 10$ . Details of the growth process are described elsewhere<sup>85</sup>. Figure 4.10 shows SEM images of a nanowire from the examined sample. Their diameter ranges from 100–200 nm, and they have a length of up to 2  $\mu\text{m}$ . The sample was prepared by Volker Schmidt in the group of Stephan Senz at the Max Plank institute in Halle (D).

Table 4.1 shows the measured bending strength together with the dimension of the nanowires. The average bending strength is  $(6.3 \pm 1.8)\%$ . A few nanowires withstand strains up to 10%.



### 4.4.3 Results on zinc oxide nanowires

Zinc Oxide nanowires from 3 different growth processes were analyzed. They were all synthesized via thermal evaporation and deposition inside a horizontal split quartz tube furnace (Carbolite HST 12/400). An alumina boat loaded with a ZnO and graphite powder mixture (1:1 weight ratio) was located at the center of the third heating zone. The substrates, *a*-plane oriented  $\alpha$ -Al<sub>2</sub>O<sub>3</sub> sapphire single crystals, were coated with a thin sputtered 3 nm Au film. The substrate was then placed above the source boat. The reaction tube was heated up by 20 °C/min to the desired temperatures and cooled down naturally to room temperature after the experiments. For samples A, B, and C the temperatures were 850, 850, and 820 °C respectively and the corresponding dwelling times were 3, 2.5, and 2.5 h. The chamber pressure was maintained at 200 mbar by a constant flow of Ar gas and pumping. The residual air in the chamber provided the oxygen. Because of the similarity of their growth conditions the sample A, B, and C are indistinguishable from one another in terms of overall size and crystal structure (wurtzite, growth along [0001]). The only difference that could matter for this study is the crystalline quality, i.e. the defect density, which depends on the local Zn and O vapor concentrations during growth.

Under these synthesis conditions it is most likely that both VLS and vapor–solid mechanisms play a role in the growth. On one hand, the molten gold provides the necessary nucleation sites for Zn/ZnO vapors, leading to a vapor–liquid–solid growth process; on the other hand, vapor–solid can be a dominant growth process at temperatures in the range of 820–850 °C, giving rise to widening of the diameters via a lateral growth<sup>25</sup>. The density of nanowires on the substrate is relatively low, which is convenient for single nanowire manipulation by the AFM tip. A nanowire of each sample is shown in Fig. 4.11. The samples were prepared by Hongjin Fan in the group of Margit Zacharias at the Max Plank institute in Halle (D).

The overall geometry of all 50 experiments together with the measured strengths and Young’s modulus from the bending and tensile tests are listed in Table 4.2 and Table 4.3, respectively. The average maximum strain measured in the bending experiment was  $(7.7 \pm 0.8)\%$  for sample A. The average tensile fracture strength was  $(4.0 \pm 1.7)$  GPa,  $(3.7 \pm 1.3)$  GPa and  $(5.5 \pm 1.4)$  GPa for sample A, B and C respectively. The measured Young’s modulus of sample C is  $(97 \pm 18)$  GPa.

### 4.4.4 Error analysis

All the parameters that enter the calculations are extracted directly or indirectly from SEM images, their accurate reading thus determines the accuracy of the experiments. The user introduces a statistical error when measuring the data in the images, and the SEM adds an systematic error because of its finite precision. Table 4.4 shows how the different measurement inaccuracies enter the uncertainty of the measured bending strain, tensile stress and Young’s modulus.



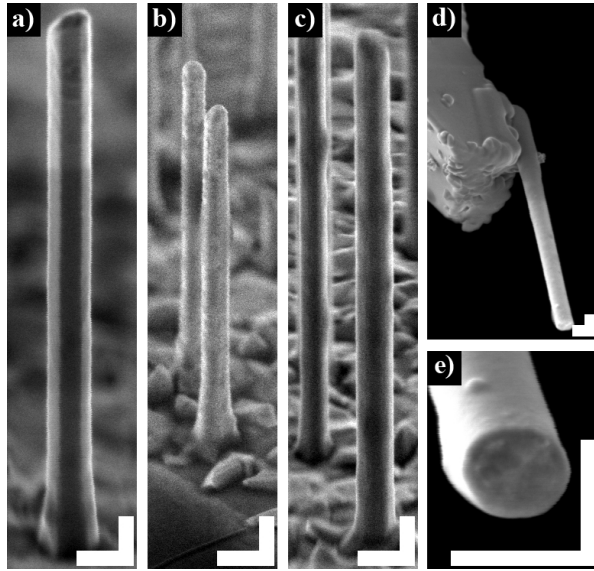


**Figure 4.11:** SEM images of the ZnO nanowires. a) to c): Nanowires of samples A, B and C respectively. d) Nanowire attached to an AFM tip by EBeam induced contamination deposition. e) Fracture surface of a nanowire from a tensile test. All scalebars correspond to 250 nm, because of the view angle the vertical direction is contracted.

Sample A			
$l$ [ $\mu\text{m}$ ]	$d$ [ $\mu\text{m}$ ]	$s$ [ $\mu\text{m}$ ]	$(\epsilon_z)_{\text{max}}$ [%]
.98	.19	.20	5.9
.98	.17	.27	7.2
.93	.20	.20	7.2
1.0	.19	.27	7.3
2.3	.23	1.2	7.4
1.1	.22	.27	7.7
1.1	.21	.31	7.7
1.6	.22	.64	7.9
1.1	.19	.33	8.0
.82	.18	.20	8.2
.80	.18	.19	8.3
1.1	.18	.37	8.4
1.1	.31	.23	9.0
Average $(\epsilon_z)_{\text{max}}$ :			$7.7 \pm 0.8$

**Table 4.2:** The results of the bending experiment together with the dimensions of the ZnO nanowires tested.

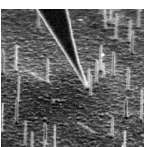
### Bending strength

The nanowires subjected to the bending experiment have been imaged in a tungsten filament SEM. Assuming it is perfectly calibrated (but taking into account its finite resolution), the user can measure the nanowire diameter with an accuracy of about 10%, and its length and deflection with an accuracy of about 5%. This induces a statistical error on  $(\epsilon_z)_{\text{max}}$  of 15%. The SEM introduces a systematic error through its calibration and its characteristics such as the electron beam diameter and the image contrast. If these effects are assumed to limit the accuracy to 5%, then an error of up to 20% may arise.

### Tensile strength

The nanowire diameter enters squared into Eq. 4.7 and is thus the major error source. At a measurement accuracy of 10% it sets the statistical uncertainty to 20%. The statistical error on the back leap  $t$  of the cantilever is small as it spans more than 100 pixels and is measured with an accuracy of 1 pixel with **Spotfinder**.

In the tensile experiment the force constant of the cantilever enters through  $F = kt$  into the calculation of tensile strength and Young's modulus. The cantilevers spring constant is calculated by an anisotropic finite element model including the cantilever holder and the tip,



Sample A				Sample B				Sample C						
$l_0$	$d$	$t$	$\sigma$	$l_0$	$d$	$t$	$\sigma$	$l_0$	$l - l_0$	$d$	$t$	$\epsilon$	$\sigma$	$E$
$\mu\text{m}$	$\mu\text{m}$	$\mu\text{m}$	GPa	$\mu\text{m}$	$\mu\text{m}$	$\mu\text{m}$	GPa	$\mu\text{m}$	$\mu\text{m}$	$\mu\text{m}$	$\mu\text{m}$	%	GPa	GPa
2.0	.24	1.8	1.7	2.0	.13	.54	1.8	3.1	.10	.14	1.1	3.3	3.3	100
1.4	.20	1.4	1.9	2.3	.11	.63	2.5	3.1	.13	.10	.74	4.2	4.0	94
2.2	.17	1.3	2.4	2.1	.14	1.1	2.9	2.6	.11	.11	.95	4.3	4.5	104
2.0	.22	2.2	2.6	2.0	.10	.58	3.0	2.4	.11	.14	1.7	4.6	4.6	100
2.2	.21	2.3	2.9	1.7	.13	.92	3.0	2.8	.16	.11	.95	5.6	4.7	83
2.6	.20	2.7	3.5	1.2	.12	.90	3.2	2.4	.20	.10	1.0	8.0	5.8	72
1.9	.18	2.6	4.2	1.5	.11	.91	3.6	3.5	NA	.11	1.4		6.1	
2.4	.15	1.7	4.2	1.3	.076	.41	3.6	2.5	.13	.13	2.0	5.0	6.5	130
2.2	.20	3.6	5.0	1.5	.11	.87	4.0	2.8	NA	.13	2.1		6.9	
2.7	.15	2.1	5.1	2.1	.073	.43	4.1	2.6	NA	.15	3.0		7.3	
2.3	.16	2.5	5.5	2.0	.10	.84	4.3	2.6	NA	.13	2.2		7.3	
2.6	.13	1.8	5.8	1.4	.090	.92	5.8							
2.0	.16	3.5	7.5	.77	.060	.48	6.8							
Average $\sigma$ : $4.0 \pm 1.7$				Average $\sigma$ : $3.7 \pm 1.3$				Average $\epsilon$ , $\sigma$ , $E$ : $5.0 \pm 1.5$ , $5.5 \pm 1.4$ , $97 \pm 18$						

**Table 4.3:** The results of the tensile experiment including Young's moduli together with the dimensions of the ZnO nanowires tested.

	Equation	Statistical error	Systematical error
Bending strength	$(\epsilon_z)_{\max} = \frac{3}{2} \frac{d}{l^2} s$	$\frac{\delta(\epsilon_z)_{\max}}{(\epsilon_z)_{\max}} = \sqrt{\frac{\delta d^2}{d^2} + \frac{4\delta l^2}{l^2} + \frac{\delta s^2}{s^2}}$	$\frac{\delta(\epsilon_z)_{\max}}{(\epsilon_z)_{\max}} = \frac{\delta d}{d} + \frac{2\delta l}{l} + \frac{\delta s}{s}$
Tensile strength	$(\sigma_z)_{\max} = \frac{4kt}{\pi d^2}$	$\frac{\delta(\sigma_z)_{\max}}{(\sigma_z)_{\max}} = \sqrt{\frac{4\delta d^2}{d^2} + \frac{\delta t^2}{t^2}}$	$\frac{\delta(\sigma_z)_{\max}}{(\sigma_z)_{\max}} = \frac{\delta k}{k} + \frac{2\delta d}{d} + \frac{\delta t}{t}$
Young's modulus	$E = \frac{l_0}{l-l_0} \sigma$	$\frac{\delta E}{E} = \sqrt{\frac{\delta[l_0/(l-l_0)]^2}{[l_0/(l-l_0)]^2} + \frac{\delta \sigma^2}{\sigma^2}}$	$\frac{\delta E}{E} = \frac{\delta[l_0/(l-l_0)]}{l_0/(l-l_0)} + \frac{\delta \sigma}{\sigma}$

**Table 4.4:** The sources of the measuring errors for the calculation of bending and tensile strength as well as Young's modulus.

based on the dimensions measured in the SEM. The error on the spring constant thus also originates from the SEM measurements and enters as a systematical uncertainty of about 15%. This error does not enter into the statistical error because the same cantilever was used for several measurements.

In addition to the cantilever stiffness, the measurement of its back leap and the nanowire diameter each contribute 5% to the systematic error. The diameter is measured in a field emitter SEM prior to the experiment, the two contributions thus do not partly cancel as the formula would suggest. Together with the 15% from the spring constant the systematical error adds up to 25%.

### Young's modulus

For the determination of Young's modulus, the extraction of the strain,  $l_0/(l - l_0)$ , is a statistical error source due to the limited resolution of the SEM. With **Spotfinder** one locates the position of the tip–nanowire joint and the nanowire footing in each image of the video file. Despite of the noise present in the images, the accuracy is still  $\pm 1$  pixel (see Fig. 4.7). The length difference  $l - l_0$  typically spans 10 pixels so the strain can be determined within  $\pm 10\%$ . Together with the contribution of the stress, the statistical uncertainty on Young's modulus is raised to 22%.

The systematical error of the strain is negligible since a ratio of two lengths is measured; only image distortion falsifies the ratio and this is small compared to the systematical error that enters through the measurement of the diameter. As for the tensile stress, the systematical error on Young's modulus is thus 25%.

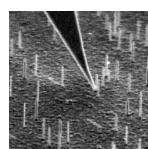
## 4.5 Discussion

### 4.5.1 Silicon nanowires

#### Comparison to literature

Although brittle materials have a probabilistic behavior in their mechanical properties, the scatter of the bending strength is expected to be smaller for such small specimens. Namazu *et al.*<sup>72</sup> have found an average strain to failure of  $9.3 \pm 0.2\%$  for micromachined silicon beams (along the  $\langle 110 \rangle$  direction) of 6  $\mu\text{m}$  length and around 250 nm in diameter. This corresponds to a scatter of  $\pm 2\%$ , whereas for 5 of our nanowires which have the same length of about 800 nm, the scatter is  $\pm 15\%$ , which is also expected from the error analysis. Aside from measurement inaccuracy, the high scattering could be due to the presence of surface or interfacial defects at the nanowire footing, which lead to a stress concentration and initiate failure there. However, the nanowires are essentially free of extended volume defects and their influence is expected to be low as deduced from transmission electron microscopy.

Tabib *et al.* have reported bending strengths of VLS grown nanowires that are more than 10 times lower than the values we measure.<sup>97</sup> The reported fracture strains, 0.16%, 0.30% and 0.45%, were read out from AFM force–deflection curves on 3 nanowires that had about the same diameter as our nanowires but were much longer (10  $\mu\text{m}$ ). Their results can only be



explained in comparison to our results and results on the micromachined silicon from Namazu if defects played a dominant role in those experiments.

### Fracture strength compared to the theoretical limit

The relation between the stress  $\sigma$  and strain  $\epsilon$  in a solid body is usually described by Hooke's law which postulates a linear relation between the two. The constants of proportionality are called the *second-order* stiffnesses. This term originates from the calculation of the deformation energy for finite strain, the second order stiffnesses being the first non-zero terms.

Although adequate for many purposes, Hooke's law does not always hold; in particular, under finite strain conditions, as they occur in the present experiments, most second-order stiffnesses are found to increase with stress. This can be accounted for by adding terms of squares and products of the strains to the stress-strain relationship. The new proportionality constants are termed *third order* elastic constants.

Ondrej Papes<sup>i</sup> has investigated different models from molecular dynamic simulations and quantum physics in order to find the "correct" constitutive equations for silicon. Figure 4.12 shows the resulting stress-strain curves from an implementation of the Brugger model<sup>100</sup> with the stiffness constants up to the third order. For the growth direction of the nanowires ( $\langle 111 \rangle$ , red curve), failure is predicted at  $\approx 16\%$  strain in tensile load. The measured bending strengths of around 6% are thus not quite at the theoretical limit.

### Possible initiation of fracture

Structural defects such as cracks are the reason why materials fracture below the theoretical limit. Griffith's theory introduces a ellipsoidal crack and calculates the stress  $\sigma_m$  occurring locally at the tip apex due to stress concentration.<sup>30</sup> The stress at the end of a elliptical crack is

$$\sigma_m = 2\sigma\sqrt{a/\rho} \quad (4.9)$$

where  $\rho$  is the radius of curvature at the crack tip,  $a$  half of the ellipse major axis and  $\sigma$  the stress far away from the crack.

According to Griffith's theory, the crack propagates (and leads to failure) if an increase in  $a$  releases more energy (from elastic energy around the crack) than is needed to create the new surface of the crack. The calculations are presented in a paper by Orowan.<sup>77</sup> The surface energy per unit thickness is  $W_S = 4\gamma a$ , and the work done by the external force is  $W_e = \pi a^2 \sigma^2 / E$  (corresponding to the difference in elastic energy in the material with and without crack). The critical stress  $\sigma_f$  for a crack length  $a$  can then be calculated by setting

$$\frac{\partial}{\partial a}(W_e - W_S) = 0 \quad (4.10)$$

and is found to be Eq. 4.1

$$\sigma_f = \sqrt{\frac{2\gamma E}{\pi a}} \quad (4.11)$$

---

<sup>i</sup>PhD student in the group of Prof. E. Mazza, ETH Zürich, Switzerland

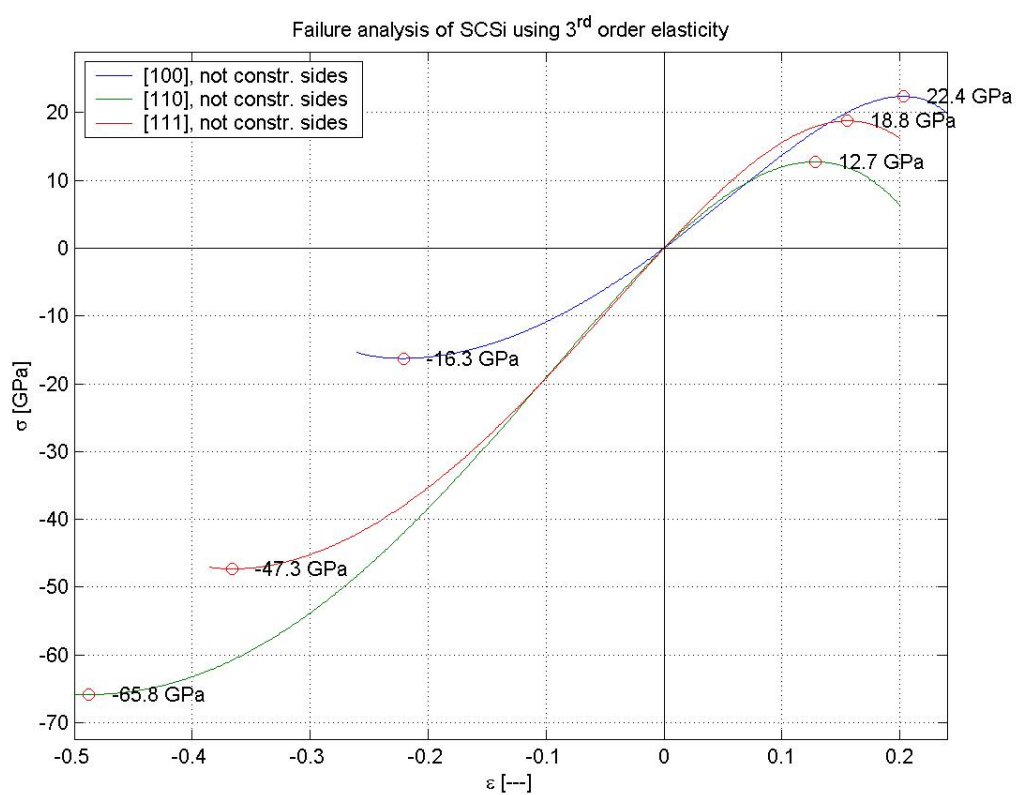
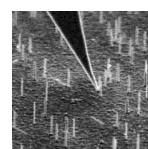


**Figure 4.12:** Non-linear stress-strain curve for unconstrained silicon, simulated with the Brugger model. From Ondrej Papes.



According to Fig. 4.12, up to the measured fracture strain of 6%, stress is still linear to strain, and the fracture stress is around 11 GPa. With a surface energy of  $1.23 \text{ Jm}^{-2}$  for the silicon (111) plane<sup>45</sup>, the crack length corresponding to the measured fracture strength is  $a = 1.2 \text{ nm}$ .

Although Griffiths theory is based on some geometrical assumptions, it gives an order of magnitude of the spatial extension of the defects present. In Fig. 4.10 one can see that the surface of the nanowire is not flat, but there are ripples with a period of about 10 nm. The resolution of the SEM does not permit the shape of a ripple apex to be seen, but the calculated crack length for the measured fracture strength suggests that it is a stress concentration around the tip of these ripples that leads to failure of the nanowire.

### Brittle fracture versus plastic deformation

As already mentioned, plastic deformation is not observed in the bending experiments. All nanowires return back to their original position when released. But brittle fracture is not the only mechanism causing silicon to fail. At elevated temperatures or under a hydrostatic pressure (e.g. directly under the tip in an indentation experiment), silicon is known to deform plastically.<sup>114</sup> In indentation experiments, a hydrostatic pressure under the tip can suppress crack formation.

Interestingly, plastic deformation of thin silicon nanowires along the  $\langle 100 \rangle$  axis is reported for compression experiments.<sup>78</sup> Nanowires with a diameter  $< 310 \text{ nm}$  show a ductility comparable to that of metals, whereas nanowires with diameters  $> 400 \text{ nm}$  develop cracks. The transition from brittle to ductile behavior is explained by different activation energies of partial dislocations, into which a propagating full dislocation is split. If the dissociation distance between the two partials is larger than the nanowire diameter, the partial with the lower activation energy can transverse the nanowire without the need of the second partial to nucleate, and thus lead to plastic deformation. If the dissociation distance is smaller than the diameter of the nanowire, the partial with the higher activation energy needs to be nucleated as well. This limits the rate at which dislocations are created, such that the nanowire cannot accommodate the imposed deformation plastically and thus will fail through brittle fracture. Compression experiments, however, differ from bending experiments in the aspect that, in bending, a part of the sample is subjected to tensile stresses.

For tensile experiments, however, plastic deformation is reported as well. Kizuka *et al* observe plastic deformation in a 6 nm thin nanowire, created by pushing an AFM into a silicon substrate and slowly retracting it inside a TEM.<sup>49</sup> After attaining the elastic limit at 10% strain, the nanowire deforms plastically before it fractures at 27%. Plastic deformation and even transformation into an amorphous structure for 30–70 nm wide nanowires is observed by Han *et al*.<sup>34</sup> They disperse nanowires on a TEM grid and image them using TEM. Under strong electron irradiation, the TEM grid deforms slightly, which strains the firmly enough attached nanowires. The strong electron irradiation, however, could not only be responsible for the bending of the TEM grid, but also be the reason for the plastic deformation of the nanowire. High energy electrons might break bonds by kicking out secondary electrons, which facilitates the movement of atoms to an extent that large strains can be sustained.

5 nm wide silicon nanowires are simulated by molecular dynamics to investigate the fracture

mechanism in tensile experiments.<sup>47</sup> These predict that at room temperature the nanowires fail under brittle fracture, and a brittle-to-ductile transition occurs at higher temperatures only. The model also predicts that  $\langle 111 \rangle$ -oriented nanowires should be more brittle than  $\langle 110 \rangle$ -oriented nanowires.

Taking into account these considerations, the observed fracture of the nanowires in the presented bending experiment is expected to be of brittle nature.

### 4.5.2 Zinc Oxide nanowires

#### Bending and tensile strength

The bending experiments of sample A show a strength two times larger than the tensile experiments. Also, there is less scatter in the bending experiment data. This can be explained by the fact that only a small volume is highly stressed in the bent nanowire. So it is less probable to encounter a structural defect that could initiate failure than in a tensile stressed nanowire, where the whole nanowire is highly stressed.

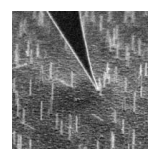
In the tensile test the nanowires either shattered or broke into two pieces at failure. Those that shattered showed a higher strength than those that broke into two pieces, probably because of the lack of a dominant defect that otherwise would have led to an early failure at a specific location. At high stresses, more elastic energy is stored in the nanowire. The liberation of this elastic energy is assumed to be the cause of shattering of the highly stressed nanowires. For the nanowires that broke into two pieces, the fracture surface was always a (0001) plane (Fig. 4.11e), the cleavage plane of ZnO. In spite of the care taken to avoid a lateral deflection of the nanowire at failure, deflections up to a tenth of the nanowire length occurred. However, the measured strength does not correlate with this lateral deflection.

Fracture strength of ZnO nanowires has been measured by only one other group so far. By picking and placing a nanowire on a micro tensile stage, Desai *et al* have measured the tensile fracture stress to lie between 7–22 GPa.<sup>21</sup> The higher fracture stresses were observed for nanowires with a diameter of 220 nm, whereas the lower values originated from thicker nanowires (480 nm). This is considerably more than the 3.7–5.5 GPa measured in the present work.

#### Young's modulus

Young's modulus of ZnO nanowires has been measured by several groups, but with somewhat different results. It has been measured to be  $\approx 58$  GPa by a mechanical resonance experiment<sup>42</sup>,  $\approx 52$  GPa by dual-mode resonance<sup>3</sup>,  $(31 \pm 2)$  GPa by a 3-point bending test with an AFM<sup>74</sup> and  $(29 \pm 8)$  GPa by a single clamped nanowire bending experiment with an AFM<sup>91</sup>. Only Chen *et al* observed a size dependence of Young's modulus.<sup>13</sup> In a resonance experiment they measured 140 GPa for nanowires with diameters larger than 200 nm and up to 220 GPa for nanowires with a diameter down to 50 nm.

All of these experiments measured Young's modulus by bending nanowires, which is generally referred to as the bending modulus. The tensile experiment has the advantage that the stress distribution is uniform throughout the nanowire.  $E$  can thus be determined directly by its definition,  $E = \sigma/\epsilon$ . A non uniform diameter at the nanowire footing has a stronger



influence on the data extracted from a bending or a resonance measurement than on the data from a tensile experiment. Although the statistical and systematical errors in the present work are considerably high, they are still lower than the scatter of the values found in the literature.

For hexagonal structures, such as wurtzite, there are 5 independent stiffness coefficients and the stiffness matrix has the form<sup>51</sup>

$$\mathbf{E} = \begin{bmatrix} E_{11} & E_{12} & E_{13} & 0 & 0 & 0 \\ & E_{11} & E_{13} & 0 & 0 & 0 \\ & & E_{33} & 0 & 0 & 0 \\ S & & & E_{55} & 0 & 0 \\ & Y & & & E_{55} & 0 \\ & & M & & & \frac{E_{11}-E_{12}}{2} \end{bmatrix} \quad (4.12)$$

For bulk ZnO, these coefficients are

$E_{11}=209.7$  GPa,  $E_{12}=121.1$  GPa,  $E_{13}=105.1$  GPa,  $E_{33}=210.9$  GPa,  $E_{55}=42.47$  GPa.<sup>110</sup>

In direction of the growth axis of the nanowire ([0001], that is the  $z$ -direction), the stiffness can be computed to be  $E=144$  GPa.

The measured value of 97 GPa thus lies 33% below the value of bulk material. The cumulative systematical error originating from the cantilever calibration and the determination of the nanowire diameter in the calculation of the stress could be responsible for the lower value measured. Physical reasons for a lower modulus could be vacancies present in the nanowires. The effect of temperature on the Young's modulus can be neglected. Using the 1-dimensional heat equation and the heat conductivity of bulk ZnO, it can be shown that the temperature is not increased by more than 1 °C, assuming that all the energy of the electron beam is absorbed at the top of the nanowire and that no heat is extracted by the AFM tip, but that the substrate is a perfect heat sink.

In the present work, Young's modulus is measured in tensile experiments, where the nanowire is stressed uniformly throughout its volume, contrary to the moduli found in the literature that are measured in bending configurations. Also, the experiment presented does not involve any friction, contrary to the deflection of a nanowire with an AFM tip. Because of the lack of error analyses in other publications, Young's modulus of ZnO nanowires with diameters down to 100 nm can thus be expected to be close to the bulk modulus.



## Chapter 5

# Electromechanical characterization

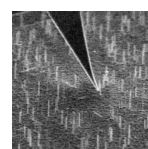
### Abstract

An approach to measure electrical properties of silicon nanowires at high strains is presented. The experiment is based on growing the nanowires between a silicon socket and a bendable silicon cantilever, such that the nanowires can be highly strained by pulling on the cantilever with a nanomanipulator. If the doping concentrations match, the epitaxial interfaces between the nanowire and the structure sidewalls result in negligible contact resistances. For undoped nanowires, however, the contacts to the highly doped substrate reveal a non-linear  $U$ - $I$  characteristic, which makes it impossible to extract electromechanical properties of the nanowire in this 2 point configuration. Initial mechanical results demonstrate that the nanowires can be strained up to 5.5%.

This work has been carried out in close collaboration with Mathias Steinmair at the Technical University of Vienna (A).

### 5.1 Motivation

The piezoresistance effect of silicon has been widely used in mechanical sensors<sup>103,104,108</sup>, and is now actively explored in order to improve the performance of silicon transistors<sup>36,54</sup>. Even at relatively low strain, He *et al* have measured the piezoresistive coefficient of silicon nanowires to be up to  $37\times$  higher than that of bulk silicon.<sup>38</sup> They grow the nanowires in trenches on a SOI wafer and bend the whole sample in order to strain the nanowires. Because of the brittle nature of the substrate, however, they reach strains up to only 0.04%. The bending experiments on silicon nanowires, presented in Chp. 4, show that the Si nanowires can sustain strains beyond 6%. The motivation behind an alternative experiment is to measure the piezoresistance of silicon nanowires at strains close to the limit of fracture. Beyond the technological interest, this could also reveal interesting effects in silicon conductivity, because the lattice constant stretched by 6% in one axis might change the band diagram significantly.



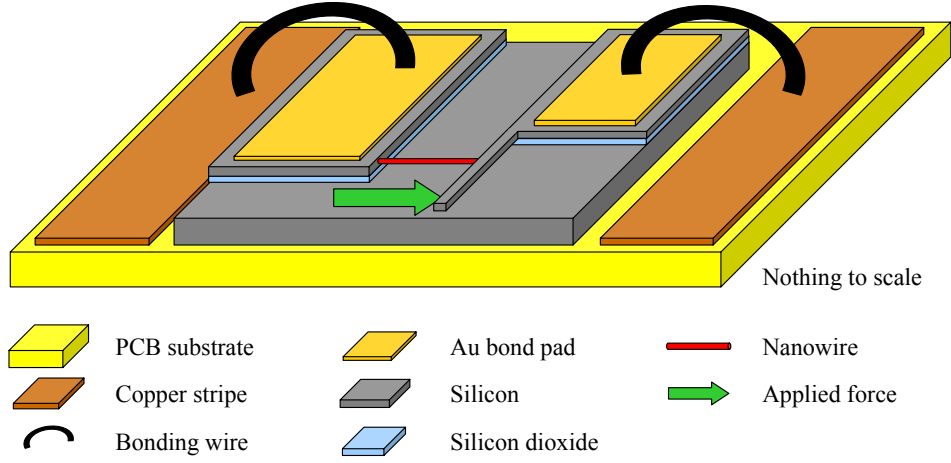


**Figure 5.1:** Principle of the electromechanical experiment to measure the electrical properties of a silicon nanowire in function of strain.

## 5.2 Experiment

The principle of the experiment is shown in Fig. 5.1. A SOI wafer is used as a base material, and, in the device layer, a structure consisting of a socket and a cantilever is formed. The  $\text{SiO}_2$  under the cantilever is removed, such that it is freestanding. Growing the nanowire between the socket and the cantilever allows it to be pulled by pushing on the cantilever. The geometry of the test structure insures that only the nanowire is highly strained, preventing failure of the cantilever. The chip may be mounted on a printed circuit board (PCB) and the pads can be bonded to copper stripes for convenient connection to the measurement apparatus.

The process flow is sketched in Fig. 5.2, the process steps are as follows:

- (a) Initial material is a SOI wafer with a (110) orientation of the device layer. On top, a layer of  $\text{Si}_3\text{N}_4$  is grown. The  $\text{Si}_3\text{N}_4$  layer is patterned with a circle 4 mm in diameter consisting of 80 squares by photolithography and reactive ion etching (RIE) ( $\text{SF}_6$ , at room-temperature). Using the  $\text{Si}_3\text{N}_4$  square openings as an etch mask, the underlying silicon device layer is unisotropically attacked in KOH at 80 °C, which results in characteristic edges along the Si (111) planes. These edges are visible through the  $\text{Si}_3\text{N}_4$  layer under a light microscope and are used in the next process step as alignment marks.
- (b) The cantilever structure is aligned to the sample such that the cantilever sidewall will be a Si (111) plane. In the design presented later, a total of 120 structures are fabricated within the 4 mm wide circle. The pattern is transferred by photolithography, the  $\text{Si}_3\text{N}_4$  is etched by RIE ( $\text{SF}_6$ , at room-temperature).
- (c) The  $\text{Si}_3\text{N}_4$  is used as an etch mask for the RIE process to transfer the pattern into the silicon layer ( $\text{SF}_6 + \text{O}_2$  at  $-108$  °C). Alternatively, KOH may be used to etch the silicon, which would result in flatter sidewalls. It is, however, more difficult to control

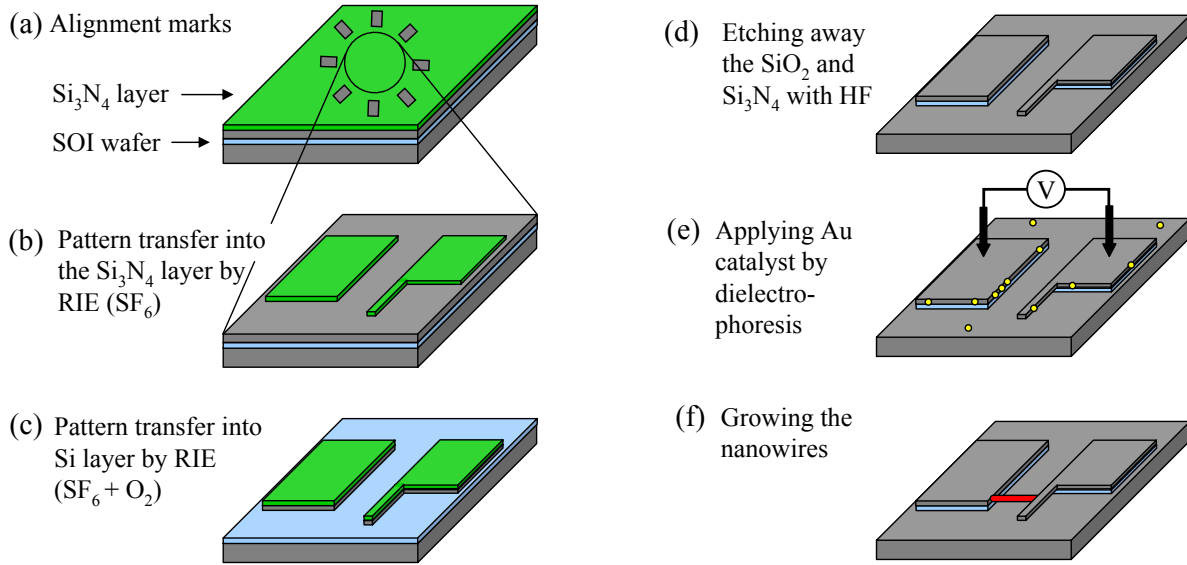


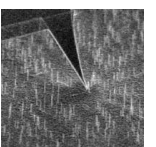
**Figure 5.2:** Process for fabricating nanowires between a silicon socket and a bendable silicon cantilever: (a) Fabrication of alignment marks; (b) Transferring the pattern into the silicon nitride layer; (c) Transferring the pattern into the device layer; (d) Removing the silicon nitride and silicon dioxide; (e) Applying Au collides; (f) Growing the nanowires (only one is drawn).

the uniformity, and in our experience structures have been etched away at some places while others were still short circuited at other places.

- (d) With HF the SiO<sub>2</sub> as well as the Si<sub>3</sub>N<sub>4</sub> layer are attacked. The cantilever is thin enough such that all the SiO<sub>2</sub> is removed underneath it. The SiO<sub>2</sub> layer must not be etched away completely, just enough in order that the cantilevers are freestanding. A thin layer at the bottom prevents short circuits between the socket and the cantilever through nanowires that grow from the socket to the bottom and from the bottom to the cantilever base.
- (e) By dielectrophoresis (100 kHz, 20 V<sub>pp</sub>, ≈ 3 s) Au colloids suspended in isopropanol are applied to the trench sidewalls. The colloid density is highest where the electric field is highest, which, in the design presented below, is between the cantilever and the socket.
- (f) The nanowires are grown by the VLS process.

### 5.3 Results

Figure 5.3 shows the design at different magnifications: (a) shows one of four fields with 30 cantilevers. The two pads on the top are used to connect the AC voltage for the dielectrophoresis to apply the gold colloids, the one on the left connects all cantilevers whereas the one on the right is connected to all sockets. The interconnections in between the sockets and cantilevers are very thin, such that a single structure with a good nanowire can be isolated easily by

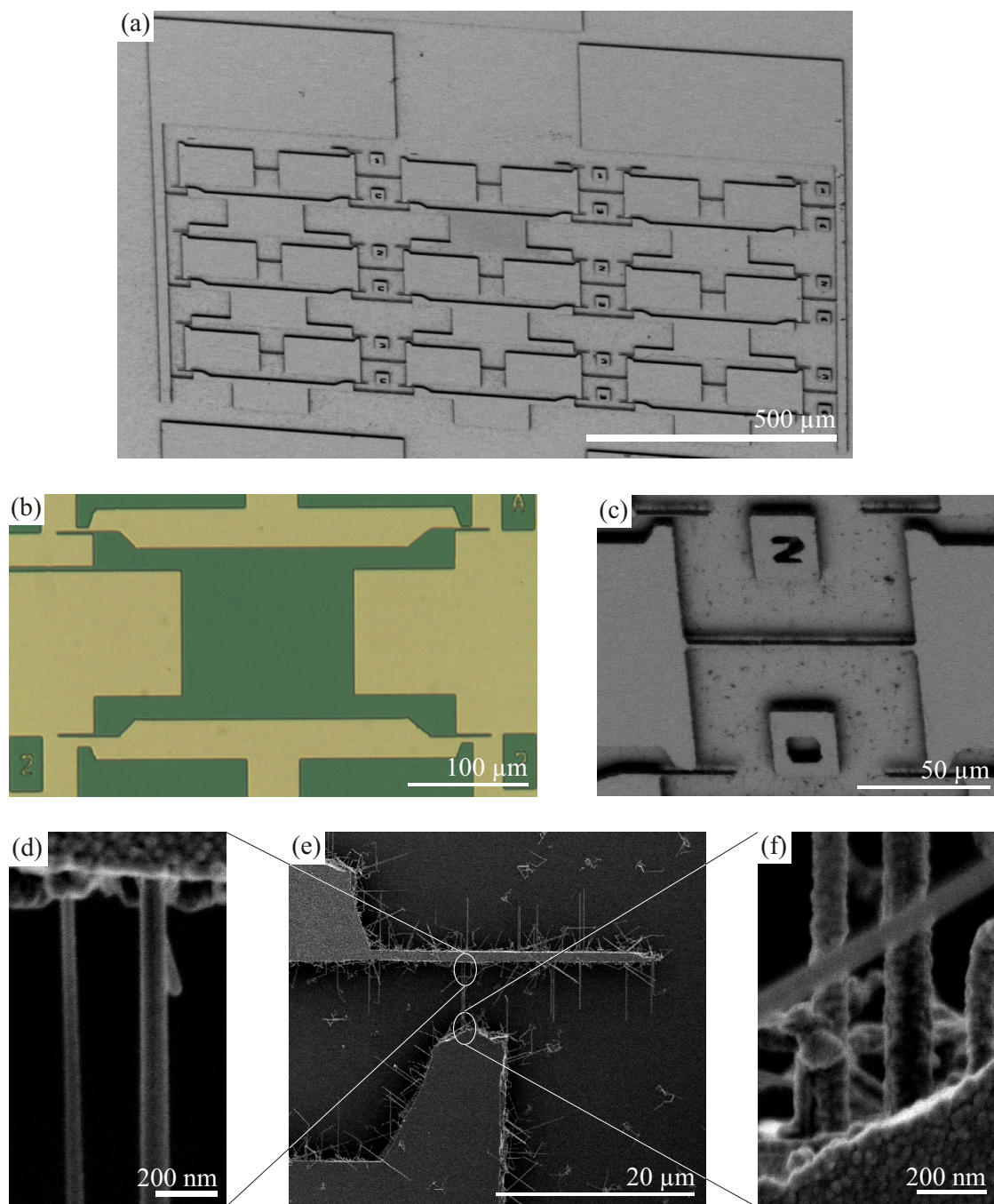


just braking the interconnect with a probe needle under a light microscope. In (b) and (c) a light microscope and a SEM image is shown, top view and inclined, respectively. There are 4 structures that differ in the distance between the cantilever and the socket, nominally these are 2, 4, 6 and 10  $\mu\text{m}$ . (d)–(f) finally show a structure where two nanowires are grown between the cantilever and the socket. In this sample, the dielectrophoresis did not work well, as can be seen in the uniform distribution of nanowires all over the cantilever and socket sidewalls. Figure 5.4 shows structures of another sample where the dielectrophoresis was successful.

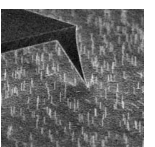
The SOI wafer used is highly *p*-doped ( $< 10^{-3} \Omega\text{cm}$ ) and the nanowires are grown by the VLS process with Au as a catalyst (3 mbar, 10 sccm  $\text{H}_2$  + 100 sccm  $\text{SiH}_4$  (2% in He), 500  $^\circ\text{C}$ , 100 min). No dopants are added during growth because this is not available in the system they were grown in. Accordingly, it is not surprising that the  $U$ – $I$  curve is dominated by the nanowire–structure contact, as shown by the non-linear characteristic in Fig. 5.4. The curves are recorded by contacting the socket and cantilever base directly with probe needles of a prober station. 2 point measurements with the probe needles on a bulk wafer with the same doping concentration show that the needle–silicon contact resistance is much smaller than what is presented in Fig. 5.4, and can thus be neglected. Because of the dominant nanowire–silicon sidewall contacts, no information on the nanowires characteristics under strain can be extracted. Nevertheless, mechanical experiments are performed in order to check the mechanical strength of the interface where the nanowire impinges on the opposite side.

Figure 5.5 presents the mechanical experiment. The nanomanipulator used is the same as the one presented in Sect. 4.3.1. (a) and (b) show the orientation of the AFM tip, coming from the top. (c)–(e) show 3 frames of the video sequence recorded. In frame 38 the tip does not touch the cantilever yet, frame 78 is the last image before fracture of the joint. It is not clearly seen from frame 78 to frame 79 that the cantilever makes a jump, but this becomes evident in the video. Also, from the video it can be seen that only the one nanowire encircled in (c) is holding the cantilever back, and that the nanowire–cantilever interface is the weakest point where it breaks off. This is at the thin end of the nanowire, thus the nanowire has grown from the base to the cantilever.

Although the joint is weaker than the nanowire, the nanowire is strained by 5.5% before fracture, revealed by **Spotfinder** and shown in Fig. 5.5(f). This is close to the fracture limit of the nanowire itself (around 6%), as it is measured in the bending experiments.



**Figure 5.3:** SEM images of two nanowires in a Silicon trench.



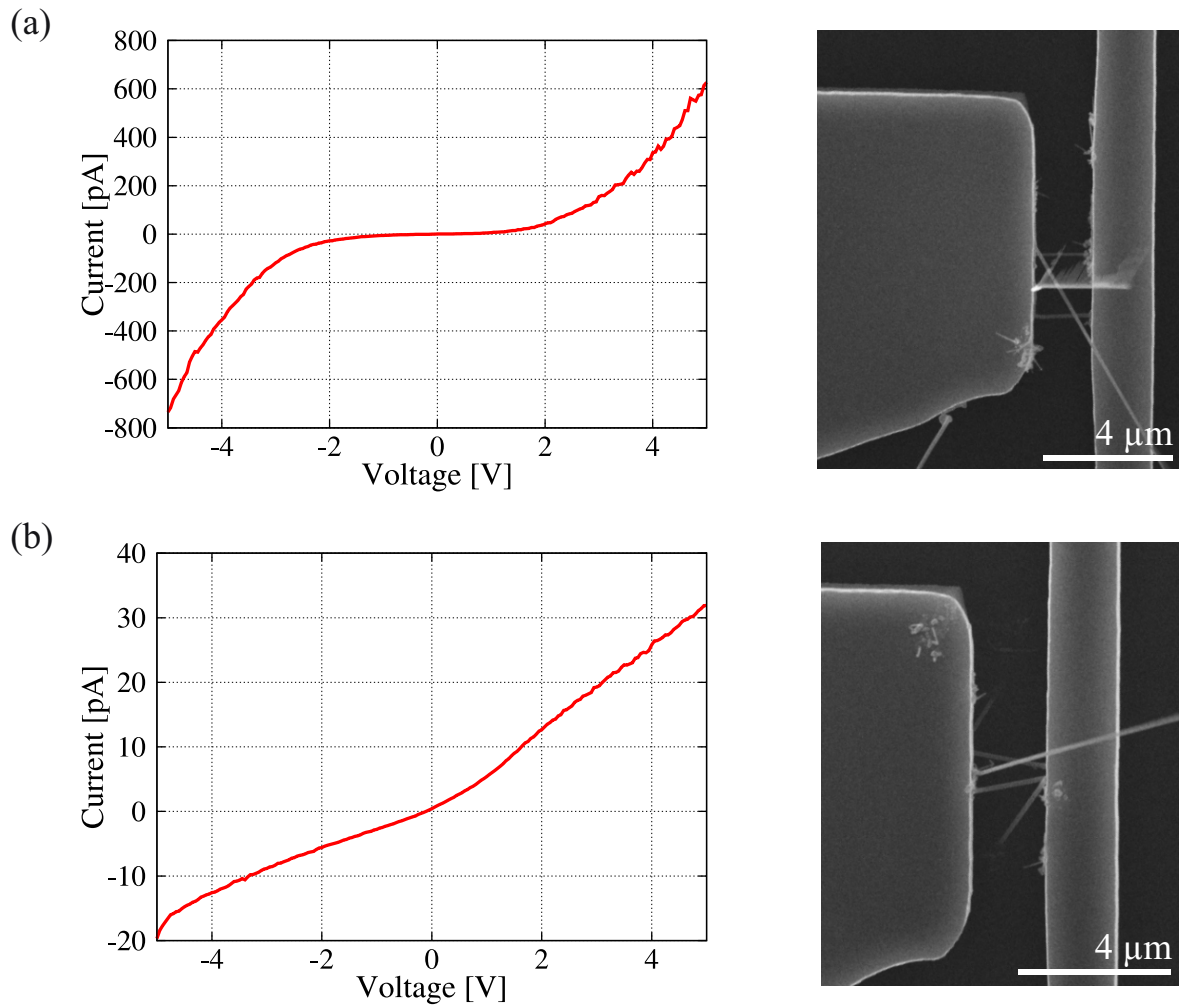


**Figure 5.4:**  $U$ - $I$  Characteristics of undoped nanowires grown between a Si socket and a Si cantilever.



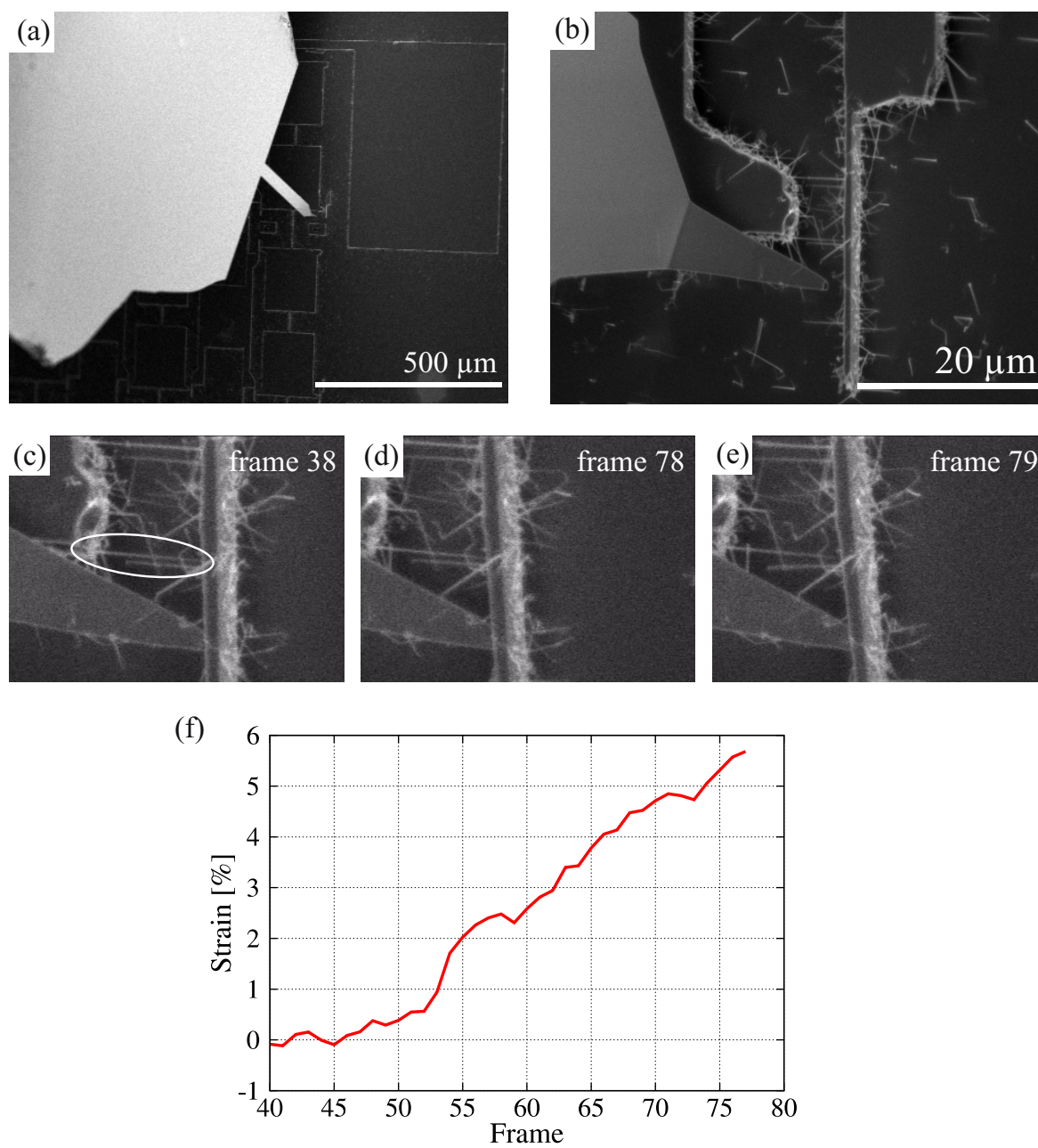
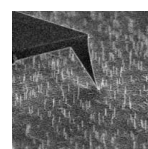


**Figure 5.5:** The mechanical strength of the joint of the nanowire to the trench sidewall in a tensile test.



## 5.4 Discussion

The mechanical investigations show that the attachment of the nanowire is strong enough to strain the nanowire almost up to its fracture limit. This shows that not only the joint at the nanowire root, but also the joint, where the nanowire grows onto the silicon sidewall, is free of major structural defects. This result is promising for a good electrical contact as well.

Electrical characterization is performed on non-doped nanowires and shows, not surprisingly, that the contact resistances dominate. For an undoped nanowire it is thus not possible to extract electromechanical characteristics of the nanowire itself. However, growing doped nanowires should overcome this problem. It is shown by different groups that undoped nanowires make an ohmic contact to bulk silicon.<sup>11,38</sup> This will allow a measurement of the electrical properties of silicon close to its fracture strength.



## Chapter 6

# Conclusions and perspectives

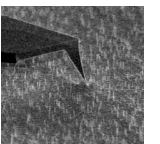
This thesis presents new techniques for the electrical and mechanical characterization of nanowires and applies them to silicon and zinc oxide nanowires.

Theoretical aspects of semiconductor physics reveal that contact characteristics require four point measurements for a reliable measurement of the nanowire resistance. Self-heating of the nanowire is shown to be a very fast process, but does not raise the temperature significantly under normal conditions. The influence of the nanowire surface is theoretically investigated and reveals that for doping concentrations below  $10^{18} \text{ cm}^{-3}$  the change in the effective cross section of the nanowire cannot be neglected.

Four point measurements on nanowires doped during growth show that silicon nanowires can be highly doped by adding diborane and phosphine to the growth chamber. By connecting eight electrodes to a same nanowire, it is shown, for the first time, that the doping concentration is not constant but decreases by about a factor of 2 from the nanowire bottom to the top. Ti/Au electrodes make an ohmic contact to the bottom of the nanowire, whereas the electrodes along the nanowire axis have a much higher contact resistance and are non-linear.

A technique based on EBIC imaging is developed for the characterization of very short nanowires. Experiments with post-growth doped nanowires reveal that *p-n* junctions can be implanted by ion implantation. The series resistance in the circuit is too large to extract the resistance of a uniformly doped nanowire in the two point measurement. But the contact characteristics show thermionic field emission, indicating that the effective doping concentration lies between  $10^{18}$  and  $10^{20} \text{ cm}^{-3}$ , which compares well to the simulated doping concentration of  $1.3 \times 10^{19} \text{ cm}^{-3}$ . The presented technique is fast and cheap, compared to EBeam lithography, and can be applied to a variety of other structures and materials.

To characterize nanowires mechanically, a novel nanomanipulation setup within a SEM is developed. It allows bending and tensile experiments to be performed on single nanowires, measuring their fracture strength and elastic properties. The technique introduced is fast, it allows many experiments to be made for statistics, and it is reliable, because from the SEM one gets a visual feedback in real time. An image analysis tool is programmed for the precise and automated extraction of data from the experiments. It allows objects to be followed in an image sequence with subpixel resolution. FEM calculations verify the limits within which the elastic beam formula is valid, for the specific case of nanowires, taking into account their



particular shape at the footing, the substrate, and the relatively low aspect ratio.

Specifically, it is shown that silicon and zinc oxide nanowires can be grown virtually defect free, as deduced from mechanical testing in bending and tensile configurations. Silicon nanowires exhibit a bending strength of  $(6.3 \pm 1.8)\%$  (average  $\pm 1$  standard deviation), which is much closer to the theoretical limit of 16% than that of micro and millimeter sized samples. It is shown that they are ripples at the nanowires surface that might be responsible for a stress concentration leading to failure. For zinc oxide nanowires, the fracture strain of  $(7.7 \pm 0.8)\%$  measured in the bending test reveals a strength about twice as high as measured in the tensile test. From the tensile experiments, Young's modulus is measured to be within 35% of that of bulk ZnO, contrary to the lower values found in the literature.

Finally, an experiment is presented for the electromechanical characterization of silicon nanowires at very high strains. The experiment is based on growing a nanowire between a silicon cantilever and a fixed base, where the epitaxial contacts provide an ohmic contact. The nanowire can be examined electrically while being strained, pulling on the cantilever with a nanomanipulator. A first device is made, and mechanical investigations show that the attachment of the nanowire is strong enough to strain the nanowire almost up to its fracture limit. Electrical characterization is performed on non-doped nanowires and shows that the contact resistances dominate, which prevents the extraction of electromechanical characteristics of the nanowire itself. Growing doped nanowires, however, should overcome this problem, as shown by different groups that they make an ohmic contact to the bulk silicon.<sup>11,38</sup> The presented experiment allows the investigations of He *et al* on the piezoresistance of silicon nanowires<sup>38</sup> to be carried out with strains over 100 times higher than the original experiment. This will allow a measurement of the electrical properties of silicon close to its fracture strength.

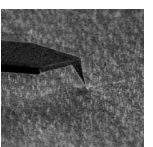
Among the interesting extensions of this work certainly would be the further development of the electromechanical characterization experiment by growing doped nanowires. This would overcome the contact problems that persist with undoped nanowires.

Other aspects to develop are:

- the examination of the doping gradient in nanowires that are doped during growth. For instance, by growing two samples, one being doped in the lower part but not in the upper part (turning the doping gas source off halfway through the growth process) and one being doped at the top but not at the bottom (turning on the doping gas source halfway through the growth process). It is possible that a simultaneous growth of a heavily doped shell is responsible for the higher conduction at the bottom of the examined sample in this work. If this is the case, then the undoped part of the first test sample would not conduct, whereas the undoped part in the second test sample would be covered by a conductive layer and thus show an apparent doping.
- the use of a nanowire as a strain sensor. Nanowires have already been used as fingers in a multiprobe for electrical characterization of fragile nanostructures.<sup>60</sup> One could also imagine using nanowires as fingers in a nanogripper. By exploiting their electromechanical properties, the strain can be measured electrically and used as information on the

force applied to the structure that is manipulated. The signal can be transferred to a force feedback joystick, facilitating the manipulation when the visual feedback is not sufficient because of the SEM resolution or the lack of the third dimension.

- the silicon nanowire could be covered with hydrogenated amorphous silicon in an attempt to passivate its surface. As shown in this thesis, surface effects are effectively screened only for relatively high doping concentrations,  $\geq 10^{19} \text{ cm}^{-3}$ . If the nanowire is not used as a sensor, its surface has to be passivated for a reliable functioning in various conditions. Hydrogenated amorphous silicon has proven to be an effective passivation in silicon solar cells.<sup>76</sup>





## Appendix A

# Matlab script: Heating a nanowire

The equation to be solved is

$$\frac{\partial u(t, x)}{\partial t} - k \frac{\partial^2 u(t, x)}{\partial x^2} - q(t, x) = 0 \quad , \quad (\text{A.1})$$

where  $u(t, x)$  is the heat per unit volume,  $k$  is the thermal diffusivity and  $q(t, x)$  is the heat generated per unit volume at a given rate. In a nanowire driven by a current  $I$  and with a voltage drop  $U$ , the heat generated per volume is

$$q(x, t) = UI/(ld^2\pi/4) \quad (\text{A.2})$$

where  $l$  and  $d$  are the length and the diameter of the nanowire. The initial condition is that the nanowire is at room temperature before the current passes through it, thus

$$u(t = 0, x) = u_0 = T_0 c \rho \quad (\text{A.3})$$

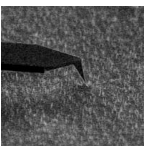
where  $c$  is the specific heat and  $\rho$  the density,  $0.713 \text{ Jg}^{-1}\text{K}^{-1}$  and  $2.329 \text{ gcm}^{-3}$  for silicon, respectively<sup>96</sup>. Solving the equation only for half the nanowire (symmetry point at its center), the boundary conditions are

$$u(t, x = 0) = u_0 \quad (\text{A.4})$$

$$\left( \frac{\partial u(t, x)}{\partial x} \right)_{x=l/2} = 0 \quad (\text{A.5})$$

which state a perfect heat sink at room temperature at the metal contact and no heat flow through the center of the nanowire.

Fortunately, there is no need to solve the partial differential equation analytically, **MATLAB** provides a function called **pdepe** that solves initial-boundary value problems for parabolic-elliptic partial differential equations in one dimension. The script presented here is based on a student project by A. Abrahamsen and D. Richards<sup>1</sup>, downloaded from <http://online.redwoods.cc.ca.us/instruct/darnold/DEProj/>. The student project describes the heat equation and how to solve it analytically as well as with the help of the **pdepe** function of **MATLAB** in detail. Fig. A.1 shows the script adapted to the present problem.



```

function heating_Nanowire

m = 0; % For slab evaluation, also known as the symmetry of the problem
l = 1e-4; % Length of nanowire, [cm]
timeinterval = 1e-8; % Timeinterval [s]

x = linspace(0,l/2,40); %This creates 40 equally spaced points
t = linspace(0,timeinterval,20); %This creates 20 equally spaced time points

sol = pdepe(m,@pde,@ic,@bc,x,t);
% The pde is a function for defining the components of the pde, ic is the
% initial conditions function, and bc is the boundary function. See the
% definitions below for explanations.

u = sol(:,:,1); %extract the first solution component

%plot the solution
surf(x,t,u)
xlabel('position [cm]')
ylabel('time(t) [s]')
zlabel('heat density [J/cm^3] ')

%=====

function [c,f,s] = pde(x,t,u,DuDx)
% The pde has to be put into the form shown below, p=partial
% c(x,t,u,pu/px)*pu/pt=x^(-m)*p/px*(x^m*f(x,t,u,pu/px)+s(x,t,u,pu/px)
%
% The heat equation for our problem is
% pu/pt = k * p^2u/px^2 + q
%
% where k is the thermal diffusivity and q the heat generated per volume
% at a given rate. We thus get the following parameters
l = 1e-4; % Length of nanowire, [cm]
d = 100e-7; % Diameter of nanowire, [cm]
U = 1; % Voltage applied [V]
I = 1e-6; % Current flowing [A]
k = 0.9; % thermal diffusivity of silicon at room temperature, [cm^2/s]
q = U*I/I/(d/2)^2/pi; % heat generated in the nanowire, [J/cm^3/s]
c = 1;
f = k*DuDx; % from the form shown earlier
s = q;

%=====

function u0 = ic(x)
% Initial conditions: heat density constant corresponding to
% room-temperature in the whole nanowire, u0 = T*c*rho
u0 = 487; % [J/cm^3]

%=====

function [p1,q1,pr,qr]=bc(x1,u1,xr,ur,t)
% Needs to be in the form,
% p(x,t,u)+q(x,t)f(x,t,u,DuDx)=0
%
% f(x,t,u,DuDx) = DuDx is the function defined in pde.
%
% The problem is symmetric, only half the nanowire can be simulated,
% and at its center we impose pu/px = 0. Then,
%
% p(x,t,u) = u1 - u0 and q(x,t) = 0 at x = 0
% p(x,t,u) = 0 and q(x,t) = 1 at x = L/2
u0 = 487; % [J/cm^3]
p1 = u1 - u0;
q1 = 0;
pr = 0;
qr = 1;

```

**Figure A.1:** MATLAB script for solving the partial differential equation for calculating the heating of a nanowire with the *pdepe* function.

## Appendix B

# Details of the lithography process

This appendix lists details concerning the EBeam lithography process used to contact nanowires in order to determine their resistivity, as presented in Sect. 3.4.

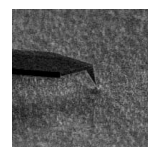
**The resists** used are from Allresist, with reference numbers PMMA 950K AR-P679.04 and PMMA 950K AR-P679.02. The .02 solution is measured to be 100 nm thick when spun for 35 s at 4000 rpm. The .04 solution is less diluted and yields thicker layers. Both solutions are used, with spinning speeds from 2000–4000 rpm. Subsequently the resist is always backed at 170 °C for 30 min on a hotplate. After exposure, the resist is developed in the AR600-56 developer from Allresist for 30–40 sec, followed by a dip in a stopper solution (AR600-60) for 30 s and is blown dry with nitrogen.

**The EBeam system** used is an ELine from Raith. It consists of a field emitter SEM with a stage that is equipped with a laser interferometer, enabling absolute positioning with a precision <100 nm over a range of several mm. Only 3 global markers are thus used for each sample.

**The exposure parameters** are adapted to the feature size of the structures. All structures are written at an acceleration voltage of 20 kV with a dose of 220  $\mu\text{C}/\text{cm}^2$  at a working distance of 18 mm. The thinnest structures,  $\approx 300$  nm pitch, are written with a EBeam current of 320 pA (aperture 30  $\mu\text{m}$ ), whereas for the largest structures the current is set to 12 nA (aperture 120  $\mu\text{m}$ , high current mode). Because there is a limit on the writing speed, the step size between two writing lines becomes larger than the diameter of the EBeam when exposure at high currents. The EBeam thus needs to be defocused for a uniform exposure at high currents.

**An HF dip** is done in a 5.4% buffered HF solution ( $\text{NH}_4\text{F}:\text{HF}_{38\%}$  7:1) for 10 s prior to each metal deposition in order to remove the native oxide of the nanowire at the contacts. The sample is transferred into the sputter chamber within 30 s after the HF dip.

**Metal deposition** of the electrode material is carried out with a sputterer from VonArdenne Anlagen Technik, which can take up to 6 sources in the same vacuum chamber. Ti and Au is used as electrode material. A thin layer of Ti (some nm, sputtering 30 s at 25 W)



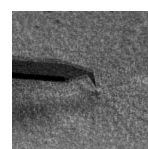
is used as an adherence layer between the Au and the SiO<sub>2</sub>. Prior to Ti deposition, the target is cleaned by sputtering for 30 s at 100 W onto a dummy sample. The Au thickness is chosen to be slightly thicker than the diameter of the nanowires, between 80–150 nm (sputtering 50–90 s at 50 W). Having several sources in the same sputter chamber is important in order to be able to change from Ti to Au without the need to ventilate. Ventilating oxidizes the Ti layer which results in a poor adherence of the Au on the SiO<sub>2</sub>. The chamber is pumped to a base pressure of  $2 \times 10^{-5}$  mbar prior to deposition, sputtering is performed at a working pressure of  $8 \times 10^{-3}$  mbar in argon.

**Lift-off** is carried out with a removal solution (**Allresist** AR600-70) in a ultrasonic bath at low power, in order to minimize the risk of lifting off the nanowire.



# List of Figures

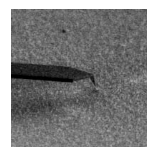
1.1	Different nanowires and experiments accomplished. . . . .	2
2.1	Growth diagram of VLS nanowire growth . . . . .	5
2.2	SEM and TEM images of a nanowire . . . . .	6
3.1	Potential devices from nanowires . . . . .	11
3.2	Resistance of a nanowire . . . . .	14
3.3	Regimes of TE, TFE and FE . . . . .	15
3.4	Metal–semiconductor contact illustrating TE, TFE and FE . . . . .	15
3.5	Contact resistance to a nanowire . . . . .	17
3.6	Depletion width of a metal–semiconductor contact . . . . .	17
3.7	Schematic of a 4 point resistance measurement . . . . .	18
3.8	Test of the measurement instrument . . . . .	19
3.9	Heating of the nanowire . . . . .	21
3.10	Influence of surface charge on resistivity . . . . .	23
3.11	Carrier velocity versus electric field for silicon . . . . .	24
3.12	EBeam lithography process . . . . .	27
3.13	Nanowires contacted by EBeam lithography . . . . .	29
3.14	SEM images of 4 point resistance experiment . . . . .	30
3.15	Classification of $U$ – $I$ characteristics . . . . .	30
3.16	$U$ – $I$ characteristics of an undoped nanowire . . . . .	32
3.17	$U$ – $I$ curves of a boron doped nanowire . . . . .	33
3.18	$U$ – $I$ curves of a phosphorous doped nanowire, P–sample 1 . . . . .	35
3.19	$U$ – $I$ curves of a phosphorous doped nanowire, P–sample 2 . . . . .	36
3.20	Nanowire connected by 8 electrodes . . . . .	37
3.21	Resistance variation along the growth axis of a nanowire . . . . .	38
3.22	Contact characteristics changing along a doped nanowire . . . . .	39
3.23	Principle of EBIC imaging . . . . .	41
3.24	Schematic overview of the ion implanted doping profiles . . . . .	42
3.25	Doping profile of the ion implanted nanowires . . . . .	43
3.26	Electrical diagram for the EBIC imaging . . . . .	44
3.27	EBIC image of a Schottky contact to a $n$ -doped nanowire . . . . .	45
3.28	EBIC images of $p$ - $n$ -doped nanowires . . . . .	46



3.29	$U$ - $I$ curves from $p$ - $n$ -doped nanowires . . . . .	47
4.1	Size effect on Si beams reported by Namazu <i>et al.</i> . . . . .	51
4.2	Bending experiment configuration . . . . .	53
4.3	Photograph of the manipulation setup . . . . .	55
4.4	Series of images from bending and tensile experiment . . . . .	56
4.5	Graphical user interface of <b>Spotfinder</b> . . . . .	57
4.6	Accuracy of <b>Spotfinder</b> in a simulated experiment . . . . .	58
4.7	Accuracy of <b>Spotfinder</b> in a tensile experiment . . . . .	59
4.8	Geometry of the FEM analysis . . . . .	60
4.9	Results of the FEM analysis . . . . .	60
4.10	SEM image of a Si nanowire subjected to the bending test . . . . .	61
4.11	SEM images of ZnO nanowires subjected to the mechanical tests . . . . .	63
4.12	Stress-strain curve for silicon simulated with the Brugger model . . . . .	67
5.1	Principle of the electromechanical experiment . . . . .	72
5.2	Process of growing nanowires in a Si trench . . . . .	73
5.3	SEM images of nanowires in a Si trench . . . . .	75
5.4	$U$ - $I$ characteristics of nanowires in a Si trench . . . . .	76
5.5	Mechanical strength of nanowire in Si trench . . . . .	77
A.1	MATLAB Script: Heating of a nanowire . . . . .	84

# List of Tables

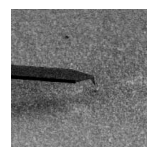
3.1	Thermal coefficients of Si, SiO <sub>2</sub> , Au and air . . . . .	20
3.2	Resistivity of boron doped nanowires . . . . .	33
3.3	Resistivity of P-sample 1 . . . . .	35
3.4	Resistivity of P-sample 2 . . . . .	36
4.1	Results from the bending experiment on Si nanowires . . . . .	61
4.2	Results from the bending experiment on ZnO nanowires . . . . .	63
4.3	Results from the tensile experiment on ZnO nanowires . . . . .	64
4.4	Error analysis on mechanical experiments . . . . .	64





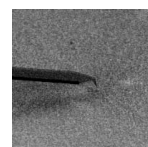
# Bibliography

- [1] ABRAHAMSEN, A., AND RICHARDS, D. The heat equation. Tech. rep., College of the Redwoods, Eureka, CA, USA, 2002.
- [2] AHN, Y., DUNNING, J., AND PARK, J. Scanning photocurrent imaging and electronic band studies in silicon nanowire field effect transistors. *Nano Letters* 5, 7 (2005), 1367.
- [3] BAI, X. D., GAO, P. X., WANG, Z. L., AND WANG, E. G. Dual-mode mechanical resonance of individual zno nanobelts. *Appl. Phys. Lett.* 82, 26 (2003), 4806.
- [4] BAUER, J., FLEISCHER, F., BREITENSTEIN, O., SCHUBERT, L., WERNER, P., GÖSELE, U., AND ZACHARIAS, M. Electrical properties of nominally undoped silicon nanowires grown by molecular-beam epitaxy. *Appl. Phys. Lett.* 90 (2007), 012105.
- [5] BECKER, M., SIVAKOV, V., ANDRÄ, G., GEIGER, R., SCHREIBER, J., HOFFMANN, S., MICHLER, J., MILENIN, A. P., WERNER, P., AND CHRISTIANSEN, S. H. The sers and ters effects obtained by gold droplets on top of si nanowires. *Nano Lett.* 7, 1 (2007), 75.
- [6] BECKER, M., SIVAKOV, V., GÖSELE, U., STELZNER, T., ANDRÄ, G., REICH, H. J., HOFFMANN, S., MICHLER, J., AND CHRISTIANSEN, S. H. Nanowires enabling signal-enhanced nanoscale raman spectroscopy. *Small* 4, 4 (2008), 398.
- [7] BJÖRK, M. T., THELANDER, C., HANSEN, A. E., JENSEN, L. E., LARSSON, M. W., WALLENBERG, L. R., AND SAMUELSON, L. Few-electron quantum dots in nanowires. *Nano Lett.* 4, 9 (2004), 1621.
- [8] BJÖRK, M. T., HAYDEN, O., RIEL, H., AND RIESS, W. Vertical surround-gated silicon nanowire impact ionization field-effect transistors. *Appl. Phys. Lett.* 90 (2007), 142110.
- [9] BJÖRK, M. T., OHLSSON, B. J., THELANDER, C., PERSSON, A. I., DEPPERT, K., WALLENBERG, L. R., AND SAMUELSON, L. Nanowire resonant tunneling diodes. *Appl. Phys. Lett.* 81, 23 (2002), 4458.
- [10] BYON, K., THAM, D., FISCHER, J. E., AND JOHNSON, A. T. Synthesis and postgrowth doping of silicon nanowires. *Appl. Phys. Lett.* 87 (2005), 193104.
- [11] CHAUDHRY, A., RAMAMURTHI, V., FONG, E., AND ISLAM, M. S. Ultra-low contact resistance of epitaxially interfaced bridged silicon nanowires. *Nano Lett.* 7, 6 (2007), 1536.
- [12] CHEN, C. Q., SHI, Y., ZHANG, Y. S., ZHU, J., AND YAN, Y. J. Size dependence of young's modulus in zno nanowires. *Phys. Rev. Lett.* 96, 7 (2006), 075505.



- [13] CHEN, Y., DORGAN JR., L., MCILROY, D., AND ASTON, D. On the importance of boundary conditions on nanomechanical bending behavior and elastic modulus determination of silver nanowires. *Journ. Appl. Phys.* 100 (2006), 104301.
- [14] CHEN, Y., WANG, X. H., ERRAMILLI, S., MOHANTY, P., AND KALINOWSKI, A. Silicon-based nanoelectronic field-effect ph sensor with local gate control. *Appl. Phys. Lett.* 89, 22 (2006), 223512.
- [15] CHRISTIANSEN, S. H., CHOU, J. W., BECKER, M., SIVAKOV, V., EHRHOLD, K., BERGER, A., CHOU, W. C., CHUU, D. S., AND GÖSELE, U. Fluorescence signals of core-shell quantum dots enhanced by single crystalline gold droplets on silicon nanowires. *Nanotechnology* (submitted).
- [16] COLLI, A., FASOLI, A., RONNING, C., PISANA, S., PISCANCE, S., AND FERRARI, A. C. Ion beam doping of silicon nanowires. *Nano Lett.* 8, 8 (2008), 2188.
- [17] COLLINS, C. B., CARLSON, R. O., AND GALLAGHER, C. Properties of gold-doped silicon. *Phys. Rev.* 105, 4 (1957), 1168.
- [18] CUI, Y., DUAN, X., HU, J., AND LIEBER, C. Doping and electrical transport in silicon nanowires. *J. Phys. Chem. B* 104, 22 (2000), 5213.
- [19] CUI, Y., AND LIEBER, C. L. Functional nanoscale electronic devices assembled using silicon nanowire building blocks. *Science* 291 (2001), 851.
- [20] CUI, Y., ZHONG, Z., WANG, D., WANG, W. U., AND LIEBER, C. M. High performance silicon nanowire field effect transistors. *Nano Lett.* 3, 2 (2003), 149.
- [21] DESAI, A. V., AND HAQUE, M. A. Mechanical properties of zno nanowires. *Sens. and Act. A In Press* (2006).
- [22] DUAN, X., HUANG, Y., CUI, Y., WANG, J., AND LIEBER, C. M. Indium phosphide nanowires as building blocks for nanoscale electronic and optoelectronic devices. *Nature* 409 (2001), 66.
- [23] EICHFELD, S. M., HO, T. T., EICHFELD, C. M., CRANMER, A., MOHNEY, S. E., MAYER, T. S., AND REDWING, J. M. Resistivity measurements of intentionally and unintentionally template-grown doped silicon nanowire arrays. *Nanotechn.* 18 (2007), 315201.
- [24] FAN, H. J., BERTRAM, F., DADGAR, A., CHRISTEN, J., KROST, A., AND ZACHARIAS, M. Self-assembly of zno nanowires and the spatial resolved characterization of their luminescence. *Nanotech.* 15, 11 (2004), 1401.
- [25] FAN, H. J., LEE, W., HAUSCHILD, R., ALEXE, M., LE RHUN, G., SCHOLZ, R., DADGAR, K., NIELSCH, K., KALT, H., KROST, A., ZACHARIAS, M., AND GÖSELE, U. Don't know. *Small* 2 (2006), 561.
- [26] FAN, H. J., LEE, W., SCHOLZ, R., DADGAR, A., KROST, A., NIELSCH, K., AND ZACHARIAS, M. Arrays of vertically aligned and hexagonally arranged zno nanowires: a new template-directed approach. *Nanotech.* 16, 6 (2005), 913.
- [27] FAN, H. J., SCHOLZ, R., ZACHARIAS, M., GÖSELE, U., BERTRAM, F., FORSTER, D., AND CHRISTEN, J. Don't know. *Appl. Phys. Lett.* 86 (2005), 023113.

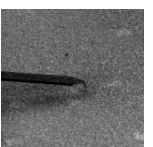
- [28] FREITAG, M., TSANG, J. C., BOL, A., YUAN, D., LIU, J., AND AVOURIS, P. Imaging of the schottky barriers and charge depletion in carbon nanotube transistors. *Nano Lett.* 7, 7 (2007), 2037.
- [29] GIVARGIZOV, E. I. Fundamental aspects of vls growth. *J. of Crystal Growth* 31 (1975), 20.
- [30] GRIFFITH, A. A. The phenomena of rupture and flow in solids. *Phil. Trans. Roy. Soc. London A221* (1921), 163.
- [31] GU, W., CHOI, H., AND KIM, K. Universal approach to accurate resistivity measurement for a single nanowire: Theory and application. *Appl. Phys. Lett.* 89 (2006), 253102.
- [32] GU, Y., RAMONKIEWICZ, J. P., DAVID, J. K., LENSCH, J. L., AND LAUHON, L. J. Quantitative measurement of the electron and hole mobility-lifetime products in semiconductor nanowires. *Nano Lett.* 6, 2 (2006), 948.
- [33] GUDIKSEN, M. S., LAUHON, L. J., WANG, J., SMITH, D. C., AND LIEBER, C. M. Growth of nanowire superlattice structures for nanoscale photonics and electronics. *Nature* 415 (2002), 617.
- [34] HAN, X., ZHENG, K., ZHANG, Y. F., ZHANG, X., ZHANG, Z., AND WANG, Z. L. Low-temperature in situ large-strain plasticity of silicon nanowires. *Adv. Mat.* 19, 16 (2007), 2112.
- [35] HANNON, J. B., KODAMBAKA, S., ROSS, F. M., AND TROMP, R. M. The influence of the surface migration of gold on the growth of silicon nanowires. *Nature* 440, 7080 (2006), 69.
- [36] HAUGERUD, B. M., BOSWORTH, L. A., AND BELFORD, R. E. Mechanically induced strain enhancement o metal-oxide-semiconductor field-effect transistors. *J. Appl. Phys.* 94 (2003), 4102.
- [37] HE, R., GAO, D., FAN, R., HOCHBAUME, A. I., CARRARO, C., MABOUDIAN, R., AND YANG, P. Si nanowire bridges in microtrenches: Integration of growth into device fabrication. *Adv. Mat.* 17 (2005), 2098.
- [38] HE, R., AND YANG, P. Giant piezoresistance effect in silicon nanowires. *Nature Nanotech.* 1 (2006), 42.
- [39] HEIDELBERG, A., NGO, L. T., MICK, B. W., PHILLIPS, A., SHARMA, S., KAMINS, T. I., SADER, J. E., AND BOLAND, J. J. A generalized description of the elastic properties of nanowires. *Nano Lett.* 6, 6 (2006), 1101.
- [40] HONG, K. H., KIM, J., LEE, S. H., AND SHIN, J. K. Strain-driven electronic band structure modulation of si nanowires. *Nano Lett.* 8, 5 (2008), 1335.
- [41] HUANG, M. H., MAO, S., FEICK, H., YAN, H., WU, Y., KIND, H., WEBER, E., RUSSO, R., AND YANG, P. Room-temperature ultraviolet nanowire nanolasers. *Science* 292 (2001), 1897.
- [42] HUANG, Y., BAI, X., AND ZHANG, Y. Don't know. *J. Phys.: Condens. Matter* 18 (2006), L179.
- [43] HUANG, Y., BAI, X., ZHANG, Y., QI, J., GU, Y., AND LIAO, Q. Field-emission properties of individual zno nanowires studied in situ by transmission electron microscopy. *J. Phys.: Cond. Mat.* 19 (2007), 176001.



- [44] IMAMURA, G., KAWASHIMA, T., FUJII, M., NISHIMURA, C., SAITOH, T., AND HAYASHI, S. Distribution of active impurities in single silicon nanowires. *Nano Lett.* 8, 9 (2008), 2620.
- [45] JACCODINE, R. J. Surface energy of germanium and silicon. *J. Electrochem. Soc.* 110, 6 (1963), 524.
- [46] JOHNSON, J., CHOI, H. J., KNUTSEN, K. P., SCHALLER, R. D., YANG, P., AND SAYKALLY, R. J. Single gallium nitride nanowire lasers. *Nature mat.* 1 (2002), 106.
- [47] KANG, K., AND CAI, W. Brittle and ductile fracture of semiconductor nanowires - molecular dynamics simulations. *Phil. mag.* 87, 14-15 (2007), 2169.
- [48] KIMUKIN, I., SAIF ISLAM, M., AND STANLEY WILLIAMS, R. Surface depletion thickness of p-doped silicon nanowires grown using metal-catalysed chemical vapour deposition. *Nanotechnology* 17 (2006), S240.
- [49] KIZUKA, T., TAKATANI, Y., ASAKA, K., AND YOSHIZAKI, R. Measurements of the atomistic mechanics of single crystalline silicon wires of nanometer width. *Phys. Rev. B* 72, 3 (2005), 035333.
- [50] KROST, A., DADGAR, A., STRASSBURGER, G., AND CLOS, R. Gan-based epitaxy on silicon: stress measurements. *Phys. Stat. Sol. A* 200, 1 (2003), 26.
- [51] LANDOLT-BÖRNSTEIN. *Zahlenwerte und Funktionen*, 3 ed., vol. 11. Springer Verlag, 1984.
- [52] LANGFORD, R. M., WANG, T. X., THORNTON, M., HEIDELBERG, A., SHERIDAN, J. G., BLAU, W., AND LEAHY, R. Comparison of different methods to contact to nanowires. *J. Vac. Sci. Techn. B* 24, 5 (2006), 2306.
- [53] LEAMY, H. J. Charge collection scanning electron microscopy. *J. Appl. Phys.* 53, 6 (1982), R51.
- [54] LEE, M. L., FITZGERALD, E. A., BULSARA, M. T., CURRIE, M. T., AND LOCHTEFELD, A. Strained si, sige and ge channels for high-mobility metal-oxide-semiconductor field-effect transistors. *J. Appl. Phys.* 97 (2005), 011101.
- [55] LEU, P. W., SVIZHENKO, A., AND CHO, K. Ab initio calculations of the mechanical and electronic properties of strained si nanowires. *Phys. Rev. B* 77, 23 (2008), 235305.
- [56] LEW, K. K., PAN, L., BOGART, T. E., DILTS, S. M., DICKEY, E. C., REDWING, J. M., WANG, Y., CABASSI, M., MAYER, T. S., AND NOVAK, S. W. Structural and electrical properties of trimethylboron-doped silicon nanowires. *Appl. Phys. Lett.* 85, 15 (2004), 3101.
- [57] LI, D., WU, Y., KIM, P., SHI, L., YANG, P., AND MAJUMDAR, A. Thermal conductivity of individual silicon nanowires. *Appl. Phys. Lett.* 83, 14 (2003), 2934.
- [58] LI, X., ONO, T., WANG, Y., AND ESASHI, M. Ultrathin single-crystalline-silicon cantilever resonators: Fabrication technology and significant specimen size effect on young's modulus. *Appl. Phys. Lett.* 83, 15 (2003), 3081.
- [59] LIBIOULLE, L., HOUBION, Y., AND GILLES, J.-M. Very sharp platinum tips for scanning tunneling microscopy. *Rev. Sci. Instrum.* 66, 1 (1995), 97.
- [60] LIN, R., BØGGILD, P., AND HANSEN, O. Microcantilever equipped with nanowire template electrodes for multiprobe measurement on fragile nanostructures. *J. Appl. Phys.* 96, 5 (2004), 2895.

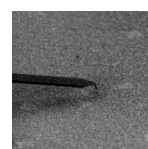


- [61] LIN, X., HE, X. B., YANG, T. Z., GUO, W., SHI, D. X., GAO, H. J., MA, D. D. D., LEE, S. T., LIU, F., AND XIE, X. C. Intrinsic current-voltage properties of nanowires with four-probe scanning tunneling microscopy: A conductance transition of zno nanowire. *Appl. Phys. Lett.* 89 (2006), 043103.
- [62] LUGSTEIN, A., STEINMAIR, M., HYUN, Y., AND BERTAGNOLLI, E. Ga/au alloy catalyst for single crystal silicon-nanowire epitaxy. *Appl. Phys. Lett.* 90 (2007), 023109.
- [63] LUGSTEIN, A., STEINMAIR, M., HYUN, Y., HAUER, G., PONGRATZ, P., AND BERTAGNOLLI, E. Pressure-induced orientation control of the growth of epitaxial silicon nanowires. *Nano Lett.* 8, 8 (2008), 2310.
- [64] LUSCOMBE, J. H., AND FRENZEN, C. L. Depletion lengths in semiconductor nanostructures. *Solid State Elect.* 46 (2002), 885.
- [65] MAYER, J. W., ERIKSSON, L., AND DAVIES, J. A. *Ion implantation into Semiconductors*. Academic Press, 1970.
- [66] MEYER, B., AND MARX, D. Density-functional study of the structure and stability of zno surfaces. *Phys. Rev. B* 67, 3 (2003), 035403.
- [67] MILLER, R. E., AND SHENOY, V. B. Size-dependent elastic properties of nanosized structural elements. *Nanotechnology* 11 (2000), 139.
- [68] MISHRA, N. N., MAKI, W. C., CAMERON, E., NELSON, R., WINTERROWD, P., RASTOGI, S. K., FILANOSKI, B., AND MAKI, G. K. Ultra-sensitive detection of bacterial toxin with silicon nanowire transistor. *Lab on a chip* 8 (2008), 868.
- [69] MOHNEY, S. E., WANG, Y., CABASSI, M. A., LEW, K. K., DEY, S., REDWING, J. M., AND MAYER, T. S. Measuring the specific contact resistance of contacts to semiconductor nanowires. *Solid-State Elect.* 49 (2005), 227.
- [70] MURCH, G. E., AND NOWICK, A. S. *Diffusion in Crystalline Solids*. Academic Press Inc., 1984.
- [71] NAM, C. Y., JAROENAPIBAL, P., THAM, D., LUZZI, D. E., EVOY, S., AND FISCHER, J. E. Diameter-dependent electromechanical properties of gan nanowires. *Nano Lett.* 6, 2 (2006), 153.
- [72] NAMAZU, T., ISONO, Y., AND TANAKA, T. Evaluation of size effect on mechanical properties of single crystal silicon by nanoscale bending test using afm. *J. Microelectromech. Sys.* 9, 4 (2000), 450.
- [73] NG, H. T., HAN, J., YAMADA, T., NGUYEN, P., CHEN, Y. P., AND MEYYAPPAN, M. Single crystal nanowire vertical surround-gate field-effect transistor. *Nano Lett.* 4, 7 (2004), 1247.
- [74] NI, H., LI, X., AND GAO, H. Elastic modulus of amorphous sio<sub>2</sub> nanowires. *Appl. Phys. Lett.* 88, 4 (2006), 043108.
- [75] OH, S. H., VAN BENTHEM, K., MOLINA, S. I., BORISEVICH, A. Y., LUO, W., WERNER, P., ZAKHAROV, N. D., KUMAR, D., PANTELIDES, S., AND PENNYCOOK, S. J. Point defect configurations of supersaturated au atoms inside si nanowires. *Nano Lett.* XX, XX (2008), ToDo: Complete citation.



- [76] OLIBET, S., VALLAT-SAUVAIN, E., BALLIF, C., KORTE, L., AND FESQUET, L. Silicon solar cell passivation using heterostructures. *Proc. 17th Workshop on Crystalline Silicon Solar Cells and Modules: Materials and Processes* (August 2007), 130.
- [77] OROWAN, E. Fracture and strength of solids. *Rep. Prog. Phys.* 12 (1949), 183.
- [78] ÖSTLUND, F., RZEPJEJEWSKA-MALYSKA, K., LEIFER, K., AND MICHLER, J. Brittle-to-ductile transition in uniaxial compression of silicon pillars at room temperature. *Small submitted* (2008).
- [79] PADOVANI, F. A., AND STRATTON, R. Field and thermionic-field emission in schottky barriers. *Solid-State Elec.* 9 (1966), 695.
- [80] PARK, H. S. Surface stress effects on the resonant properties of silicon nanowires. *J. Appl. Phys* 102, 12 (2008), 123504.
- [81] PARK, W. I., ZHENG, G., JIANG, X., TIAN, B., AND LIEBER, C. M. Controlled synthesis of millimeter-long silicon nanowires with uniform electronic properties. *Nano Lett.* 8, 9 (2008), 3004.
- [82] SAMUELSON, L., BJÖRK, M. T., DEPPERT, K., LARSSON, M., OHLSSON, B. J., PANEV, N., PERSSON, A. I., SKÖLD, N., THELANDER, C., AND R, W. L. Semiconductor nanowires for novel one-dimensional devices. *Physica E* 21 (2004), 560.
- [83] SAN PAULO, A., BOKOR, J., HOWE, R. T., HE, R., YANG, P., GAO, D., CARRARO, C., AND MABOUDIAN, R. Mechanical elasticity of single and double clamped silicon nanobeass fabricated by the vapor-liquid-solid method. *Appl. Phys. Lett.* 87 (2005), 053111.
- [84] SCHMIDT, V., RIEL, H ANDSENZ, S., KARG, S., RIESS, W., AND GÖSELE, U. Realization of a silicon nanowire vertical surround-gate field-effect transistor. *Small* 2, 1 (2006), 85.
- [85] SCHMIDT, V., SENZ, S., AND GÖSELE, U. UHV chemical vapour deposition of silicon nanowires. *Zeitschrift für Metallkunde* 96, 5 (2005), 427–428.
- [86] SCHUBERT, L., WERNER, P., ZAKHAROV, N., GERTH, G., KOLB, F., LONG, L., GÖSELE, U., AND TAN, T. Silicon nanowhiskers grown on <111> si substrates by molecular-beam epitaxy. *Appl. Phys. Lett.* 84, 24 (2004), 4968.
- [87] SEO, K., SHARMA, S., YASSERI, A. A., STEWART, D. R., AND I, K. T. Surface charge density of unpassivated and passivated metal-catalyzed silicon nanowires. *Electrochem. Sol. State Lett.* 9, 3 (2006), G69.
- [88] SHARMA, S., KAMINS, T. I., AND STANLEY WILLIAMS, R. Diameter control of ti-catalyzed silicon nanowires. *J. Crystal Growth* 267, 3-4 (2004), 613.
- [89] SHIRI, D., KONG, Y., BUIN, A., AND ANANTRAM, M. P. Strain induced change of bandgap and effective mass in silicon nanowires. *Appl. Phys. Lett.* 93, 7 (2008), 073114.
- [90] SIVAKOV, V., HEYROTH, F., FALK, F., ANDRÄ, G., AND CHRISTIANSEN, S. Silicon nanowire growth by electron beam evaporation: Kinetic and energetic contributions to the growth morphology. *J. of Cryst. Growth* 300 (2007), 288.
- [91] SONG, J., WANG, X., RIEDO, E., AND WANG, Z. L. Elastic property of vertically aligned nanowires. *Nano Lett.* 5, 10 (2005), 1954.

- [92] STEINMAIR, M. *Synthesis and electrical characterization of silicon nanowires*. PhD thesis, Technical University of Vienna, 2008.
- [93] STERN, E., CHENG, G., KLEMIC, J. F., BROOMFIELD, E., TURNER-EVANS, D., LI, C., ZHOU, C., AND REED, M. A. Methods for fabricating ohmic contacts to nanowires and nanotubes. *J. Vac. Sci. Technol. B* 24, 1 (2006), 333.
- [94] STICHTENOTH, D., WEGENER, K., GUTSCHE, C., REGOLIN, I., TEGUDE, F. J., PROST, W., SEIBT, M., AND RONNING, C. P-type doping of gaas nanowires. *Appl. Phys. Lett.* 92, 17 (2008), 163107.
- [95] STONE, M. J., AND AHMED, H. Silicon single electron memory cell. *Appl. Phys. Lett.* 73, 15 (1998), 2134.
- [96] SZE, S. M., AND NG, K. K. *Physics of semiconductor devices*, 3 ed. John Wiley and Sons, 2007.
- [97] TABIB-AZAR, M., NASSIROU, M., WANG, R., SHARMA, S., KAMINS, T. I., SAIF ISLAM, M., AND WILLIAMS, R. S. Mechanical properties of self-welded silicon nanobridges. *Appl. Phys. Lett.* 87 (2005), 113102.
- [98] TANG, Q., KAMINS, T. I., LIU, X., GRUPP, D. E., AND HARRISA, J. S. In situ p-n junctions and gated devices in titanium-silicide nucleated si nanowires. *Electrochem. Sol. State Lett.* 8, 8 (2005), G240.
- [99] THELANDER, C., MARTENSSON, T., BJÖRK, M. T., OHLSSON, B. J., LARSSON, M. W., R, W. L., AND SAMUELSON, L. Single-electron transistors in heterostructure nanowires. *Appl. Phys. Lett.* 83 (2003), 2052.
- [100] THURSTON, R. N., AND BRUGGER, K. Third-order elastic constants and the velocity of small amplitude elastic waves in homogeneously stressed media. *Phys. Rev.* 133, 6A (1964), A1604.
- [101] TIAN, B., ZHENG, X., KEMPA, T. J., FANG, Y., YU, N., YU, G., HUANG, J., AND LIEBER, C. M. Coaxial silicon nanowires as solar cells and nanoelectronic power sources. *Nature* 449 (2007), 885.
- [102] TIMOSHENKO, S. P., AND GOODIER, J. N. *Theory of elasticity*, 3 ed. Mac Graw-Hill, 1934.
- [103] TORTONESE, M., BARRETT, R. C., AND QUATE, C. F. Atomic resolution with an atomic force microscope using piezoresistive detection. *Appl. Phys. Lett.* 62 (1992), 834.
- [104] TUFTE, O. N., CHAPMAN, P. W., AND LONG, D. Silicon diffused-element piezoresistive diaphragms. *J. Appl. Phys.* 33 (1962), 3322.
- [105] WANG, W., ZHANG, G., YU, L., BAI, X., ZHANG, Z., AND ZHAO, X. Field emission properties of zinc oxide nanowires fabricated by thermal evaporation. *Physica E* 36 (2007), 86.
- [106] WANG, X., SONG, J., LIU, J., AND WANG, Z. L. Direct-current nanogenerator driven by ultrasonic waves. *Science* 316 (2007), 102.
- [107] WANG, Y., LEW, K. K., HO, T. T., PAN, L., NOVAK, S. W., DICKEY, E. C., REDWING, J. M., AND MAYER, T. S. Use of phosphine as an n-type dopant source for vapor-liquid-solid growth of silicon nanowires. *Nano Lett.* 5 (2005), 2139.



- [108] WEE, K. W., KANG, G. Y., PARK, J., KANG, J. Y., YOON, D. S., PARK, J. H., AND KIM, T. S. Novel electrical detection of label-free disease marker proteins using piezoresistive self-sensing micro-cantilevers. *Biosens. & Bioel.* *20* (2005), 1932.
- [109] WEIBULL, W. A statistical distribution function of wide applicability. *J. Appl. Mech.-Transact. ASME* *18*, 3 (1951), 293.
- [110] WERN, H. *Single Crystal Elastic Constants and Calculated Bulk Properties*. Logos Verlag, 2004.
- [111] YANG, C., ZHONG, Z., AND LIEBER, C. M. Encoding electronic properties by synthesis of axial modulation-doped silicon nanowires. *Science* *310*, 5752 (2005), 1304.
- [112] YU, A. Y. C. Electron tunneling and contact resistance of metal-silicon contact barriers. *Solid-State Elec.* *13* (1970), 239.
- [113] YU, J. Y., CHUNG, S. W., AND HEATH, J. R. Silicon nanowires: Preparation, device fabrication, and transport properties. *J. Phys. Chem. B* *104* (2000), 11864.
- [114] ZARUDI, I., ZHANG, L. C., CHEONG, W. C. D., AND YU, T. X. The difference of phase distributions in silicon after indentation with berkovich and spherical indenters. *Acta Mat.* *53* (2005), 4795.
- [115] ZHENG, G., LU, W., JIN, S., AND LIEBER, C. M. Synthesis and fabrication of high-performance n-type silicon nanowire transistors. *Adv. Mat.* *16*, 21 (2004), 1890.
- [116] ZHENG, G., PATOLSKY, F., CUI, Y., WANG, W. U., AND LIEBER, C. M. Multiplexed electrical detection of cancer markers with nanowire sensor arrays. *Nature Biotech.* *23*, 10 (2005), 1294.
- [117] ZHOU, L. G., AND HUANG, H. Are surfaces elastically softer or stiffer? *Appl. Phys. Lett.* *84*, 11 (2004), 1940.
- [118] ZIEGLER, J. F., BIRSACK, J. P., AND LITTMARK, U. *The stopping and ranges of ions in solids*. Pergamon Press, 1985.

# Acknowledgements

First, without the constant support of my supervisor Johann Michler, Head of the department of Mechanics of Micro-materials and Nanostructures at EMPA and the Director of my thesis Christophe Ballif, Chair of the Photovoltaics and Thin Film Electronics Laboratory at the University of Neuchâtel, this work could not have been brought to a successful conclusion. Aside from the valuable scientific input, they also both supported me spending a part of the time in another institution.

Other official partners are:

- At the Technical University in Vienna (A) special thanks go to Mathias Steinmair and Christoph Schöndorfer for both their scientific help and inputs and the moral support. But also Alois Lugstein, Erwin Auer, Youn-Joo Hyun and Thomas Burchhart have been a great help.
- At the Max Plank Institute of Microstructure Physics in Halle (D) I could count on the support and contribution of Jan Bauer, Frank Fleischer, Silke Christiansen, Pratyush Das-Kanungo, Volker Schmidt, Stephan Senz, Michael Becker, Luise Schubert, and Peter Werner
- At the Institute for Photonic Technologies in Jena (D) Thomas Stelzner, Vladimir Sivakov, Matthias Pietsch and Björn Eisenhawer were continuously active growing nanowires, but also contributed through helpful discussions.

Tiphaine Dupont spent six months for her diploma thesis on setting up a lithography process at EMPA. I thank her for her constantly positive spirit, even in quite desperate situations. Staying at EMPA, I thank Vinzenz Friedli for the company in setting up the AFM within the SEM, which was not useful for this work, but probably the most fun time. Many thanks also go to Fredrik Östlund who, sitting in the same office, needed to stand my mood in difficult times and shared lots of ideas and thoughts making the work more efficient, but I also thank him for compensating the time gained with discussions not having a direct link to work. Many thanks go to Gerhard Bürki who introduced me to the world of electron microscopy and provided valuable assistance in the lab with his large experience of the technical aspects involved. I thank Kilian, Adrien, Simona, Hiroyuki, Ivo, Mikhael, Christian, Danilo, Philippe and Jaques for participating in *ex situ* activities and for the stimulating environment created therewith.

In mechanically characterizing the nanowires, Ondrej Papes was a very patient teacher on non-linear calculations of the stress-strain relationships, and also helped characterizing **Spotfinder**. My gratitude also goes to Michel Troyon from the University of Reims (F), who was very patient as well, compressing silicon nanowires and micro pillars.

Finally, acknowledgments also go to the Swiss National Science Foundation (SNSF) for financing me the first two years, to the European Union for financing another 1½ years through the sixth framework programme, and to the Janggen-Pöhn Stiftung for financing my research stay in Vienna.



# List of Publications

## Book chapter

- V. Friedli, S. Hoffmann, J. Michler, and I. Utke. AFM Sensors in Scanning Electron and Ion Microscopes: Tools for Nanomechanics, Nanoanalytics, and Nanofabrication. In B. Bhushan, H. Fuchs, and M. Tomitori, editors, *Applied Scanning Probe Methods VIII*. Springer, Heidelberg, 2008 (Online version available at [www.springer.com/978-3-540-74079-7](http://www.springer.com/978-3-540-74079-7))

## Journal articles

- S. Hoffmann, J. Bauer, C. Ronning, T. Stelzner, J. Michler, C. Ballif, V. Sivakov, S. H. Christiansen, Axial p-n junctions realized in silicon nanowires by ion implantation. *Nano Letters*, *accepted for publishing in 2009*
- M. Becker, V. Sivakov, U. Gösele, T. Stelzner, G. Andrä, H. J. Reich, S. Hoffmann, J. Michler, S. H. Christiansen, Nanowires enabling signal-enhanced nanoscale Raman spectroscopy. *Small*, 4(4):398-404, 2008
- S. Hoffmann, F. Östlund, J. Michler, H. J. Fan, M. Zacharias, S. H. Christiansen, C. Ballif, Fracture strength and Young's modulus of ZnO nanowires. *Nanotechnology*, 18(20):205503, 2007
- M. Becker, V. Sivakov, G. Andrä, R. Geiger, J. Schreiber, S. Hoffmann, J. Michler, A. P. Milenin, P. Werner, S. H. Christiansen, The SERS and TERS effects obtained by gold droplets on top of Si nanowires. *Nano Letters*, 7(1):75-80, 2007
- S. Hoffmann, I. Utke, B. Moser, J. Michler, S. H. Christiansen, V. Schmidt, S. Senz, P. Werner P, U. Gösele, C. Ballif, Measurement of the bending strength of vapor-liquid-solid grown silicon nanowires. *Nano Letters*, 6(4):622-625, 2006
- I. Utke, V. Friedli, S. Fahlbusch, S. Hoffmann, P. Hoffmann, and J. Michler, Tensile strengths of metal-containing joints fabricated by focused electron beam induced deposition. *Adv. Eng. Mater.*, 8(3):155-157, 2006





# Curriculum Vitae

## Personal data

Name: Samuel HOFFMANN  
Date of birth: 24. 09. 1979  
Place of birth: Zug (CH)  
Nationality: Swiss / Australian

## Professional activities

2005 - 2008: Swiss Federal Laboratories for Materials Testing and Research (EMPA)  
Ph.D. project at the Laboratory for Mechanics of Micro-materials and Nanostructures

2008: Technical University of Vienna (3 months)  
Research stay in the Institute for Solid State Electronics within the Ph.D. project

2003: Technical University of Warsaw (6 weeks)  
Internship at the Institute for Electron Technology

2001 - 2002: Süss MicroOptics, Neuchâtel (4 months)  
Internship on the characterization of micro lenses

## Education

1999 - 2005: University of Neuchâtel  
Master of Science in Micro- and Nanotechnologies

1992 - 1999: Gymnasium Zug  
Matura Typus C (Natural Sciences)